

---

# **Doppler Global Velocimeter Development for the Large Wind Tunnels at Ames Research Center**

---

Michael S. Reinath

---

September 1997



National Aeronautics and  
Space Administration

---

# Doppler Global Velocimeter Development for the Large Wind Tunnels at Ames Research Center

---

Michael S. Reinath, Ames Research Center, Moffett Field, California

September 1997



National Aeronautics and  
Space Administration

**Ames Research Center**  
Moffett Field, California 94035-1000

# Contents

	Page
List of Figures .....	v
Nomenclature .....	vii
Summary .....	1
Introduction.....	1
System Description .....	2
General.....	2
Laser.....	2
Beam-Delivery Optics .....	2
Camera Optics .....	3
Data Acquisition Instrumentation .....	5
Data Reduction.....	5
Basics.....	5
Reduction of Raw Images.....	8
System Calibration .....	11
Pixel Sensitivity Calibration .....	11
Spatial Calibration .....	11
Iodine-Cell Response Calibration .....	14
Flatfield Calibration.....	16
Measurement Uncertainty .....	16
CCD Radiometric Measurement Uncertainty .....	16
Doppler-Shift Uncertainty .....	18
Orthogonal-Component Uncertainty .....	19
Experimental Results .....	22
Background.....	22
Jet Engine Simulator Exhaust-Plume Measurements .....	22
Advanced Fighter LEX-Vortex Measurements .....	26
Wing Tip-Vortex Measurements .....	32
Flap-Edge Vortex Measurements .....	35
Conclusions.....	41
Appendix A—Unit Vectors for General-Case Viewing Geometry .....	43
Appendix B— $U$ -, $V$ -, and $W$ -Component Precision Uncertainty.....	45
References.....	49

## List of Figures

Figure	Page
1. Diagram of the optical components that monitor the beam frequency and create the laser sheet.....	3
2. Diagram of the camera system optics (iodine-cell heaters, thermocouples, and enclosure are not shown) .....	4
3. Data acquisition instrumentation .....	6
4. DGV measurement geometry for obtaining a single velocity component .....	7
5. Overview of the conversion from image intensity to Doppler frequency shift .....	8
6. Sequence of processing steps to convert raw DGV images to velocity .....	9
7. Response of CCD sensor to uniform illumination illustrating the effectiveness of the pixel sensitivity correction. (a) Image before pixel sensitivity correction. (b) Image after pixel sensitivity correction.....	12
8. Sample images illustrating the spatial calibration. (a) Gray-level, spatial-calibration image. (b) Bi-level image showing software tool that sets image boundary. (c) Scan result showing rectangles that identify all marks located by the scan.....	13
9. Typical iodine response curves showing repeatability and sensitivity to stem temperature (cell body temperature = 160° F). (a) Iodine response measured five times on consecutive days. (b) Iodine response measured at three different stem temperatures .....	15
10. Measured total CCD radiometric variance for mean signal levels ranging from near zero to near saturation.....	18
11. Uncertainty of the measured Doppler shift due to random effects. Signal strength of the unfiltered camera is assumed to be sufficient to fill the pixel wells to two-thirds capacity, and the laser frequency is assumed to be set midway between maximum and minimum absorption .....	19
12. Coordinate system and measurement geometry used to develop the expressions that define the unit vector directions of the measured components .....	21
13. Isolated engine simulator shown in the Ames 40- by 80-Foot Wind Tunnel test section. The nozzle shown is a conical nozzle and not the mixer-ejector described in the text .....	22
14. Diagram of the test section showing the camera locations, laser sheet, and the directions of the measured components (view is shown looking upstream) .....	23
15. Measured mean axial component of the jet simulator exhaust plume. (a) Mean axial velocity image. (b) Vertical profile through the center of the velocity image .....	24
16. Comparison between DGV and rake velocity measurements through the center of the exhaust plume .....	26
17. Generic advanced fighter model shown in the Ames 40- by 80-Foot Wind Tunnel test section. (a) General installation showing high-alpha condition. (b) Flow visualization showing DGV measurement location.....	27
18. Diagram of the test section showing the camera locations, laser sheet, and the directions of the measured components (view is shown looking upstream).....	28
19. Measured mean orthogonal components of LEX flow field (looking upstream). (a) Streamwise component. (b) Spanwise component (positive to the right). (c) Downwash component (positive up). (d) Horizontal profile through the center of the vortex. (e) Vertical profile through the center of the vortex.....	29



20.	High-Speed Civil Transport model shown in the Ames 7- by 10-Foot Wind Tunnel test section.....	32
21.	Test section diagram showing the camera locations, laser sheet, and the directions of the measured components.....	33
22.	Measured mean orthogonal components of the High-Speed Civil Transport wake flow field (looking downstream). (a) Streamwise component. (b) Spanwise component (positive to the left). (c) Downwash component (positive up) .....	34
23.	NACA 63 <sub>2</sub> -215 Mod B airfoil and 0.3 chord, half-span flap shown in the Ames 7- by 10-Foot Wind Tunnel test section .....	35
24.	Test section diagram showing the camera locations, laser sheet, and the directions of the measured components.....	36
25.	Measured mean orthogonal components of the flap-edge vortical flow field (looking upstream). (a) Streamwise component. (b) Spanwise component (positive up). (c) Downwash component (positive to the right). (d) Vertical profile through center of vortex. (e) Horizontal profile through center of vortex .....	37

## Nomenclature

$B_i$	bias limit (estimated so that the experimenter is confident that in 95 out of 100 measurements the true value of the bias error, if known, would be less than $ B_i $ )	$S$	filtered diode signal in volts
$\langle C_i \rangle$	mean intensity level in counts at the $i$ th pixel	$S_i$	standard deviation of an ensemble of measurements
$f_D$	frequency of the Doppler shifted laser light	$s_i$	filtered camera signal at the $i$ th pixel in electrons
$f_{\max}$	frequency outside the absorption well of the iodine response where maximum transmission occurs	$T(f_D)$	iodine filter transmission at the frequency $f_D$
$f_0$	frequency of the unshifted laser light	$T(f_{\max})$	iodine filter transmission at the frequency $f_{\max}$
$G_{AD}$	analog-to-digital conversion gain in electrons/count	$U$	magnitude of the total velocity vector component in the direction of the x-axis
$G_R$	gain of the reference camera and frame grabber	$U_i$	total uncertainty of a particular measurement in an ensemble of measurements
$G_S$	gain of the signal camera and frame grabber	$U_m$	magnitude of the measured Doppler global velocimetry component
$k$	coverage factor (2 for large sample sizes and 95% confidence)	$U_{ma}$	magnitude of the component measured by camera a
$\hat{k}$	unit vector opposite to the viewing direction	$U_{mb}$	magnitude of the component measured by camera b
$\hat{l}$	unit vector in the direction of the laser beam path	$U_{mc}$	magnitude of the component measured by camera c
$N$	normalized value of the reference iodine cell	$V$	magnitude of the total velocity vector component in the direction of the y-axis
$n$	normalized value (signal pixel intensity/reference pixel intensity)	$\vec{V}$	total velocity vector
$n_{\text{corrected}}$	normalized value after correction with the flatfield image	$W$	magnitude of the total velocity vector component in the direction of the z-axis
$n_{ff}$	normalized value of the flatfield image	$X_1, Y_1, Z_1$	unit vector components that define the direction of the component measured by camera a
$n_i$	normalized value of the $i$ th pixel	$X_2, Y_2, Z_2$	unit vector components that define the direction of the component measured by camera b
$P_i$	precision limit = $kS_i$ (the interval about the mean within which the mean value would fall 95 times out of 100 if the experiment were repeated many times under the same conditions using the same equipment, assuming $k = 2$ )	$X_3, Y_3, Z_3$	unit vector components that define the direction of the component measured by camera c
$R$	unfiltered diode signal in volts	$x_i, y_i, z_i$	wind tunnel coordinates of the $i$ th pixel projected onto the object plane
$r_i$	unfiltered camera signal at the $i$ th pixel in electrons	$x_s, y_s, z_s$	wind tunnel coordinates of the laser sheet point of origin

$x_1, y_1, z_1$	wind tunnel coordinates of camera a	$\sigma_{r_i}$	radiometric noise of the unfiltered camera in electrons
$x_2, y_2, z_2$	wind tunnel coordinates of camera b	$\sigma_S$	standard deviation of the unfiltered diode signal
$x_3, y_3, z_3$	wind tunnel coordinates of camera c	$\sigma_{s_i}$	radiometric noise of the filtered camera in electrons
$\beta$	angle between the unit vectors $-\hat{l}$ and $\hat{k}$	$\sigma_U, \sigma_V, \sigma_W$	standard deviations of the $U$ , $V$ , and $W$ components
$\Delta f$	Doppler frequency shift	$\sigma_{X_1}, \sigma_{Y_1}, \sigma_{Z_1}$	standard deviations of the unit vectors that define the component measured by camera a
$\lambda_0$	wavelength of the unshifted laser light	$\sigma_{X_2}, \sigma_{Y_2}, \sigma_{Z_2}$	standard deviations of the unit vectors that define the component measured by camera b
$\sigma_a, \sigma_b, \sigma_c$	standard deviations of the directly measured components $U_{ma}, U_{mb}, U_{mc}$	$\sigma_{X_3}, \sigma_{Y_3}, \sigma_{Z_3}$	standard deviations of the unit vectors that define the component measured by camera c
$\sigma_{DC}$	detector dark charge noise in electrons	$\sigma_{\Delta f_i}$	uncertainty of the Doppler frequency shift at the $i$ th pixel
$\sigma_i$	total detector noise at the $i$ th pixel in electrons		
$\sigma_{PS_i}$	photon-statistical noise at the $i$ th pixel in electrons		
$\sigma_R$	standard deviation of the filtered diode signal		
$\sigma_{RO}$	detector readout noise in electrons		

# Doppler Global Velocimeter Development for the Large Wind Tunnels at Ames Research Center

MICHAEL S. REINATH

*Ames Research Center*

## Summary

Development of an optical, laser-based flow-field measurement technique for large wind tunnels is described. The technique uses laser sheet illumination and charged coupled device detectors to rapidly measure flow-field velocity distributions over large planar regions of the flow. Sample measurements are presented that illustrate the capability of the technique.

An analysis of measurement uncertainty, which focuses on the random component of uncertainty, shows that precision uncertainty is not dependent on the measured velocity magnitude. For a single-image measurement, the analysis predicts a precision uncertainty of  $\pm 5$  m/s. When multiple images are averaged, this uncertainty is shown to decrease. For an average of 100 images, for example, the analysis shows that a precision uncertainty of  $\pm 0.5$  m/s can be expected.

Sample applications show that vectors aligned with an orthogonal coordinate system are difficult to measure directly. An algebraic transformation is presented which converts measured vectors to the desired orthogonal components. Uncertainty propagation is then used to show how the uncertainty propagates from the direct measurements to the orthogonal components. For a typical forward-scatter viewing geometry, the propagation analysis predicts precision uncertainties of  $\pm 4$ ,  $\pm 7$ , and  $\pm 6$  m/s, respectively, for the  $U$ ,  $V$ , and  $W$  components at 68% confidence.

## Introduction

Aerodynamic research in wind tunnels often creates the need for measurement of the velocity field around a test vehicle. In large facilities, when the region of interest covers a large portion of the flow, velocity measurements are best made remotely. Optical, laser-based techniques are preferable because mechanical probes require large, costly traverse mechanisms and associated support hardware that may perturb the flow.

Laser Doppler velocimetry (LDV), a well known nonintrusive technique, has been used to measure flow fields in large facilities (ref. 1). This point measurement

technique suffers from several drawbacks, however, that limit its usefulness in these facilities. First of all, excessive amounts of run time can be consumed in mapping large areas with many survey points—long runs at a constant test condition can often be tolerated in the research environment of a small facility but not in the fast-paced environment of a large production testing facility. Furthermore, creating the proper seeding for LDV, which requires that individual particles be imaged within the sample volume, can be difficult, especially when measurement distances are long. Use of larger seed particles is often required to compensate for the weaker signals, and particle lag errors are introduced.

An improved nonintrusive technique is needed that can acquire data more rapidly than LDV, over the long measurement distances, without suffering performance degradation when smaller seed particles are used. There are presently two candidate techniques under development to fill this need: particle image velocimetry (PIV) and Doppler global velocimetry (DGV), also called planar Doppler velocimetry (PDV).

PIV is a technique that effectively tracks groups of particles and uses time of flight to measure two components of velocity in a plane (ref. 2). Ongoing development efforts will probably soon extend this capability to three components. While the requirement for more rapid acquisition of measurements is satisfied, the technique still requires imaging of individual seed particles or groups of particles; that is, the particles must be distinguishable from the surrounding background. This places strict performance requirements on the lens system, and also places an upper limit on the size of the measurement region that can be imaged at a particular distance. An intrusive placement of the camera inside a faired enclosure in the flow field can be used to shorten the measurement distance, but support structure, which may perturb the flow, is then needed. The technique requires some method of resolving reverse flow ambiguity, and also must have a special provision for handling measurement geometries that produce large out-of-plane velocity components. The technique, at its present stage of development, is best suited for precise mapping of measurement regions that are limited in size when only

two components of velocity are required in the plane of the measurement.

DGV is a Doppler-shift measurement technique that measures three components of velocity in a plane. No special provisions are required to handle large out-of-plane velocity components, and reverse-flow ambiguity does not exist. The technique does not require imaging of individual seed particles, so measurement distances are limited only by the need to achieve a specific final spatial resolution in the measurement plane. Micron and sub-micron-sized seed particles, which are the easiest sizes to produce in large volumes, can be used as seeding. The technique, at its present stage of development, is best suited for mapping and visualizing large regions of the flow when three components of mean velocity are of interest.

This paper summarizes the work that has been performed to develop and deploy a continuous wave DGV system for mean velocity measurement in the wind tunnels at the National Full Scale Aerodynamics Complex (NFAC) at Ames Research Center.

The author would like to thank Mark Bennett for software development and Jim Meyers, Joe Lee, Rich Schwartz, Angelo Cavone, Gary Fleming, and Mark Fletcher of Langley Research Center and Bob McKenzie of Ames for technical assistance.

## System Description

### General

DGV is a technique that can rapidly measure flow-field velocity distributions over large planar regions in the flow. All velocity measurements in the measuring surface are acquired simultaneously using laser sheet illumination and charged coupled device (CCD) detectors. Seed particles moving with the flow pass through the laser sheet and scatter light that is shifted in frequency by the Doppler effect. Some of this light is collected and imaged by a pair of CCD cameras. One of these cameras views the object plane directly and obtains a reference image that records intensity variations due to nonuniform illumination, nonuniform seeding, and image system defects. To include the effect of Doppler shift, the other camera views the same object plane through an absorption-line-filter cell containing iodine vapor. This cell acts as a spectral filter and causes the small shifts in Doppler frequency to produce measurable changes in light intensity on the CCD detector. An image is produced which records intensity variations that are a combination

of those caused by the iodine absorption and those caused by the nonuniformities mentioned above. By calculating the ratio of the two images pixel by pixel, only the Doppler shift information is retained. Velocity maps are computed from the gray-level image by converting the intensity of the image at a pixel to velocity using a simple linear transformation. By proper choice of lenses, the technique can be made to measure large two-dimensional regions of the flow. Three velocity components can be measured by installing three camera systems with different viewing angles.

### Laser

An argon laser capable of producing 25 watts of multiline power is tuned to the 514.5-nm line to create the laser beam. The laser is equipped with an intracavity, temperature-controlled etalon that can be adjusted manually to select a single frequency from the many longitudinal modes that occur at a 76.1-MHz spacing for this laser. The resulting single-frequency beam has a line width of about 10 MHz and an output power of 6 watts.

A closed-loop, water-to-water heat exchanger is used to dissipate the 55-kW heat load created by the laser and power supply. The heat exchanger unit isolates the filtered, deionized laser cooling water from the wind tunnel cooling water, which does not need to be conditioned. To save water, cooling water from a recirculating cooling tower system that has been treated with rust inhibitor and algaecides can be used in place of tap water.

### Beam-Delivery Optics

Figure 1 shows a diagram of the optics that create the laser sheet and provide a means for monitoring the beam frequency. Two beamsplitters are used to sample the main beam and create two low-power input beams for an optical spectrum analyzer and a reference iodine cell. Neutral density filters are used to adjust the low-power beam intensities, and a beam expander ensures that laser energy is spread throughout the volume of the iodine cell.

The laser frequency can be monitored using the optical spectrum analyzer to provide visual verification that a single-cavity mode has been properly selected. By viewing the output on an oscilloscope and manually adjusting the intracavity etalon, the operator can also change the beam frequency and visually verify that the selected adjustment has been made correctly. The frequency adjustment is limited by the mode spacing to discrete frequency jumps of 76.1 MHz.

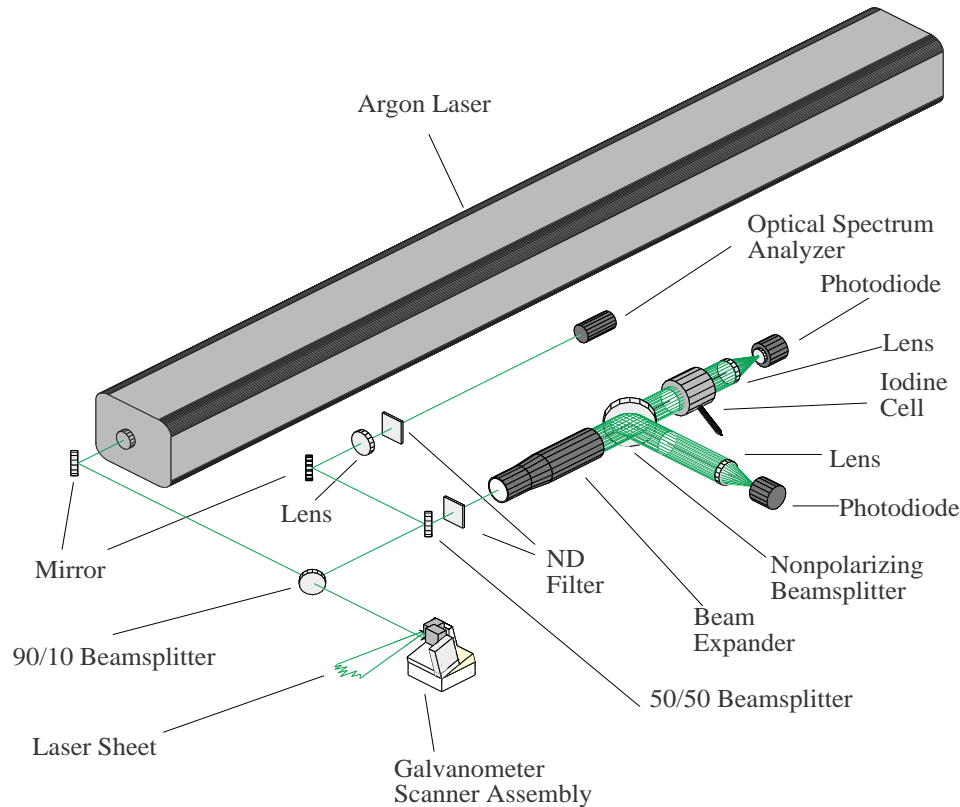


Figure 1. Diagram of the optical components that monitor the beam frequency and create the laser sheet.

The reference iodine cell also monitors the laser frequency,  $f_0$ , for detection of mode hops and other, more subtle, frequency changes. This frequency is needed as a reference to compute velocity because Doppler frequency is measured relative to this reference. Its value represents the frequency that would be measured for zero Doppler frequency shift. Therefore,  $f_0$  establishes the zero-velocity reference for all measurements and must be carefully measured to ensure accuracy. The measurement is made automatically each time images are acquired, using a 16-bit analog-to-digital (A-to-D) converter card. The card receives its input from the two silicon photodiodes that have a responsivity of 0.26 amp/watt at 514 nm and an active area of 10 mm<sup>2</sup>. The diode mounts are equipped with iris diaphragms that can be adjusted to minimize the influence of background light.

The laser sheet is generated by the scanner unit shown in figure 1. Two orthogonally mounted mirrors are driven by galvanometer scanners to create a sheet of time-averaged uniform intensity. This method is favored for this

application over use of cylindrical optics, which produce a nonuniform sheet with a Gaussian intensity profile. One scanner, driven by a saw-tooth wave form, oscillates to create the sheet while the other provides angular adjustment capability in a direction perpendicular to the plane of the sheet. By varying the amplitude of the waveform, the spread angle of the sheet can be adjusted from 0° to a maximum of 40°. The oscillating mirror is driven at a frequency of 80 Hz, which produces 160 passes of the beam per second, since one cycle equals two passes of the beam across the sheet. For standard RS-170 video, which runs at 30 frames per second, 2.7 beam passes occur per video field.

### Camera Optics

Three identical camera systems, one of which is shown in figure 2, acquire the raw DGV data images. Doppler-shifted light rays, scattered by seed particles in the object plane, are collected through the limiting aperture of the

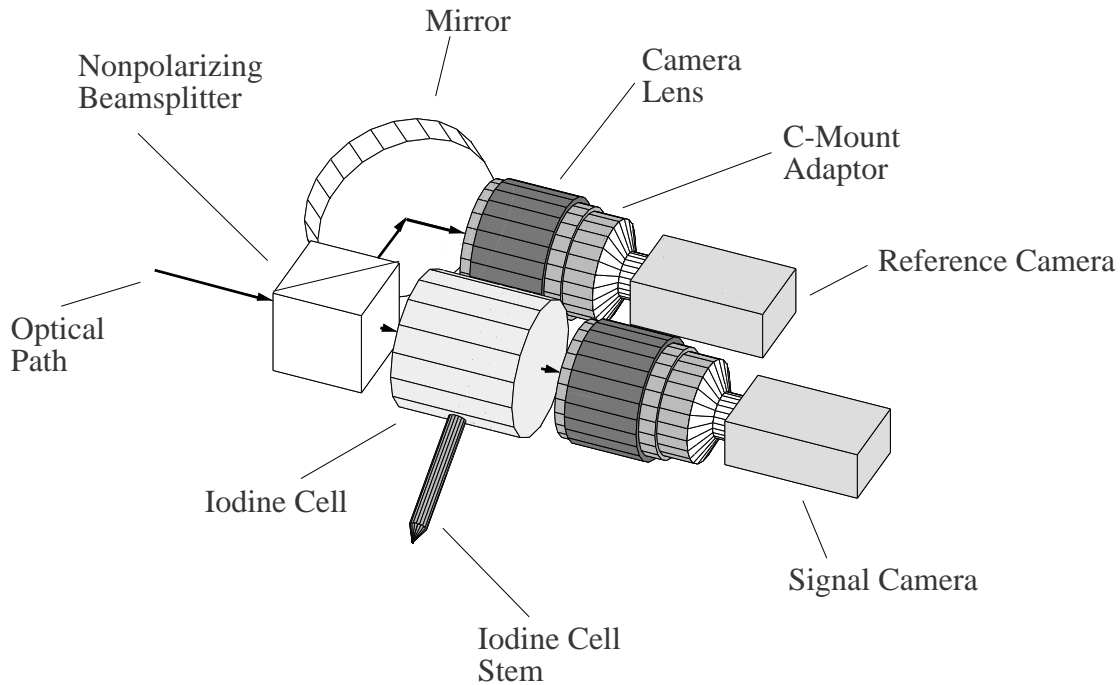


Figure 2. Diagram of the camera system optics (iodine-cell heaters, thermocouples, and enclosure are not shown).

nonpolarizing beamsplitter cube. The cube splits the image, creating two views of the object plane with a common optical axis. The beamsplitter coating is specified to reflect or transmit  $50 \pm 5\%$  of the incident radiation, with the *s*- and *p*-components of the reflected or transmitted rays matching to within 3% of each other; all of the cube surfaces are coated with an antireflection coating to eliminate ghost images. To create a more compact optical configuration, rays that are reflected from the beamsplitter coating are folded by a 4-in. diameter, one-tenth wave, aluminized mirror before entering the 8-bit, RS-170 video camera that acquires the reference image. Rays that are transmitted pass through the iodine absorption-line-filter cell and are imaged by the camera that acquires the signal image. Careful alignment of the components produces two images that are essentially identical, pixel for pixel.

The beamsplitter is an important component that can adversely affect the measurement accuracy. Incident rays are both reflected and transmitted, and their intensity ratio must remain constant, regardless of the polarization of the incident radiation, in order to avoid introducing measurement errors. This requirement must hold for rays that are incident parallel to the optical axis as well as for rays that enter at an angle near the edges of the field of view. In the early stages of system development, two different plate beamsplitters were tested that did not meet these performance requirements. In one case, polarization affected the

ratio of the reflected and transmitted intensities, and in the other case, the ratio was not constant for rays both parallel and at an angle to the optical axis.

The cylindrically shaped iodine cell is 3 in. in diameter, 2 3/4 in. in length, and is composed of fused silica. The optical-grade,  $1/4\lambda$ , 1/4-in.-thick windows are sealed to the cell body using an optical contacting method that does not require the application of heat, which could distort the window surfaces. A 3/8-in.-diameter, 2 3/4-in.-long tube-shaped projection, the cell stem, located on the side of the cylindrical body midway between the windows, is used to purge and evacuate the cell to  $10^{-6}$  torr or better and add the required distilled iodine (10 to 20 mg) during manufacture. During operation, the stem functions as the cold condensation area for the solid iodine crystals, which would otherwise condense on the window surfaces.

Heat is applied to the iodine cell using three band heaters and two copper jackets to increase and control the iodine vapor pressure and to prevent condensation of the iodine on the window surfaces. The copper jackets act as heat sinks and are placed over both the cell body and stem to distribute the heat and stabilize the heating process. Copper foil is wrapped around the stem to ensure a snug fit in its copper jacket; the stem temperature controls the vapor pressure of the iodine and must be held to a closer tolerance than that of the cell body. Two of the band heaters apply heat to the copper jacket that covers the cell body, and the third applies heat to the stem jacket. The

cell body and stem are heated to different temperatures by two controllers using type-J thermocouples for feedback. The body thermocouple is attached to the copper jacket that covers the cell body, and the stem thermocouple is attached to the tip of the glass at the end of the stem. The two temperatures are held to within  $\pm 0.2^\circ \text{F}$  of their set points. To minimize the influence of the ambient air temperature, the entire cell assembly is mounted inside a sheet metal enclosure that is filled with insulation material. An aluminum conduction path connects the base of the copper stem jacket to the bottom of the sheet metal enclosure so that heat may be conducted from the stem. Without this added conduction path, heat builds inside the enclosure and the stem temperature exceeds its set point.

### Data Acquisition Instrumentation

The data acquisition instrumentation is shown schematically in figure 3. Each of the six cameras, shown at the top of the figure, is connected to a synchronization generator to ensure that all frames are acquired simultaneously. Distribution amplifiers split the camera signals to create input for the frame grabbers and video switchers. By making a selection on the front panel of the video switchers, each of the camera images can be displayed on the two monitors shown. One video switcher controls display of the signal images, the images that are acquired through the iodine cells, and the other controls display of the reference images.

Three Macintosh desktop computers are used to acquire and process the images. The units are connected locally and communicate with each other via ethernet. Two of the units are slaved to the third, which acts as the master controller. Each is equipped with two RS-170, 8-bit, 640- by 480-pixel frame-grabber boards that are externally triggered by a control register in the master computer. By executing a single command, the master computer triggers all six frame grabbers simultaneously.

In addition to the frame grabbers, the master computer is also equipped with a 16-bit A-to-D converter card. This card indirectly measures the unshifted beam frequency using the reference iodine cell and other optical components shown at the bottom of figure 3. The signal and reference diodes provide two channels of analog input for the card. A two-channel oscilloscope is also used to monitor the inputs in real time. During the image-capture interval of 1/30 sec, the card is programmed to acquire 350 samples of each input signal. The ratio formed by dividing the signal by the reference value is a nondimensional measure of the unshifted beam frequency,  $f_0$ . This ratio is computed from the acquired samples along with the mean and standard deviation of the resulting distribu-

tion. The standard deviation is used to evaluate whether the laser frequency is stable during the image acquisition interval. If the standard deviation exceeds a predetermined value, a laser mode hop is assumed to have occurred, and the images are rejected.

The data acquisition and processing software was developed in-house and is written in C. The program consists of more than 200K lines of code and incorporates many useful features. For diagnosing performance and evaluating system alignment, a continuous capture mode can be selected. In this mode, the raw camera images are repeatedly captured and displayed on each computer using a user-selectable, false-color palette. Other features can be activated as required to display additional data in this mode. For example, in order to monitor parameters such as seed density and camera saturation, real-time histograms of all six raw images can be displayed. Also, to provide a first look at the velocity data, normalized images can be calculated and displayed; these images are calculated by forming the ratio of raw signal image to raw reference image without other processing. To display the data in a more conventional format, a profile plot through the normalized image can be displayed. This profile shows an x-y plot of the normalized value, in counts or meters per second, as a function of pixel position. Also shown on the plot are the corresponding signal and reference image intensities in counts. The selected profile line can be horizontal, vertical, or at an arbitrary angle. Finally, to monitor the stability of the laser frequency,  $f_0$ , data gathered from the reference iodine cell by the A-to-D card can be displayed.

The software also incorporates routines that set up and perform several required calibration procedures, which will be described in greater detail in a later section. These routines include a camera pixel sensitivity correction calibration, a flatfield or vignetting correction, an iodine response function calibration, and a spatial calibration required for image registration.

## Data Reduction

### Basics

Figure 4 shows the DGV measurement geometry for obtaining a single component of velocity. The vector  $\vec{V}$  represents the flow-field velocity at an arbitrary location in the image plane. The unit vectors  $\hat{l}$  and  $\hat{k}$  define the direction of the incident laser light ray and the direction of the ray of scattered light collected at the observation location, respectively. The vector  $\vec{U}_m$  is the component of the total velocity vector  $\vec{V}$  that is measured for this geometry.



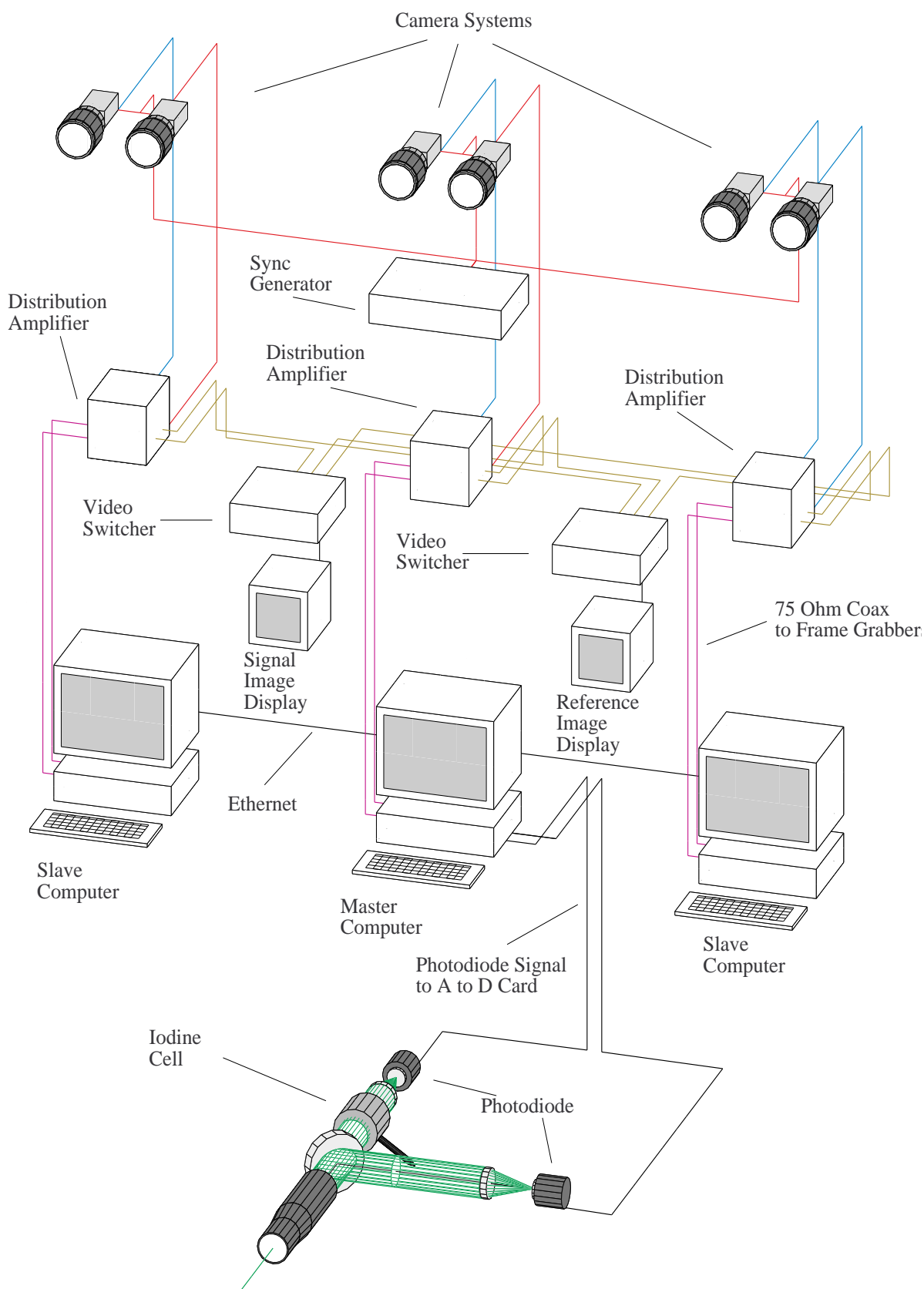


Figure 3. Data acquisition instrumentation.

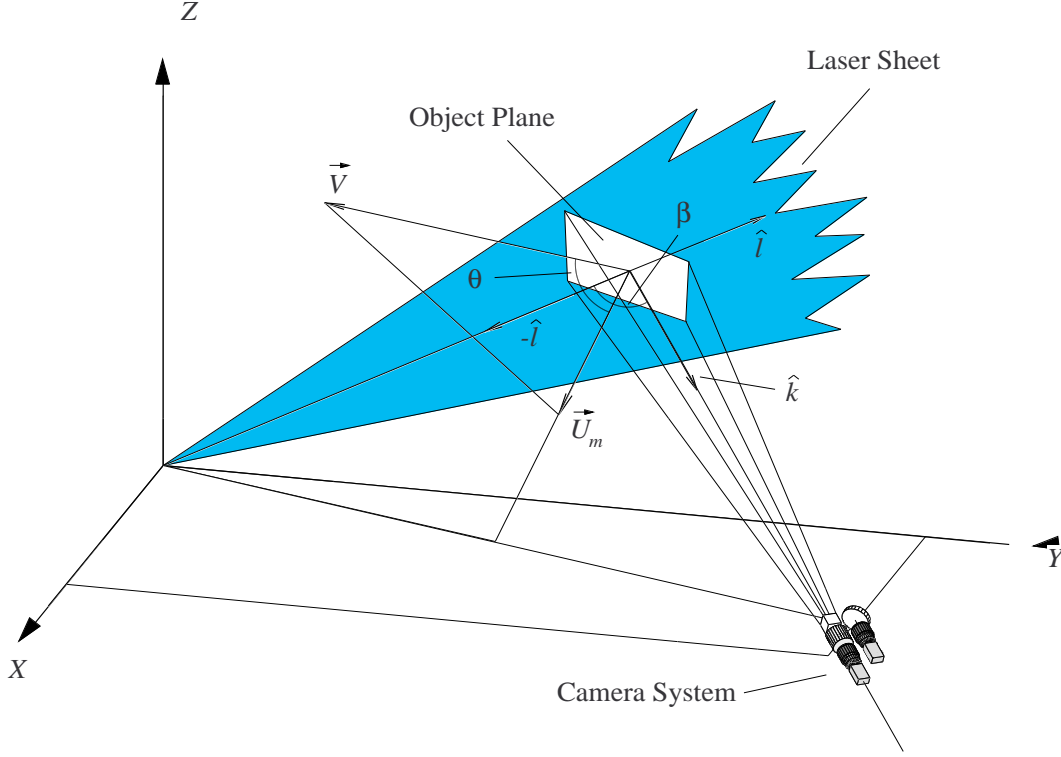


Figure 4. DGV measurement geometry for obtaining a single velocity component.

The equation that relates Doppler frequency shift to the parameters of velocity and geometry can be written as (refs. 3 and 4)

$$\Delta f = \frac{1}{\lambda_0} \vec{V} \cdot (\hat{k} - \hat{l}) \quad (1)$$

where  $\Delta f$  is the Doppler shift and  $\lambda_0$  is the wavelength of the incident laser light. The magnitude of measured component  $\bar{U}_m$  is given by the dot product of the vector  $\vec{V}$  with the direction  $(\hat{k} - \hat{l})$ . By simplifying and rearranging, the equation can be written as

$$U_m = \frac{\lambda_0 \Delta f}{2 \cos\left(\frac{\beta}{2}\right)} \quad (2)$$

where  $\beta$ , the angle between the incident ray and the scattered ray, is shown in figure 4.

Velocity information is extracted from DGV image data in a two-step process. First, the measured intensity at a pixel is converted to Doppler frequency shift. Then,

equation (2) is used to compute velocity. The conversion to Doppler shift is made using two iodine cell response functions, one from the cell associated with the camera and one from the cell measuring the  $\lambda_0$  reference value. Figure 5 shows typical iodine cell response functions and depicts graphically the process of converting measured intensity to Doppler shift. Both response curves are measured simultaneously prior to acquiring image data by adjusting the laser etalon while viewing the discrete mode hops on the optical spectrum analyzer and physically stepping the laser through the frequency range covered by the iodine spectral feature. Since the modes are known to be spaced at 76.1 MHz for this laser, relative frequencies can be calculated for each mode; the absolute frequency need not be known, since both curves have the same arbitrary zero-frequency reference, and the conversion from image intensity to frequency ultimately yields a frequency shift and not an absolute frequency. The Doppler shift is obtained by subtracting the zero-velocity relative frequency,  $f_0$ , from the relative frequency,  $f_D$ , of the Doppler-shifted light.

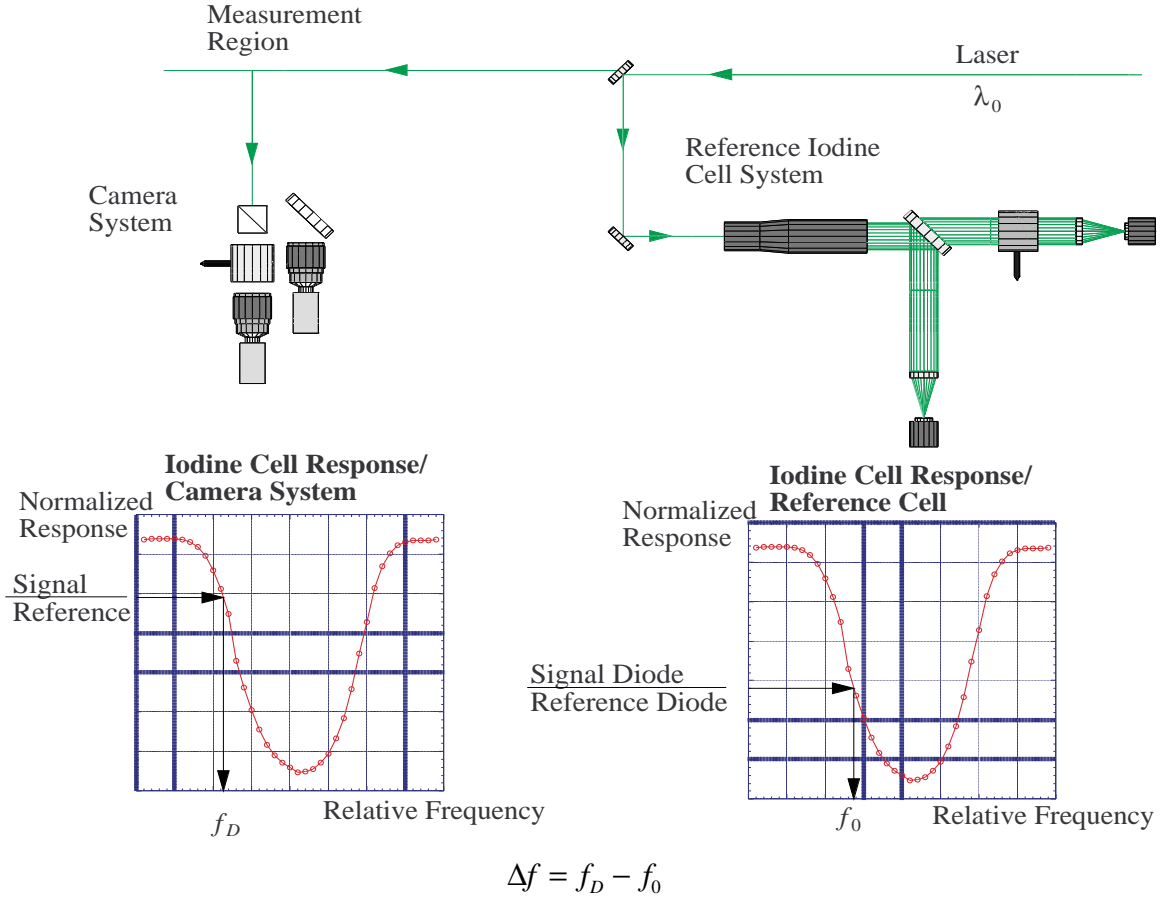


Figure 5. Overview of the conversion from image intensity to Doppler frequency shift.

### Reduction of Raw Images

Raw DGV images are processed by the sequence of steps summarized in the flow chart of figure 6. The procedure begins with the separation of each interlaced video frame into two fields. The fields are essentially two separate images that are acquired sequentially at half the resolution and exposure of the full video frame. Since the 1/60-sec frame exposure is long compared with the changes in flow-field velocities, each field must be treated as a separate image (ref. 5).

The raw images have a background component that is subtracted prior to further processing. This component is obtained by averaging multiple individual background images, acquired shortly before or after acquisition of the raw data images to ensure identical laser power, ambient illumination level, and geometry. The background images are acquired while no seeding is present in the field of view of the cameras or the path of the laser sheet. The laser sheet, however, must be present to include its contribution to ambient illumination level. Even if no primary diffuse reflections are in the view of the cameras,

scattering from surfaces can contribute to the overall illumination level, as can the flare that is produced by the sheet as it passes through the test section window. Their contributions should be included in the background images.

Raw data images are corrected for pixel sensitivity variations using a linear correction technique. Ideally, since the CCD array is being used as a photogrammetric detector, all pixels should have the same radiometric response to a given incident intensity. Unfortunately, laboratory measurements show that radiometric pixel sensitivity varies across the CCD detector from pixel to pixel. If this variation is not corrected, it introduces a component of intensity variation across each data image that is artificial. To avoid this, pixel sensitivities are corrected using a simple technique that makes use of the linear nature of the CCD response. First the actual radiometric response of each pixel is measured using the average of many images at two illumination levels, low and high. Then a linear correction to each pixel response

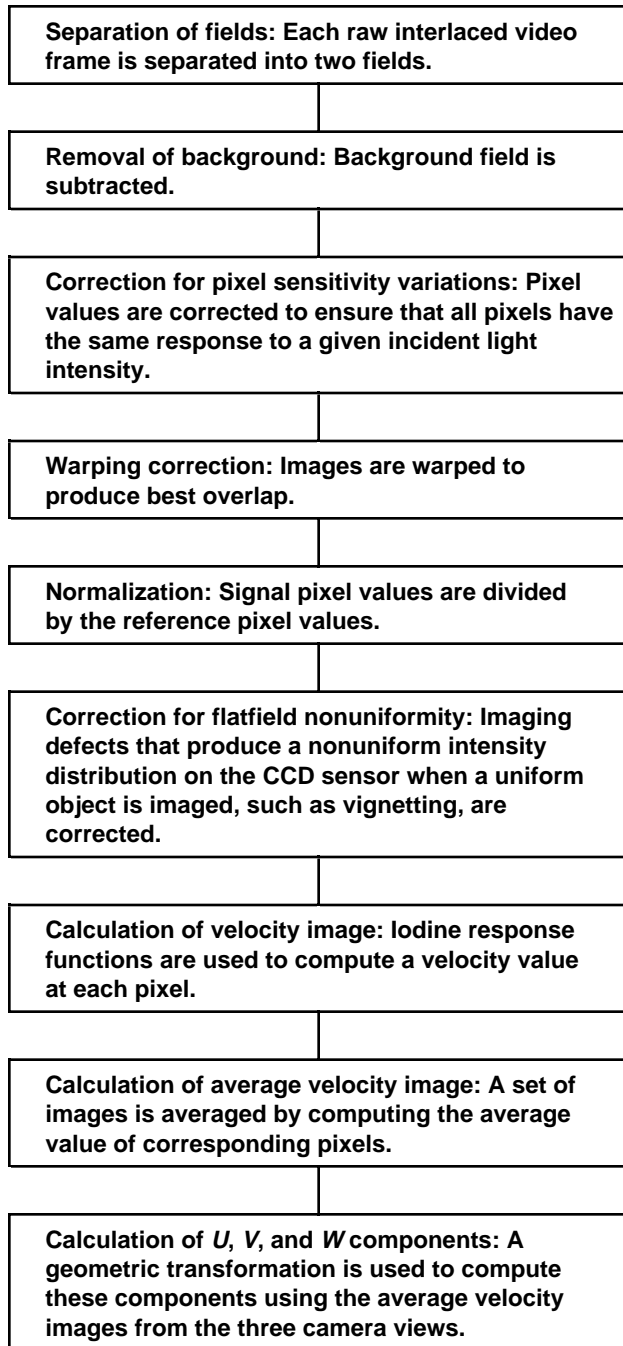


Figure 6. Sequence of processing steps to convert raw DGV images to velocity.

is computed by imposing the requirement that the corrected pixel response be the same as the mean radiometric response of the entire detector. Overall response of the CCD detector remains unchanged, but the artificial variance is eliminated.

The next step in processing raw images is a warping procedure that performs two functions. Data images are warped to ensure best overlap, to correct for simple misalignment and optical distortion, and the oblique view of the object plane is numerically rotated to simulate a perpendicular view. The warping technique, known as pixel filling (ref. 6), is used to perform the geometric transformation procedure in two steps. First, a bilinear interpolation is used to map each data image to a grid of control points, which is acquired by imaging a target of evenly spaced reseau marks placed in the image plane. Second, a bilinear interpolation is used to calculate the gray level of each pixel in the warped image using the gray-level values of the four nearest pixels in the unwarped image. A similar type of warping correction has been used previously to correct geometric and photometric distortions as described in references 7–9.

The normalized image is then computed by forming the ratio of signal-image pixel value to reference-image pixel value.

In the next step of processing, a flatfield correction is performed which removes vignetting and corrects for losses in the collection optics that may not be uniform across the image. This correction is different from the pixel sensitivity correction, which compensates for imperfections that originate on the CCD chip itself. The flatfield defects introduce a component of nonuniformity that is caused by the collection optics and not by the CCD detector. If not removed, this nonuniformity adds to the uncertainty of the radiometric measurement. The correction is performed by multiplying the normalized image by the inverse of the flatfield correction image. To obtain the correction image, the laser frequency is adjusted to produce maximum transmission through the iodine cell at the top of the response curve. Images are acquired while flow velocity in the seeded region of the object plane is zero or near zero and processed up to and including the normalization; the process requires averaging of many images to reduce the photon statistical noise. The resulting image contains intensity variations caused by effects other than Doppler shift and pixel sensitivity. In a perfect imaging system, this image would be completely uniform. In reality, the central region is normally a few counts brighter than the edges.

As added benefit, an image processed and corrected using the flatfield correction image is independent of the camera/frame-grabber effective gain after the correction. This is important in order to eliminate the problems that would occur as gains of the cameras and frame grabbers drift with time. In general, the normalized value at a given pixel can be written as (ref. 10)

$$n = \frac{\text{Signal Pixel Intensity}}{\text{Reference Pixel Intensity}} = \frac{G_S \cdot T(f_D)}{G_R} \quad (3)$$

where  $T(f_D)$  is the iodine filter transmission at the Doppler frequency, and  $G_S$  and  $G_R$  are the effective gains of the signal and reference camera/frame-grabber combinations, respectively, in counts per unit of incident intensity. Similarly, the flatfield correction image is given by

$$n_{ff} = \frac{G_S \cdot T(f_{\max})}{G_R} \quad (4)$$

where  $T(f_{\max})$  is the iodine filter transmission at the frequency  $f_{\max}$  ( $f_{ma}$  is located outside the iodine absorption well at the top of the response curve where peak transmission through the cell occurs). When the correction is made, the normalized value at a given pixel, equation (3), is multiplied by the inverse of the flatfield correction image at the same pixel, equation (4):

$$n_{\text{corrected}} = \frac{T(v_D)}{T(v_m)} \quad (5)$$

The two effective gain parameters cancel, and the resulting image is independent of the effective gain. Since gain can drift with time, flatfield images must always be acquired immediately before or after acquiring data images.

After an image is corrected for flatfield nonuniformities, image intensity must be converted to velocity before any averaging of multiple images can be performed. The velocity computation must be performed first because each image has its own zero-velocity reference,  $f_0$ , which is normally not common to all images because of laser frequency drift and the possibility of mode hopping. A two-step process is used for the computation, which is performed at each pixel in the image. In the first step, Doppler shift is calculated using the corrected normalized pixel intensity,  $n_{\text{corrected}}$ , and frequency measured by the reference cell,  $f_0$ , as shown in figure 5. Cubic B-Splines are used to interpolate between data points on the response curves. In the second step, equation (2) is used to convert the Doppler shift to velocity.

Once all images have been converted to velocity, averaging of images that form an ensemble at a particular condition can be performed to reduce statistical uncer-

tainty. The result is the directly measured component,  $\vec{U}_m$ , shown in figure 4. This vector is normally at an angle relative to the wind tunnel coordinate system for each of the three camera views. The final processing step takes the components from these views and converts them to the components  $U$ ,  $V$ , and  $W$  in the wind tunnel coordinate system directions using a geometric transformation. This transformation is obtained in the following way. First, three scalar products of the unknown total velocity vector  $\vec{V}_T$  with the unit vector directions of each camera view are formed. Simplification yields the three linear equations

$$X_1 \cdot U + Y_1 \cdot V + Z_1 \cdot W = U_{ma}$$

$$X_2 \cdot U + Y_2 \cdot V + Z_2 \cdot W = U_{mb}$$

$$X_3 \cdot U + Y_3 \cdot V + Z_3 \cdot W = U_{mc}$$

where

$U_{ma}$  = magnitude of the measured component from camera view a

$U_{mb}$  = magnitude of the measured component from camera view b

$U_{mc}$  = magnitude of the measured component from camera view c

$X_1, Y_1, Z_1$  = unit vector components defining the direction of  $\vec{U}_{ma}$

$X_2, Y_2, Z_2$  = unit vector components defining the direction of  $\vec{U}_{mb}$

$X_3, Y_3, Z_3$  = unit vector components defining the direction of  $\vec{U}_{mc}$

in the three unknown quantities  $U$ ,  $V$ , and  $W$ . Solving the system for the unknown components yields the transformation equations

$$U = \frac{\begin{bmatrix} U_{ma}(Y_2Z_3 - Y_3Z_2) - U_{mb}(Y_1Z_3 - Y_3Z_1) \\ + U_{mc}(Y_1Z_2 - Y_2Z_1) \end{bmatrix}}{\begin{bmatrix} X_1Y_2Z_3 - X_1Z_2Y_3 - Y_1X_2Z_3 + Z_1X_2Y_3 \\ + Y_1Z_2X_3 - Z_1Y_2X_3 \end{bmatrix}} \quad (6)$$

$$V = \frac{\begin{bmatrix} X_1(U_{mb}Z_3 - U_{mc}Z_2) - X_2(U_{ma}Z_3 - U_{mc}Z_1) \\ + X_3(U_{ma}Z_2 - U_{mb}Z_1) \end{bmatrix}}{\begin{bmatrix} X_1Y_2Z_3 - X_1Z_2Y_3 - Y_1X_2Z_3 + Z_1X_2Y_3 \\ + Y_1Z_2X_3 - Z_1Y_2X_3 \end{bmatrix}} \quad (7)$$

$$W = \frac{\begin{bmatrix} X_1(U_{mc}Y_2 - U_{mb}Y_3) - X_2(U_{mc}Y_1 - U_{ma}Y_3) \\ + X_3(U_{mb}Y_1 - U_{ma}Y_2) \end{bmatrix}}{\begin{bmatrix} X_1Y_2Z_3 - X_1Z_2Y_3 - Y_1X_2Z_3 + Z_1X_2Y_3 \\ + Y_1Z_2X_3 - Z_1Y_2X_3 \end{bmatrix}} \quad (8)$$

for the final processing step of figure 6.

Computation of the  $U$ ,  $V$ , and  $W$  components is simplified slightly, at the present stage of development, by treating the unit vector components as constants throughout the image. This approximation neglects the small unit vector direction changes from pixel to pixel that occur because of small changes in viewing direction and laser propagation direction from one pixel to the next. For large viewing distances, these angle changes are very small and, to a first approximation, can be neglected. Therefore, to simplify processing, viewing angle and laser propagation direction are assumed constant over the image. Their values are taken at the center of the image.

## System Calibration

### Pixel Sensitivity Calibration

The pixel sensitivity calibration determines the slope and intercept of the actual linear radiometric response of each CCD pixel. These values provide the required input for the pixel sensitivity correction described above. The procedure consists of acquiring average images from each camera at two illumination levels (refs. 9 and 11). An incandescent bulb is placed about 20 ft from the camera to simulate a point source, and a diffuser is substituted in place of the lens to produce a fairly uniform illumination of the CCD sensor; the illumination level need not be completely uniform because response of each pixel is linear. The software includes a routine that processes the images and stores the required files for later use.

Figure 7(a) shows a typical CCD sensor response to uniform illumination. The image and corresponding histogram were produced by carefully illuminating the CCD sensor using the uniform output of an integrating sphere. Intensity is spread over six levels because of variation of pixel sensitivity. Gray-level contouring, which would be difficult to discern in the normal gray-level image, is accentuated using a color palette. Figure 7(b) shows the same image after application of the pixel sensitivity correction. The image is clearly flatter, and the histogram shows that intensity is confined to only three levels after the correction. A slight contouring remains due to integer roundoff of the 8-bit gray-level values.

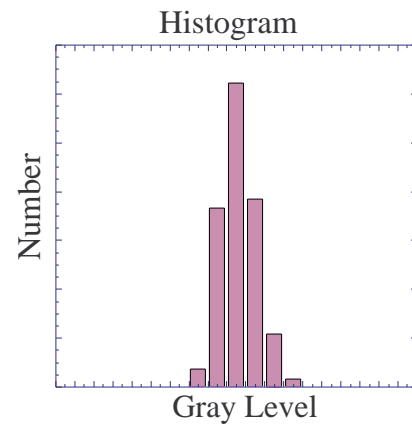
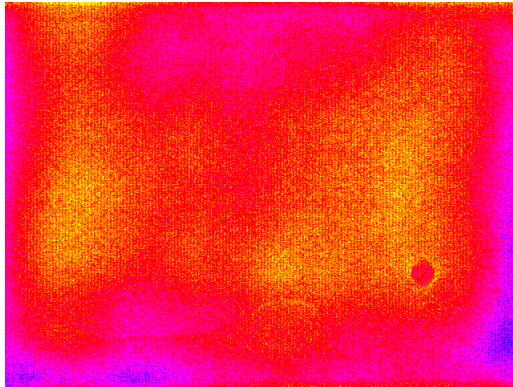
### Spatial Calibration

The spatial calibration provides the numerical input required to perform image warping during processing of raw images. Recall that warping adjusts simple misalignment of image overlap, corrects optical distortion differences that may be present in the two camera views of each camera pair, and numerically rotates the images to simulate an orthogonal view.

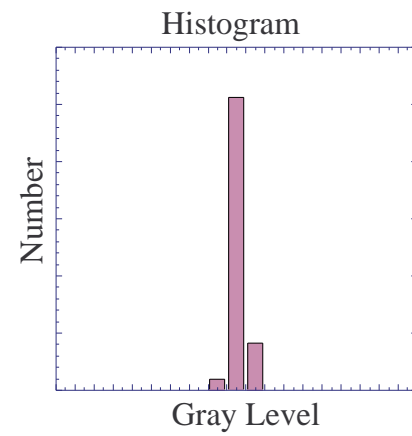
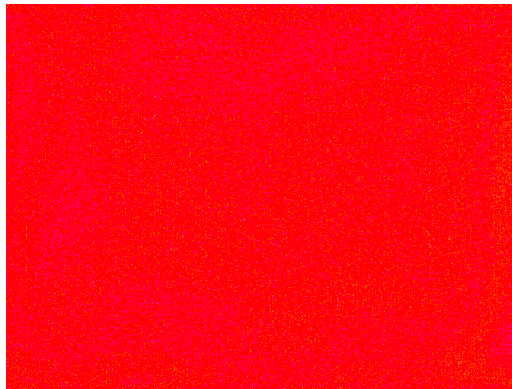
The spatial calibration is acquired by imaging a grid of regularly spaced reseau marks. The plane of the grid is oriented to coincide with the plane of the laser sheet, and the size of the grid must cover the field of view. In general, the reseau marks must be visible from both front and back surfaces of the grid to accommodate viewing geometries that have cameras mounted on both sides of the laser sheet.

The spatial-calibration images are acquired after all camera alignment and viewing angle adjustments have been made. The viewing angle of each camera pair is coarsely adjusted to center the image on the center of the grid. Fine adjustments are made to maximize the area of the image that is common to all three views, since processing to the final  $U$ ,  $V$ , and  $W$  velocities requires input from each camera view. Any portion of the object plane that is not part of the union of all three images will be excluded from the final velocity image, limiting its size. Thus care must be taken to fine-tune the viewing geometry to maximize the common area while also insuring that this area is centered on the region of interest.

Once the viewing geometry is fixed, spatial-calibration images of the grid are simultaneously acquired by all cameras and saved to disc. The software processes the images by first converting the gray-level images to bi-level images and then automatically scanning for the reseau marks to locate their centroids in image coordinates. Some operator interaction is necessary during the processing to validate that no reseau marks are skipped by the scan. Images are displayed during the process, and rectangles are drawn around the marks as they are located by the scan, enabling the operator to see at a glance any marks missed by the scan. Prior to initiating the scan, the operator is required to identify a typical reseau mark. The software measures the area of the mark in pixels and uses this value as an aid in performing the scan. The operator is also required to identify the portion of the grid that is common to the three viewing directions. The scan then proceeds to locate the centroids only within this region. Sample images are shown in figure 8.



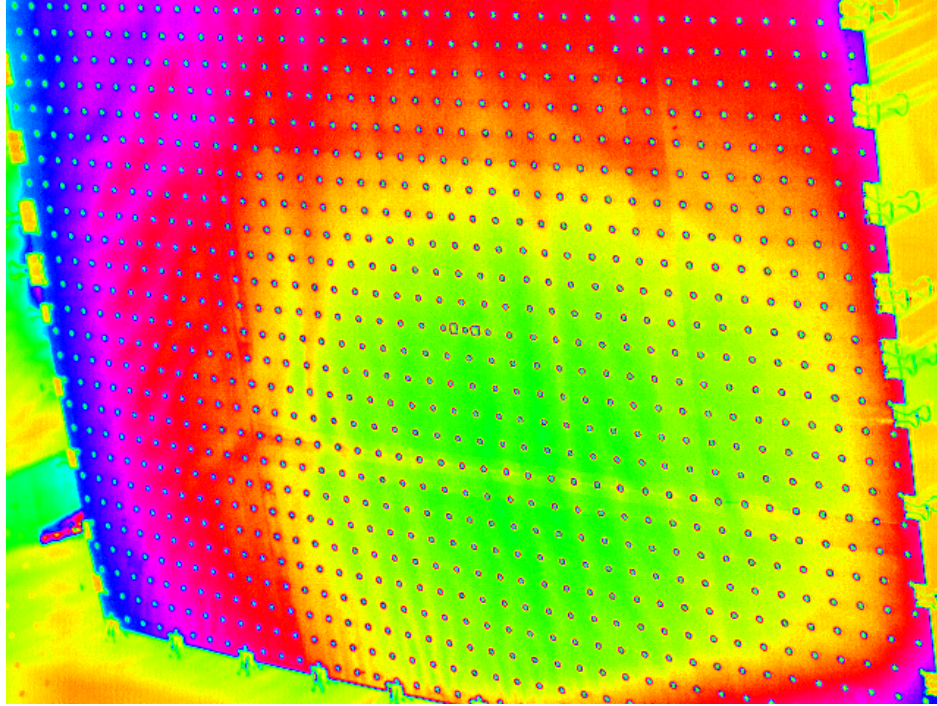
*(a) Image before pixel sensitivity correction.*



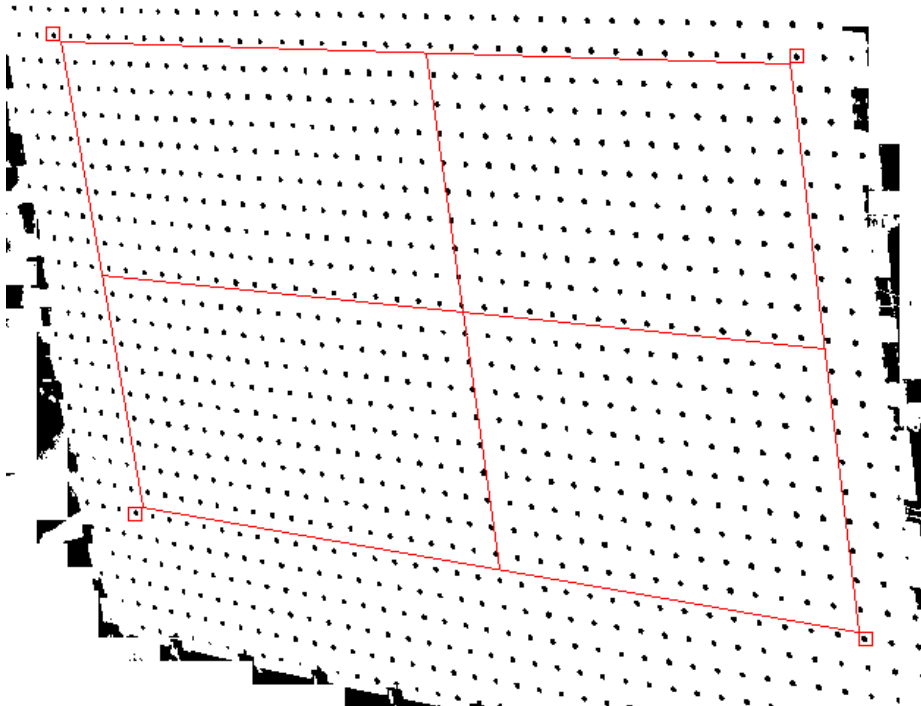
*(b) Image after pixel sensitivity correction.*

*Figure 7. Response of CCD sensor to uniform illumination illustrating the effectiveness of the pixel sensitivity correction.*





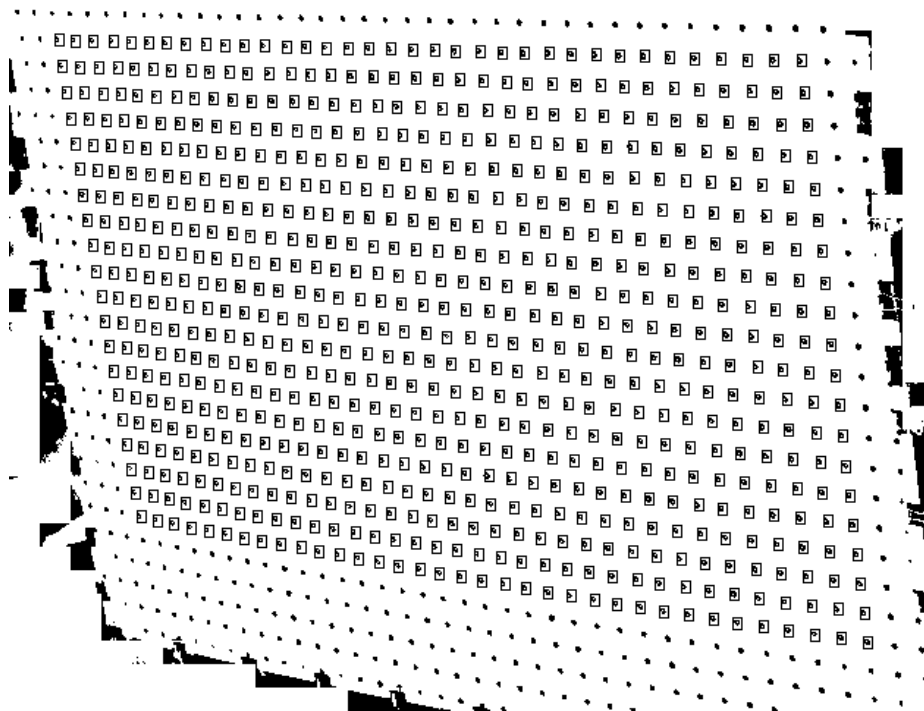
(a) Gray-level, spatial-calibration image.



(b) Bi-level image showing software tool that sets image boundary.

Figure 8. Sample images illustrating the spatial calibration.





(c) Scan result showing rectangles that identify all marks located by the scan.

Figure 8. Concluded.

The processing of calibration images can be simplified if care is taken to illuminate the grid surface uniformly when images are acquired. During processing, the 8-bit images are converted to bi-level images using a thresholding algorithm that cannot tolerate large gradients caused by nonuniform illumination. In practice, when testing in a large wind tunnel environment, illumination of the surface may not be ideal. To compensate, the software partitions the images and performs the bi-level conversion separately in each partition. Operator input is required to select the number of partitions using trial and error if the illumination is highly nonuniform.

The processing is finished when all centroid coordinates have been located in all six images and output to a file. The warping algorithm uses these values, and the coordinates of the grid point centroids as they appear in the actual grid, to perform the warping procedure. The images are constrained to match at the grid points before and after warping. Bilinear interpolations are performed between the points, as described previously.

### Iodine-Cell Response Calibration

Each iodine cell is heated to increase and control the vapor pressure of the iodine contained within the cell. Response function shape is strongly dependent on the

iodine vapor pressure. Since iodine vapor pressure changes significantly with temperature, it is necessary to accurately control the cell temperature to ensure stability of the response curve.

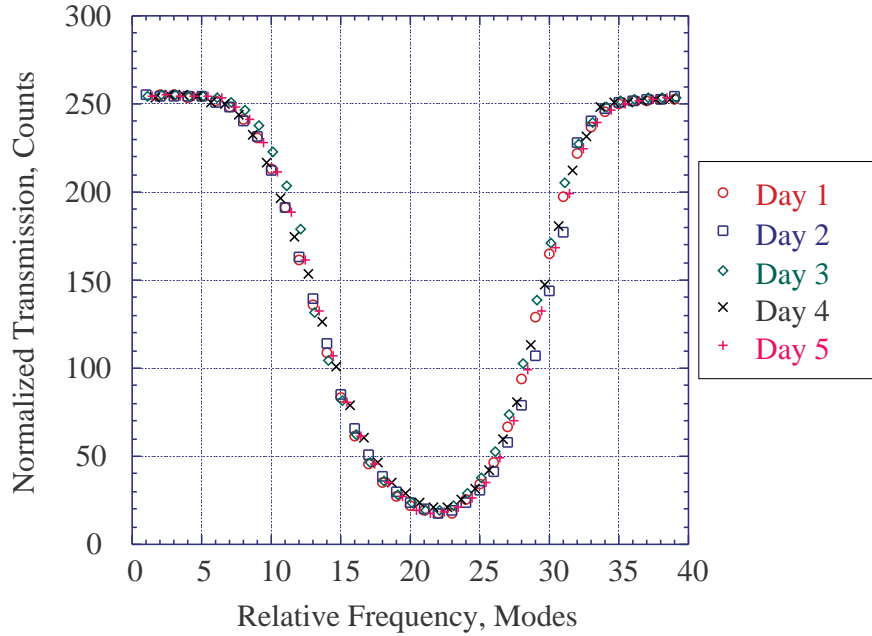
The iodine vapor pressure is determined by the temperature of the coldest part of the cell where iodine condensation occurs. Temperature of the solid iodine at this point determines the response of the cell and must be carefully controlled. To ensure that this cold location occurs at the stem tip, the cell body is heated to a higher temperature than the stem. The remainder of the cell must be at a temperature large enough to prevent condensation of the iodine on the window surfaces, which are exposed to the ambient temperature. This temperature is otherwise unimportant and does not influence the shape of the response curve as long as the tip is not affected.

Experience has shown that a value of about 150° to 160° F works well for moderate ambient temperatures. If operations are being conducted where ambient temperatures are unusually low, frequent inspection of the cell windows for iodine crystals should be made. When crystals are present on the window surface, vapor pressure inside the cell may be lower than the level indicated by the stem temperature, and the response of the cell may be different than expected. Also, the crystals on the window surface tend to cast a shadow on the surface of the

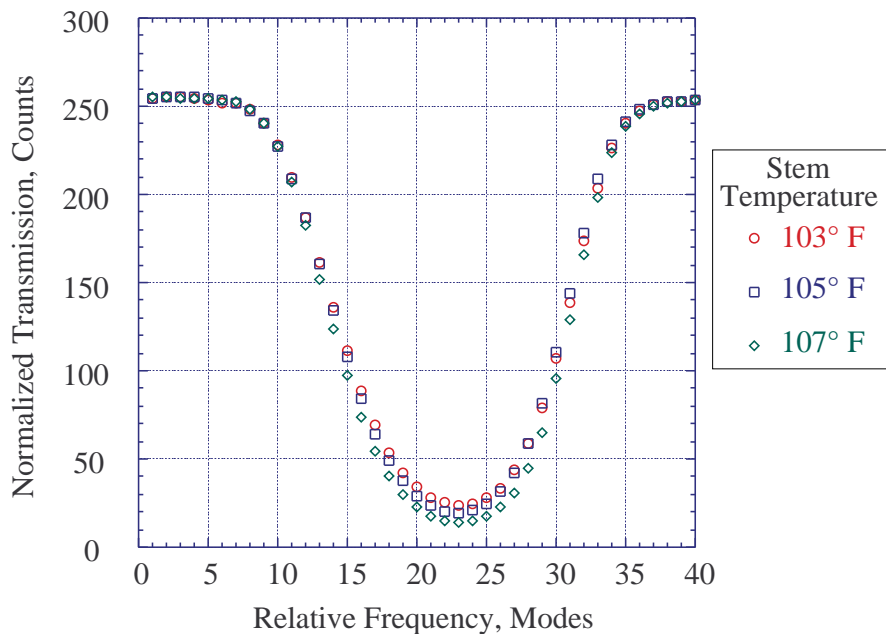
photodiode detector, producing an erroneous indication of intensity transmitted through the cell.

Figure 9 shows typical iodine cell response curves to illustrate repeatability and temperature sensitivity. The

measured response of a particular cell taken several times over a period of 5 days is shown in figure 9(a) for a stem temperature of 105° F. The same cell response, measured at three different stem temperatures, is shown in figure 9(b).



(a) Iodine response measured five times on consecutive days.



(b) Iodine response measured at three different stem temperatures.

Figure 9. Typical iodine response curves showing repeatability and sensitivity to stem temperature (cell body temperature = 160° F).

To minimize the possibility of response-curve drift, the response function is measured immediately prior to acquiring data using the following procedure, which simultaneously measures the response functions of all four system cells. After the viewing geometry has been finalized and the spatial calibration has been performed, a uniform white target is placed in the object plane at the sheet location. The laser is used to illuminate an area on the surface of the target large enough to cover the common field of view of the cameras. Images are acquired from all cameras while manually stepping the laser through its discrete frequencies. About 40 frequency steps are required to cover the complete response curve. Images are processed as described in the previous section, but processing ends with the normalization step. The pixel values are then averaged within a rectangular region of each image to yield the response for the corresponding relative frequency. The region is selected as large as possible but must exclude any pixels that are not imaging the laser reflection. The resulting curves are normalized using the value outside the absorption well where the plateau occurs at peak transmission. This final step is equivalent to, and produces the same result as, the flatfield correction.

### Flatfield Calibration

The flatfield calibration image is required to correct for vignetting and other losses in the collection optics that produce a variation in measured intensity that is not present in the object plane. The calibration image is acquired immediately after acquiring data images while seeding is still present in the wind tunnel, using the aerosol itself as the flatfield target. Wind tunnel speed is reduced to a level just large enough to keep the seeded air moving through the test section, and the laser is set to a frequency outside the absorption well of the iodine on the response-curve plateau where maximum transmission occurs. Since the laser frequency has been moved out of the absorption well, cell transmission remains constant for the small Doppler shifts that result because of the low-speed flow. A series of images is acquired and processed up to the normalization step in the processing sequence. The resulting images are then averaged together to produce the final flatfield image.

### Measurement Uncertainty

A statement specifying the magnitude of an experimentally measured parameter must include a quantitative description of the uncertainty in order to add value and credibility to the measurement. When uncertainty is reported, it is normally expressed as an interval within

which the *true value* of the measured parameter is expected to fall at a specified level of confidence. Measurement error is then the difference between this true value, rarely known exactly, and the measured value. It is composed of a component arising from bias or systematic effects and a component arising from scatter or random effects. These errors are estimated and combined to characterize the uncertainty for a particular measurement by using the equation (ref. 12)

$$U_i = \pm (B_i^2 + P_i^2)^{1/2} \quad (9)$$

where

$B_i$  = bias limit (estimated so that the experimenter is confident that in 95 out of 100 measurements the true value of the bias error, if known, would be less than  $|B_i|$ )

$P_i$  = precision limit =  $KS_i$

$K$  = coverage factor (2 for large sample sizes and 95% confidence)

$S_i$  = standard deviation of the distribution of measurements of the parameter

and the subscript  $i$  denotes the  $i$ th measurement of the parameter in an ensemble of measurements.

The task of computing the uncertainty of DGV measurements can be broken down into three basic steps. In the first step, the CCD camera radiometric measurement uncertainty is characterized. Next, a computation is performed to show how this uncertainty propagates into the Doppler shift and computed velocity. Finally, since the measured velocities are normally not orthogonal, the third step requires characterizing how this uncertainty propagates through the geometric transformation to computed orthogonal components.

### CCD Radiometric Measurement Uncertainty

The CCD radiometric measurement uncertainty is computed by combining estimates of the random and systematic components that limit the accuracy of the measurement using equation (9). The systematic component is the nonrandom bias that affects all measurements equally and is very difficult to estimate in this case. It is caused, for example, by secondary scattering from windows, walls, or model surfaces that are illuminated by laser light scattered from the aerosol itself or from diffuse or specular reflections of the laser sheet. Proper design of the experiment can minimize or eliminate these components. Therefore, bias is assumed to be negligible for the radiometric measurement, and estimation of the uncertainty is limited to determining

the random effects that govern the precision of the measurement.

The random uncertainty component can be estimated as shown in references 10 and 13 by summing the statistically independent uncertainty components (noise sources) of the CCD detector; the term *noise* in this case is used as a synonym for *standard deviation* and quantifies the measurement scatter. The noise sources can be summed as variances (ref. 14) to yield the variance of the radiometric measurement (ref. 13) as shown in the following equation.

$$\sigma_i^2 = \sigma_{RO}^2 + \sigma_{PS_i}^2 + \sigma_{DC}^2 \geq \frac{G_{AD}^2}{12} \quad (10)$$

where

$\sigma_{RO}$  = detector readout noise in electrons

$\sigma_{PS_i}$  = photon-statistical noise in electrons

$\sigma_{DC}$  = dark-charge noise in electrons

$G_{AD}$  = A-to-D conversion gain in electrons/count

and the subscript  $i$  denotes the  $i$ th pixel in the CCD array.

The constant, 12, converts the rectangular quantization interval of  $\pm 1/2$  count to variance, assuming that occurrences of the measured parameter value are continuously distributed and equally likely over this digitization interval of one count (ref. 15). At a given pixel, the random uncertainty component is determined by the sum of the noise sources or the A-to-D gain, whichever is greater. To compute the total radiometric uncertainty at a pixel, the value of each term must first be estimated.

Readout noise originates when charge packets that accumulate at each pixel are moved off the detector surface in the process of reading the image. Values are well documented for many slow-scan, scientific-grade cameras but lack for cameras that operate at video rates. An estimate can be made, however, since this noise increases in proportion to the square of the readout frequency (ref. 16). Scaling a nominal slow-scan value to the higher readout rate yields a noise of about 110 electrons.

Photon-statistical noise is inherent to the random process of photon emission and detection. Its value is statistically equal to the square root of the average number of photo-electrons accumulated during an exposure (ref. 13). This accumulation will, in general, contain a background component composed of a mean value and an associated noise, in addition to the accumulation due to the primary signal. The mean background component is subtracted during processing but the noise remains. An estimate of

the total photon-statistical noise is made by assuming that parameters such as seed density, laser power, and camera aperture are adjusted to produce an exposure that fills the pixels of the unfiltered camera to two-thirds their full-well capacity. Further, it is assumed that the laser frequency is adjusted to set the transmission of the iodine cell to about 50%, producing an exposure of one-half this value in the filtered camera. The effective full-well capacity of the cameras will later be shown to be about 30,000 electrons. Thus, the photon-statistical noise is 140 and 100 electrons, respectively, for the two cameras.

Dark-charge noise, to a first approximation, doubles for every 7° C increase in the operating temperature of the CCD array and is directly proportional to the surface area of the pixels (ref. 15). The video cameras used for this development have a pixel size of 11 by 13  $\mu\text{m}$  and operate at a temperature of 33° C at an ambient temperature of 21° C. About 30 electrons will accumulate as dark-charge noise during the video exposure period under these conditions.

The A-to-D gain is estimated, to a first approximation, using the following procedure. An ensemble of dark images is acquired while blocking all light from the camera sensor. The standard deviation of the distribution of pixel values over the ensemble is computed for several pixels. These values are averaged to yield an estimate, in counts, of the mean readout and dark-charge noise. The result, 0.98 count, is divided into the total radiometric measurement noise, computed using equation (10) and the estimates given above, to yield 120 electrons/count, to two significant figures.

An alternate method of estimating the A-to-D gain is presented in reference 13 using the following equation

$$\sigma_i^2 = \frac{\langle C_i \rangle}{G_{AD}} + \frac{\sigma_{RO}^2 + \sigma_{DC}^2}{G_{AD}^2} \quad (11)$$

where  $\langle C_i \rangle$  represents the mean level in counts at the  $i$ th pixel. The A-to-D gain is obtained from a plot of total radiometric variance versus mean signal level by inverting the slope of a least squares linear fit. Figure 10 shows a sample plot of this type for various mean signal levels ranging from near zero to near saturation. An integrating sphere with regulated illumination was used to acquire 100-image ensembles at each signal level. A standard 1/30-sec video exposure interval was used to acquire the images after the camera had reached thermal equilibrium at an ambient temperature of 18° C. Variance was computed at each mean signal level for a 200- by 200-pixel subset of each image. The slope of the least squares linear fit, when inverted, yields an A-to-D gain estimate of 132 electrons/count. This value compares reasonably

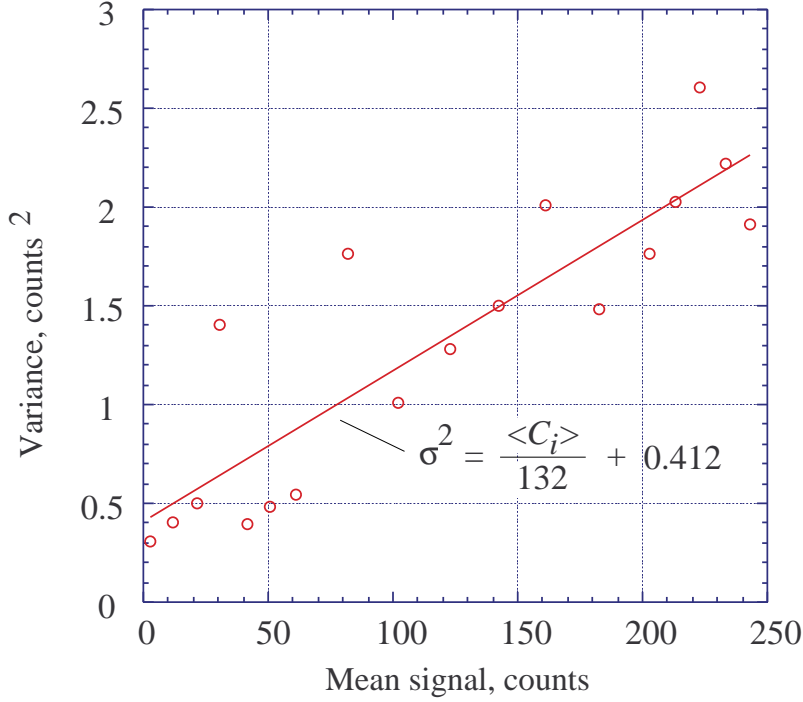


Figure 10. Measured total CCD radiometric variance for mean signal levels ranging from near zero to near saturation.

well with the estimate made above. Thus, an effective well depth, or dynamic range, of about 30,000 electrons can be expected, based on 8-bit digitization. The least-squares intercept can be equated with the constant term in the equation to yield a combined readout and dark-charge noise estimate of 85 electrons. This value is somewhat less than 114 electrons, the result from the previous individual estimates of these quantities. Since a small error in slope produced by scatter of the data can produce a significant error in the least squares intercept, it is reasonable to expect a large uncertainty in this value. A conservative approach is to use the previous larger estimates.

The total radiometric uncertainty,  $\sigma_i$ , can now be evaluated using equation (10) and the individual noise component estimates from above. For the filtered and unfiltered cameras, respectively, it evaluates to 150 or 180 electrons. A check of the digital-truncation parameter, which evaluates to 38 electrons, shows that individual noise sources do, in fact, determine the uncertainty in this case rather than digital truncation.

### Doppler-Shift Uncertainty

Doppler-shift uncertainty is determined using a first-order Taylor series expansion (refs. 12 and 17) to propagate the

radiometric uncertainty into the Doppler-shift result. The method is given in references 10 and 13, and is only summarized here. The Doppler-shift uncertainty is given by

$$\sigma_{\Delta f_i} = \left[ \left( \frac{s_i}{r_i} \right)^2 \left\{ \frac{\sigma_{s_i}^2}{s_i^2} + \frac{\sigma_{r_i}^2}{r_i^2} \right\} \left( \frac{\partial f}{\partial n_i} \right)_{f_D}^2 + \left( \frac{S}{R} \right)^2 \left\{ \frac{\sigma_S^2}{S^2} + \frac{\sigma_R^2}{R^2} \right\} \left( \frac{\partial f}{\partial N} \right)_{f_0}^2 \right]^{1/2} \quad (12)$$

where

- $s_i$  = filtered camera signal in electrons
- $r_i$  = unfiltered camera signal in electrons
- $n_i$  = normalized value =  $s_i / r_i$
- $f_D$  = Doppler frequency in MHz
- $f_0$  = unshifted laser frequency in MHz
- $\Delta f_i$  = Doppler frequency shift in MHz
- $\sigma_{s_i}$  = radiometric noise of filtered camera in electrons
- $\sigma_{r_i}$  = radiometric noise of unfiltered camera in electrons

- $S$  = filtered diode signal (reference cell) in volts  
 $R$  = unfiltered diode signal (reference cell) in volts  
 $N$  = normalized reference-cell value =  $S/R$   
 $\sigma_S$  = standard deviation of the filtered diode signal  
 $\sigma_R$  = standard deviation of the unfiltered diode signal

and the subscript  $i$  denotes the  $i$ th pixel in the CCD array.

The solution of this equation is shown in figure 11, assuming that experimental conditions are properly selected to ensure that the well capacity of the unfiltered camera is filled to two-thirds and transmission through the iodine is about 50%. The predicted uncertainty is minimum where the slope of the response curve is maximum and nearly constant. The figure shows two such regions that correspond to the positive and negative slopes of the response curve. Measurement of Doppler shift should be possible to over a range of about 340 MHz in each of these regions with an uncertainty not greater than about 7 MHz due to random effects. The corresponding velocity uncertainty,  $\pm 5$  m/s over a range of 230 m/s, is computed using equation (2), assuming a  $45^\circ$  viewing angle ( $\beta = 135^\circ$  for the worst case).

### Orthogonal-Component Uncertainty

The three measured velocity components do not form a mutually orthogonal set of vectors for a typical measurement application, nor do they align with the directions of the typical wind tunnel coordinate system. The viewing geometry cannot be oriented to measure the orthogonal components directly because limited optical access usually restricts the viewing geometry to only a few possible configurations. Also, the laser sheet orientation is usually fixed by the measurement requirements of the particular test being conducted (perpendicular to the free-stream flow, for example), and the geometry is further constrained by the requirement to avoid viewing angles steeper than  $45^\circ$ , measured between the viewing direction and the sheet, to minimize perspective distortion. Taken together, these constraints preclude the direct measurement of orthogonal components.

A geometric conversion is necessary to convert the direct measurements to orthogonal components, using equations (6), (7), and (8). Additional uncertainty is introduced in this conversion (ref. 18) when uncertainty propagates from the direct measurements to the computed orthogonal components through the data reduction equations. A Taylor series expansion with only linear terms retained is used to approximate how the uncertainty propagates to the results. In general, the geometric

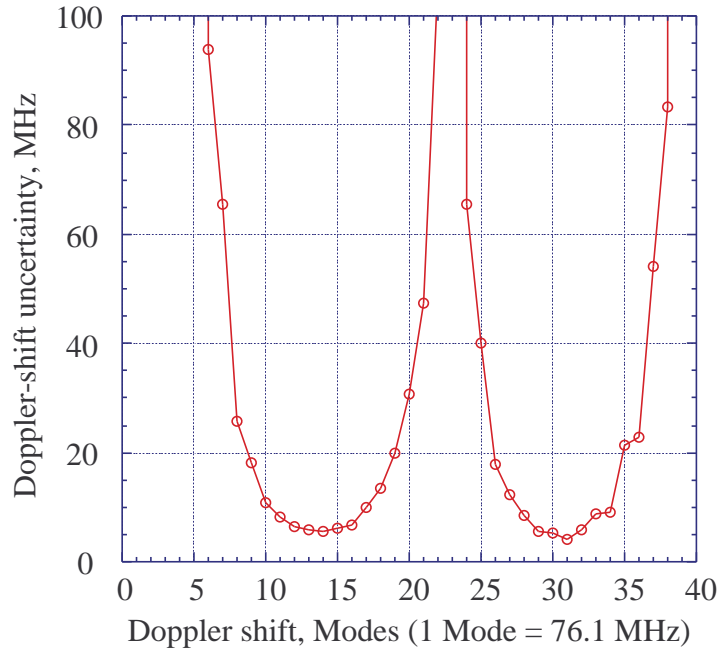


Figure 11. Uncertainty of the measured Doppler shift due to random effects. Signal strength of the unfiltered camera is assumed to be sufficient to fill the pixel wells to two-thirds capacity, and the laser frequency is assumed to be set midway between maximum and minimum absorption.

transformation equations are functions of many variables which can be expressed in the form

$$r = r(X_1, X_2, \dots, X_J) \quad (13)$$

Provided the variables are statistically independent, the standard deviation of the result can be expressed as (ref. 19)

$$\sigma_r^2 = \sum_{i=1}^J \frac{\partial r}{\partial X_i} \sigma_i^2 \quad (14)$$

where  $\sigma_i$  represents the random component of uncertainty of each variable. The uncertainty component due to bias can be computed in a similar manner using the expression

$$B_r^2 = \sum_{i=1}^J \frac{\partial r}{\partial X_i} B_i^2 \quad (15)$$

The bias and random uncertainty components are then combined using equation (9) to yield total uncertainty of the orthogonal components.

Using equation (14), the  $U$ -,  $V$ -, and  $W$ -component variances are expressed as

$$\begin{aligned} \sigma_U^2 = & \frac{\partial U}{\partial U_{ma}} \sigma_a^2 + \frac{\partial U}{\partial U_{mb}} \sigma_b^2 + \frac{\partial U}{\partial U_{mc}} \sigma_c^2 + \frac{\partial U}{\partial X_1} \sigma_{X_1}^2 \\ & + \frac{\partial U}{\partial Y_1} \sigma_{Y_1}^2 + \frac{\partial U}{\partial Z_1} \sigma_{Z_1}^2 + \frac{\partial U}{\partial X_2} \sigma_{X_2}^2 + \frac{\partial U}{\partial Y_2} \sigma_{Y_2}^2 \\ & + \frac{\partial U}{\partial Z_2} \sigma_{Z_2}^2 + \frac{\partial U}{\partial X_3} \sigma_{X_3}^2 + \frac{\partial U}{\partial Y_3} \sigma_{Y_3}^2 + \frac{\partial U}{\partial Z_3} \sigma_{Z_3}^2 \end{aligned} \quad (16)$$

$$\begin{aligned} \sigma_V^2 = & \frac{\partial V}{\partial U_{ma}} \sigma_a^2 + \frac{\partial V}{\partial U_{mb}} \sigma_b^2 + \frac{\partial V}{\partial U_{mc}} \sigma_c^2 + \frac{\partial V}{\partial X_1} \sigma_{X_1}^2 \\ & + \frac{\partial V}{\partial Y_1} \sigma_{Y_1}^2 + \frac{\partial V}{\partial Z_1} \sigma_{Z_1}^2 + \frac{\partial V}{\partial X_2} \sigma_{X_2}^2 + \frac{\partial V}{\partial Y_2} \sigma_{Y_2}^2 \\ & + \frac{\partial V}{\partial Z_2} \sigma_{Z_2}^2 + \frac{\partial V}{\partial X_3} \sigma_{X_3}^2 + \frac{\partial V}{\partial Y_3} \sigma_{Y_3}^2 + \frac{\partial V}{\partial Z_3} \sigma_{Z_3}^2 \end{aligned} \quad (17)$$

$$\begin{aligned} \sigma_W^2 = & \frac{\partial W}{\partial U_{ma}} \sigma_a^2 + \frac{\partial W}{\partial U_{mb}} \sigma_b^2 + \frac{\partial W}{\partial U_{mc}} \sigma_c^2 + \frac{\partial W}{\partial X_1} \sigma_{X_1}^2 \\ & + \frac{\partial W}{\partial Y_1} \sigma_{Y_1}^2 + \frac{\partial W}{\partial Z_1} \sigma_{Z_1}^2 + \frac{\partial W}{\partial X_2} \sigma_{X_2}^2 + \frac{\partial W}{\partial Y_2} \sigma_{Y_2}^2 \\ & + \frac{\partial W}{\partial Z_2} \sigma_{Z_2}^2 + \frac{\partial W}{\partial X_3} \sigma_{X_3}^2 + \frac{\partial W}{\partial Y_3} \sigma_{Y_3}^2 + \frac{\partial W}{\partial Z_3} \sigma_{Z_3}^2 \end{aligned} \quad (18)$$

where

- $\sigma_U$  = computed  $U$ -component standard deviation
- $\sigma_V$  = computed  $V$ -component standard deviation
- $\sigma_W$  = computed  $W$ -component standard deviation
- $\sigma_a$  = directly measured  $a$ -component standard deviation, calculated to be  $\pm 5$  m/s for a single image
- $\sigma_b$  = directly measured  $b$ -component standard deviation, calculated to be  $\pm 5$  m/s for a single image
- $\sigma_c$  = directly measured  $c$ -component standard deviation, calculated to be  $\pm 5$  m/s for a single image
- $\sigma_{x_1}, \sigma_{y_1}, \sigma_{z_1}$  = standard deviations of unit vector components defining the  $a$ -component direction
- $\sigma_{x_2}, \sigma_{y_2}, \sigma_{z_2}$  = standard deviations of unit vector components defining the  $b$ -component direction
- $\sigma_{x_3}, \sigma_{y_3}, \sigma_{z_3}$  = standard deviations of unit vector components defining the  $c$ -component direction

The partial derivatives are obtained from equations (6), (7), and (8), and standard deviations of the directly measured components have been estimated to be  $\pm 5$  m/s. Unknown are the standard deviations of the unit vector components that define the directions of the measured velocities. These are determined as follows.

The unit vectors are computed from measurements of the viewing geometry, using equations that have the same form as equation (13). To determine the uncertainty of these vectors, uncertainty propagation is again employed using equation (14). The individual geometric measurement uncertainties, or standard deviations, are required as input, in addition to another set of partial derivatives. The standard deviations are approximately equal to estimates of absolute uncertainty obtained in the following way. When the geometry is measured, the absolute uncertainty of each measured parameter is estimated so that, if the measurement were repeated 100 times, about 68 of the values would not deviate from the mean by an amount greater than plus or minus the estimated absolute uncertainty.

Figure 12 shows a general measurement geometry setup and coordinate system in a wind tunnel test section. The unit vectors for each of the three camera locations are given in Appendix A. These expressions are quite complex when faced with the task of acquiring the partial derivatives, as are equations (6), (7), and (8). Fortunately, the derivatives can be easily obtained in algebraic form using a symbolic mathematics program on a personal computer (see Appendix B).

Specific values of orthogonal-component uncertainty are test dependent. A typical example is presented here using the geometry of figure 12. Assume, for the purpose of this example, a 7- by 10-ft test section and a free-stream velocity of 60 m/s. Assume that the cameras are located at  $\pm 45^\circ$  to the plane of the laser sheet, measured in the x-y plane, and that camera 3 and the sheet origin are located in the horizontal plane through the vertical center of the test section. Assume further that cameras 1 and 2 are located at  $\pm 45^\circ$  from this plane, measured in the y-z plane, and that all coordinates can be measured with a precision of  $\pm 1/8$  in. with 68% confidence (a total precision-uncertainty interval of  $1/2$  in. at 95% confidence). The unit vectors for this geometry are

$$0.628 \hat{i} - 0.460 \hat{j} + 0.628 \hat{k}$$

$$0.628 \hat{i} - 0.460 \hat{j} - 0.628 \hat{k}$$

$$-0.924 \hat{i} - 0.383 \hat{j} - 0.000 \hat{k}$$

for camera locations 1, 2, and 3, respectively.

Using equations (16), (17), and (18), the  $U$ ,  $V$ , and  $W$  precision uncertainties evaluate to  $\pm 4$ ,  $\pm 7$ , and  $\pm 6$  m/s, respectively, for a single image at 68% confidence, and the values are doubled for 95% confidence. For 100-image averages, the precision uncertainties evaluate to  $\pm 0.4$ ,  $\pm 0.7$ , and  $\pm 0.6$  m/s, respectively, at 68% confidence. Again, these values are doubled for 95% confidence.

Optical access constraints may preclude the use of  $45^\circ$  viewing angles as in this example. For other geometries with small vector separations, larger uncertainties can be expected. In the sections that follow, sample measurements are presented with estimates of precision uncertainty using this method.

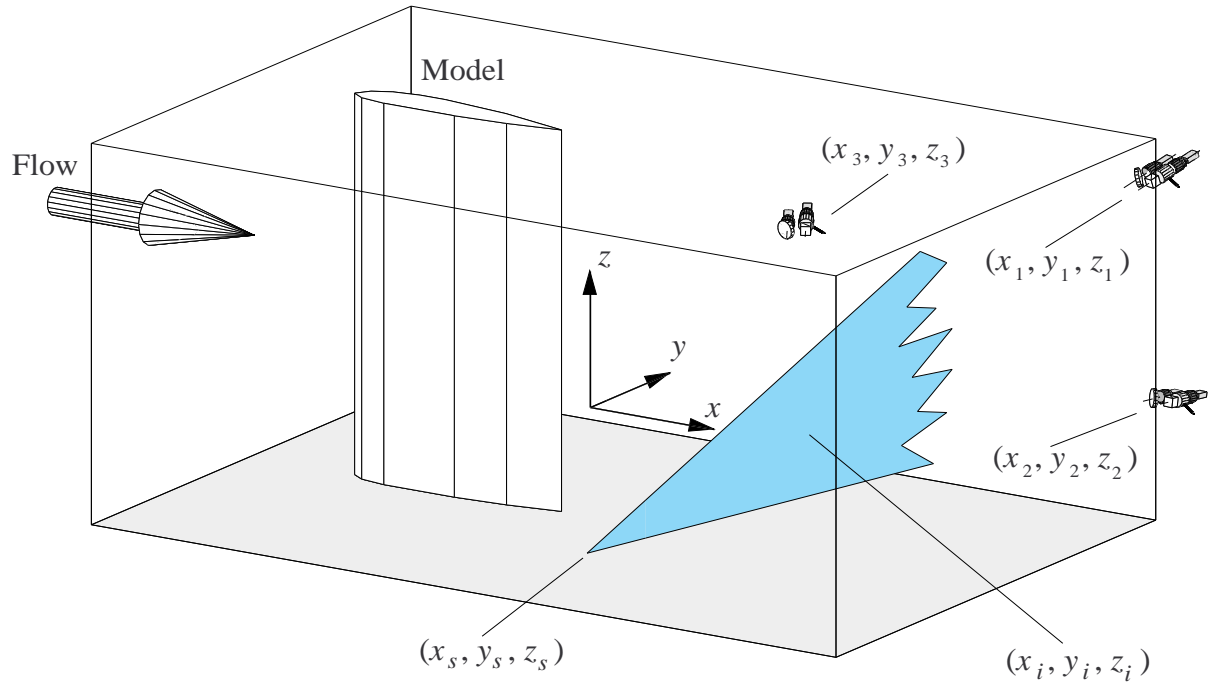


Figure 12. Coordinate system and measurement geometry used to develop the expressions that define the unit vector directions of the measured components.



## Experimental Results

### Background

DGV system development at Ames Research Center began in the summer of 1991. A single component system was first assembled and tested in the laboratory environment. Additional hardware was then added to expand the system capability to measurement of three components. As the development progressed, successful laboratory measurements of a high-speed rotating wheel were made using the full three-component system. In order to justify further development, a demonstration of the technique in the more demanding environment of a large wind tunnel was required.

Steps were taken to begin solving the problems associated with installing and operating a system of this type in a large wind tunnel environment before the system had reached a mature configuration. Laboratory development of the system continued in parallel, focusing on understanding and fine-tuning the calibration procedures that are necessary to yield accurate measurements. In the sections that follow, sample data are presented showing large wind tunnel measurements made with the system.

The data show a progression toward successful application of the technique as problems were solved in the laboratory and the system evolved.

### Jet Engine Simulator Exhaust-Plume Measurements

The DGV system was first used in September 1993 in the Ames 40- by 80-Foot Wind Tunnel to measure the mean velocity distribution of a jet simulator exhaust plume. The model, an isolated engine simulator, was tested to provide baseline data for further research in the area of propulsion/wing aerodynamic interaction. Subsequent testing of a 13.5%-scale semispan model would provide additional data on performance changes that occur when the engine simulator is installed on the wing. Exhaust velocity measurements for one jet simulator configuration constituted only a small part of the complete wind tunnel test. The measurements were made with the objective of identifying the problems that occur when the DGV technique is used in a large wind tunnel, as well as to provide data for the wind tunnel research program.

Figure 13 shows the isolated engine simulator mounted in the test section. The engine simulator was composed of an



*Figure 13. Isolated engine simulator shown in the Ames 40- by 80-Foot Wind Tunnel test section. The nozzle shown is a conical nozzle and not the mixer-ejector described in the text.*

upstream air and propane delivery system and an interchangeable exhaust nozzle. The upstream delivery system metered high-pressure air and propane to a choke plate and burner-can assembly for hot-flow testing. Several nozzles were tested during the course of the test, but velocity measurements were taken in the exhaust flow of only one nozzle, a first-generation mixer-ejector nozzle.

A diagram of the wind tunnel test section showing the camera system locations and the orientation of the laser sheet is shown in figure 14. The camera systems were mounted outside the wind tunnel shell and viewed the flow through the test section viewports. Because of the limited number of test section viewports, only a few viewing geometry configurations were possible. The geometry configuration was limited further by the requirement to measure the exhaust velocity profile only one-half diameter from the nozzle exit. To prevent partial blocking of the image by the nozzle, viewing locations on the downstream side of the laser sheet were required, as shown in the figure.

The jet simulator flow was seeded by spraying 1010 turbine engine fuel-system preservative oil into the ejector intake passages. A spray bar manifold, composed of 1/4-in. tubing, delivered the oil spray to the ejector intakes through 0.0135-in. diameter holes drilled in the tubing. The spray bar was attached to the outside surface around the circumference of the engine simulator. Oil flow was metered at a flow rate of about 1 gpm from a pressurized reservoir located in the wind tunnel balance house using a manual gate valve.

The jet simulator flow was seeded only during the period of actual image acquisition in what could be termed a *pulse* mode of operation to minimize the amount of oil injected into the wind tunnel. Sequences of 10 images were acquired from all cameras at each test condition. A seed pulse of about 3 to 5 sec was required for each set of images in the sequence. Thus, cumulative seeder operation at each test condition was not more than about 1 min.

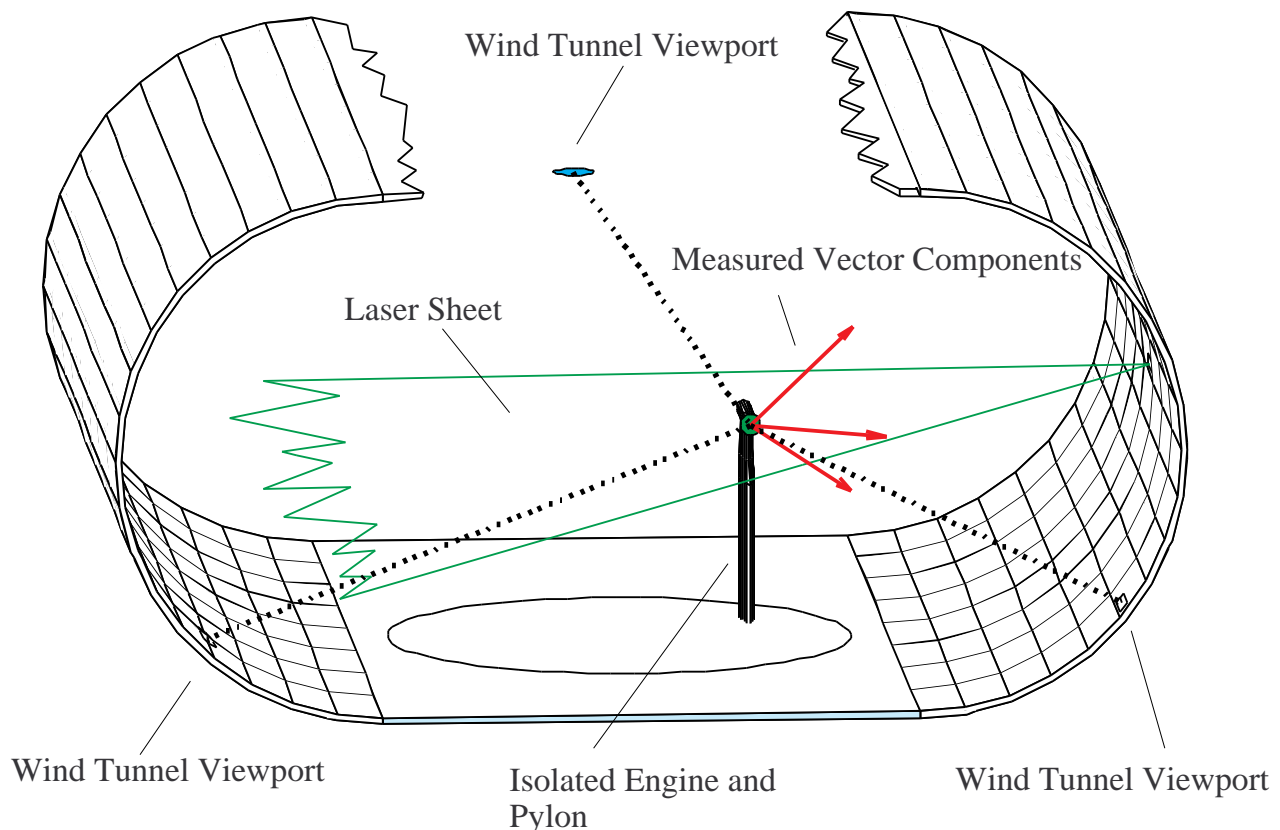
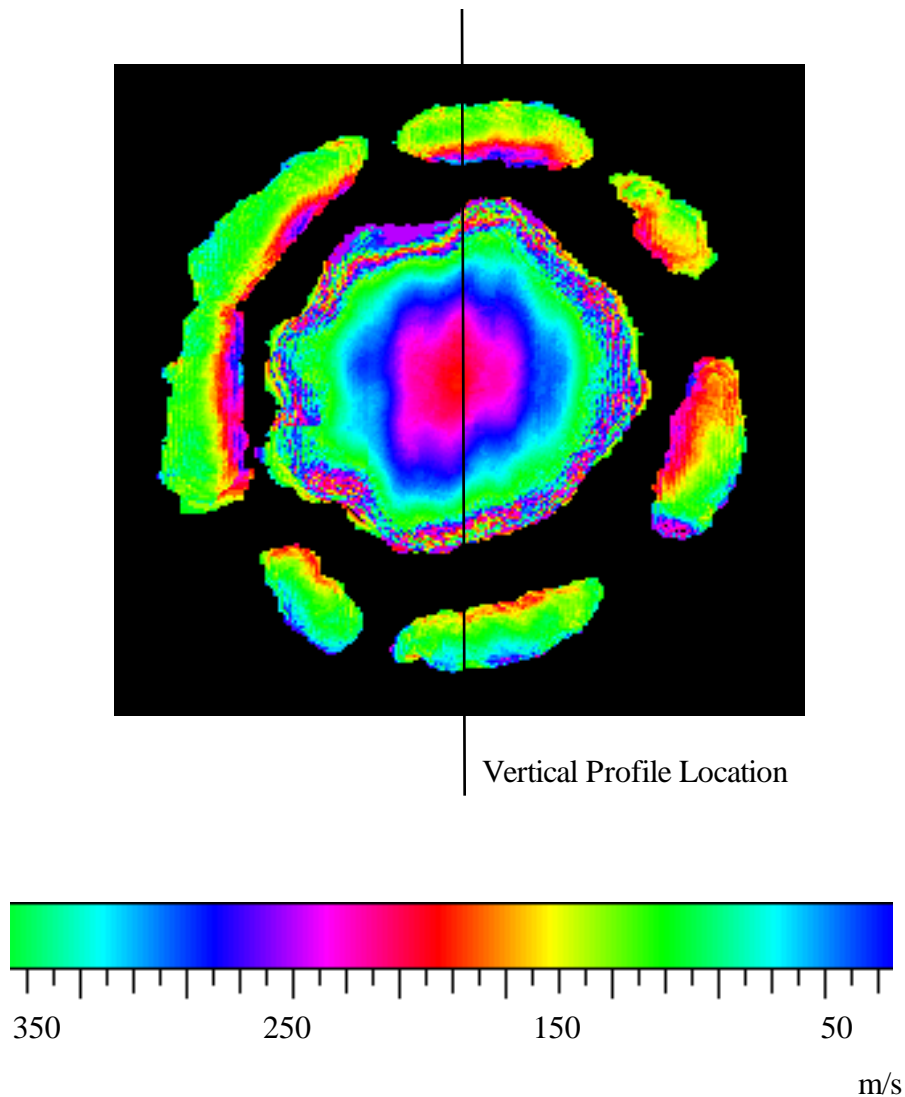


Figure 14. Diagram of the test section showing the camera locations, laser sheet, and the directions of the measured components (view is shown looking upstream).

Images were acquired at four different free-stream Mach numbers and three different nozzle pressure ratios (NPR). Unfortunately, two problems adversely affected data quality and precluded final conversion to orthogonal components. First, the scattered light intensity was insufficient at the camera system located in the ceiling of the test section. The full 8-watt laser power produced only dim images of the seeded region at this side-scatter angle. Second, drift of the iodine response curves added bias to the velocity data. Response curves were obtained in the laboratory, at this early stage of development, instead of immediately prior to acquiring data images. The bias

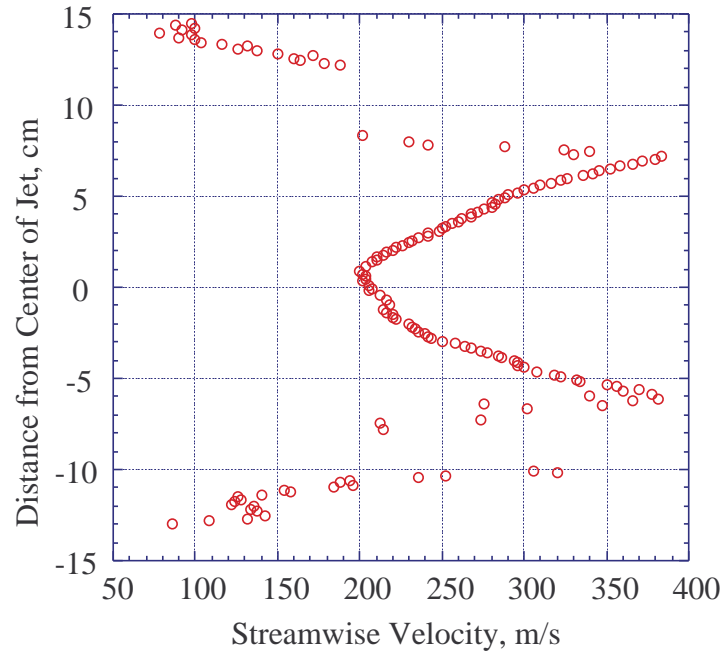
occurred when cell temperatures could not be duplicated with sufficient repeatability in the wind tunnel environment to reproduce the response curves that had been measured in the laboratory. Insulated iodine-cell enclosures were later developed and installed to improve thermal stability of the cells. Nevertheless, response curves should be determined in situ prior to acquiring data images to minimize this type of bias.

Figure 15 shows sample data acquired by the camera system located in forward scatter (J. F. Meyers of Langley Research Center assisted in acquiring and processing these data). Images obtained at this location



(a) Mean axial velocity image.

Figure 15. Measured mean axial component of the jet simulator exhaust plume.



(b) Vertical profile through the center of the velocity image.

Figure 15. Concluded.

yielded a measured component inclined  $24.0^\circ$  from the free-stream flow. The velocity image is computed from a sequence of 10 individual images that were taken at an NPR of 3.4, a free-stream Mach number of 0.244, and an exhaust flow total temperature of  $1860^\circ\text{R}$ . Fringes that are oriented vertically are faintly visible in the core of the plume superimposed on the velocity data. These can be attributed to a reflection from the back surface of the thin plate beamsplitters used in this early optical configuration. Also apparent is the wavy appearance of the plume edge, which may be a manifestation of the Widnall-Sullivan instability (ref. 20). Localized areas of seeded flow around the periphery of the exhaust plume are evident, in addition to the plume itself. These areas were created when a portion of the 1010 oil spray, entrained by the free-stream flow, passed around the outside of the hot nozzle rather than entering the ejector. Notice that the velocity in these regions approaches the free-stream value of 83 m/s. A vertical profile through the center of the plume is shown, in addition to the velocity image, to aid in interpreting the quantitative, color-coded image data. The blue portion of the palette repeats, but continuity of the profile resolves the ambiguity.

A total and static pressure rake designed for transonic velocities was traversed through the exhaust plume to acquire data that could be compared with the velocity image data. Figure 16 shows the comparison of profiles through the center of the plume for the same conditions as those of figure 15. Clearly evident is the large bias error that resulted when the response curve drifted between the time of cell calibration and acquisition of images. The general curve shape is reproduced well, however.

The precision uncertainty interval is estimated to be  $\pm(5/\sqrt{10})2=\pm3\text{ m/s}$  for the 10-image average with 95% confidence, except at the periphery of the jet. Seed density drops off significantly there, as the plume mixes with the unseeded free-stream air. The unfiltered camera pixels are no longer filled to two-thirds their well capacity and precision errors increase. In fact, as the seed density approaches zero, differences between the filtered and unfiltered images become insignificant because of the lack of Doppler-shifted light. Consequently, one would expect the corresponding normalized value to approach zero velocity, as it does in figure 16.

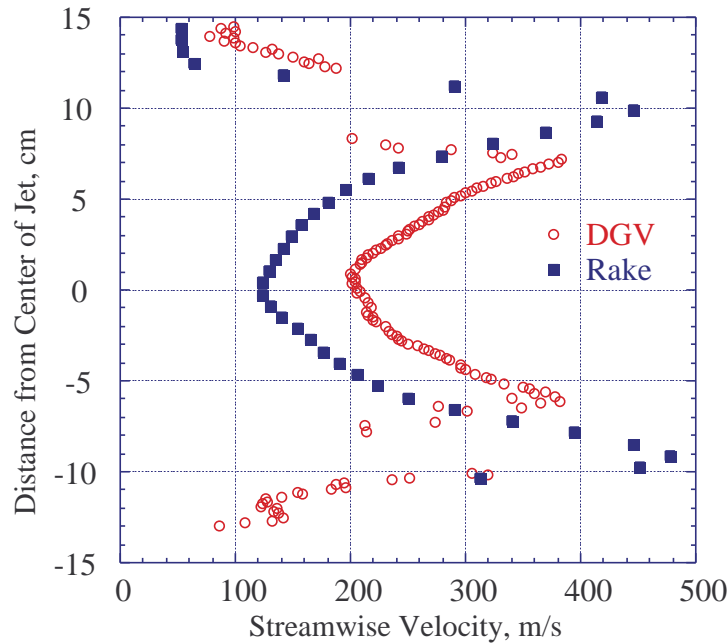


Figure 16. Comparison between DGV and rake velocity measurements through the center of the exhaust plume.

### Advanced Fighter LEX-Vortex Measurements

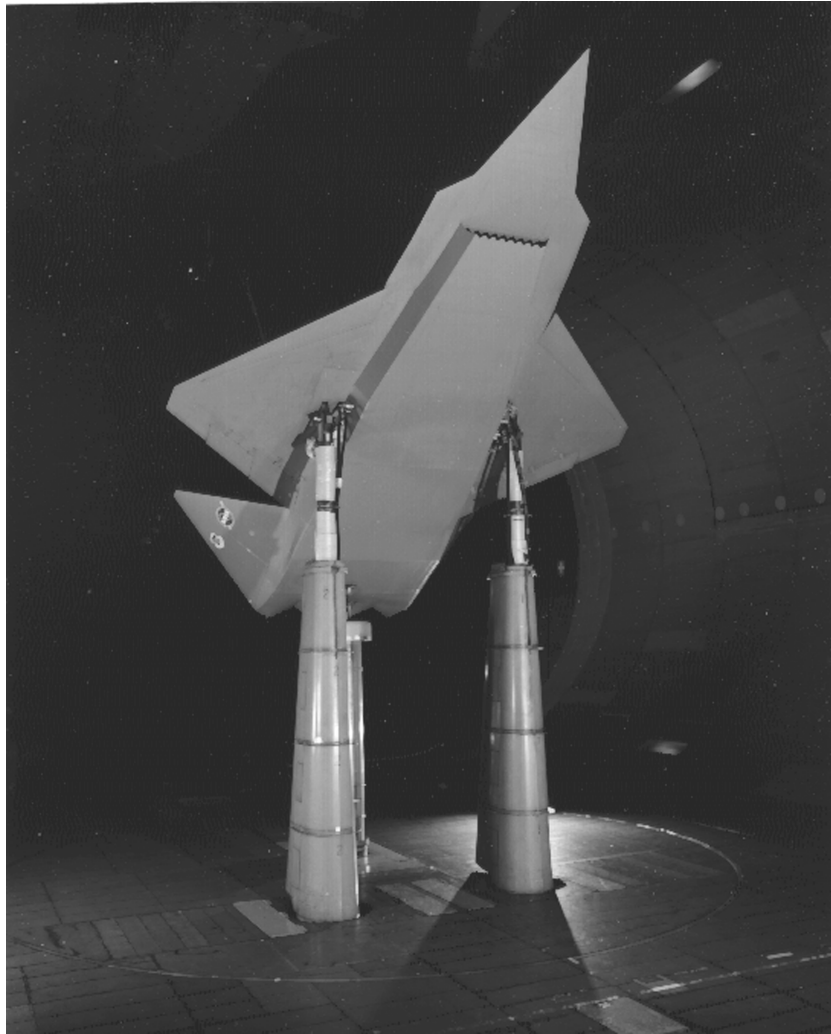
The DGV system was used a second time, in December 1994, in the Ames 40- by 80-Foot Wind Tunnel. Measurements were made above the wing of a generic fighter model to determine the distribution of velocities in the leading-edge-extension vortex. The model, a 55%-scale multi-role fighter, was tested with the objective of determining its high-lift and control characteristics (ref. 21). The low-observable configuration had a chined forebody and was equipped with leading-edge extensions (LEX), deflectable leading- and trailing-edge flaps, twin vee-tails, and a flow-through inlet. Figure 17 shows installation photographs of the model in the wind tunnel. Also depicted is a visualization of the LEX vortex, showing where DGV measurements were made. The reason for including DGV measurements as part of this test was again to continue identifying problems and making the refinements necessary to develop the technique for large wind tunnel applications.

A diagram of the wind tunnel test section showing the camera system locations and the orientation of the laser sheet is shown in figure 18. The forward-scatter viewing angle of the previous geometry could not be used again because the view of the object plane was blocked by the model from this direction. The only suitable alternative location that provided an unobstructed view was in the ceiling of the test section at the upstream end. Unfortunately, this change produced measured vectors that lacked

sufficient separation in the vertical direction—the vectors measured by the two ceiling camera systems were nearly redundant with respect to the vertical component, and the third vector, measured by the side-wall camera system, was nearly horizontal with essentially no vertical component. An increase in the random uncertainty of the computed orthogonal velocity component,  $W$ , resulted because of uncertainty propagation.

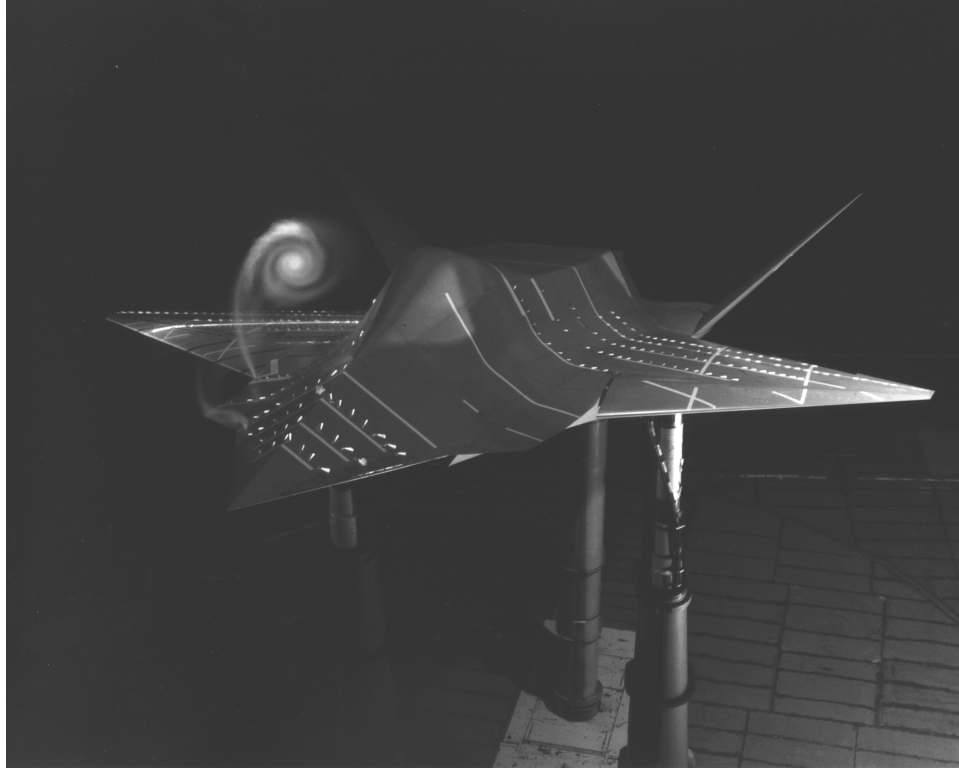
Seeding for the LEX vortex flow was created using a vapor condensation smoke generator. This type of generator produces smoke by heating a fogging fluid, composed primarily of propylene glycol, until vapor is formed. The vapor is forced through an orifice and immediately expands to form a polydisperse suspension of droplets. Most of the droplets that are created have diameters close to about 1 micron, and only about 5% are larger than 5 microns (ref. 22). Seed was released from the forward end of the LEX leading edge near the forebody juncture at a rate of about 1.5 gph during data acquisition.

Sample mean orthogonal-velocity results are shown in figure 19 for an angle of attack of  $16^\circ$  and a free-stream velocity of 30 m/s. The images present a view from behind the model looking into the free-stream flow. Optical distortions have been removed and the object plane has been rotated to a perpendicular view. The spanwise velocity component,  $V$ , is positive to the right, and downwash component,  $W$ , is positive up. Sequences of 10 frames were averaged together to create the images.



*(a) General installation showing high-alpha condition.*

*Figure 17. Generic advanced fighter model shown in the Ames 40- by 80-Foot Wind Tunnel test section.*



(b) Flow visualization showing DGV measurement location.

Figure 17. Concluded.

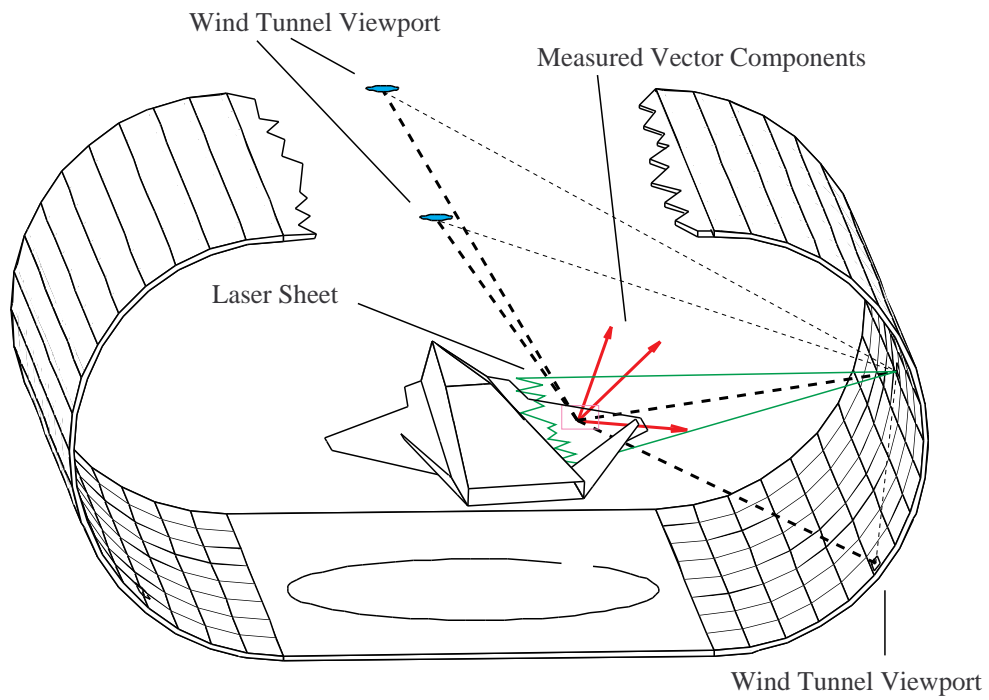


Figure 18. Diagram of the test section showing the camera locations, laser sheet, and the directions of the measured components (view is shown looking upstream).



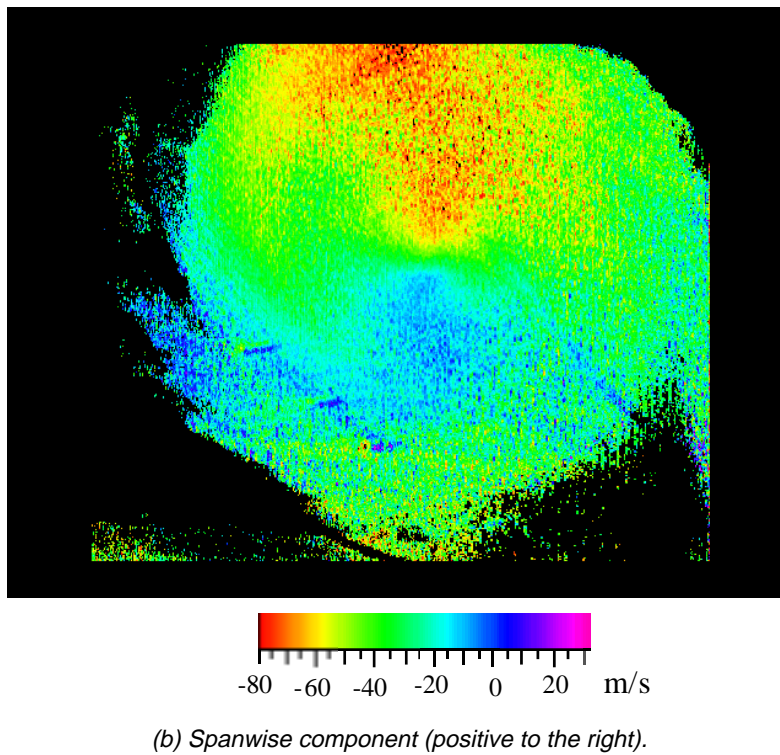
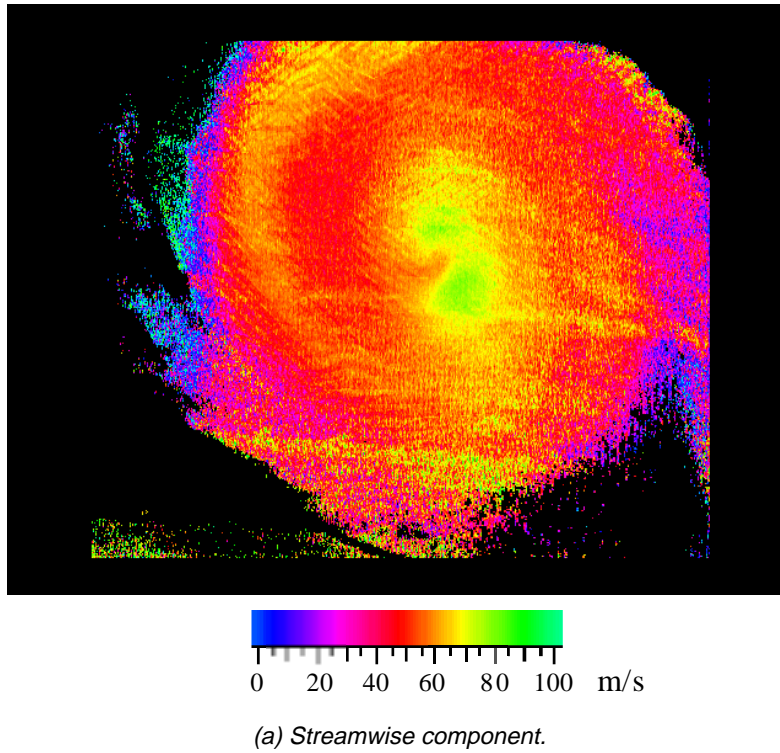
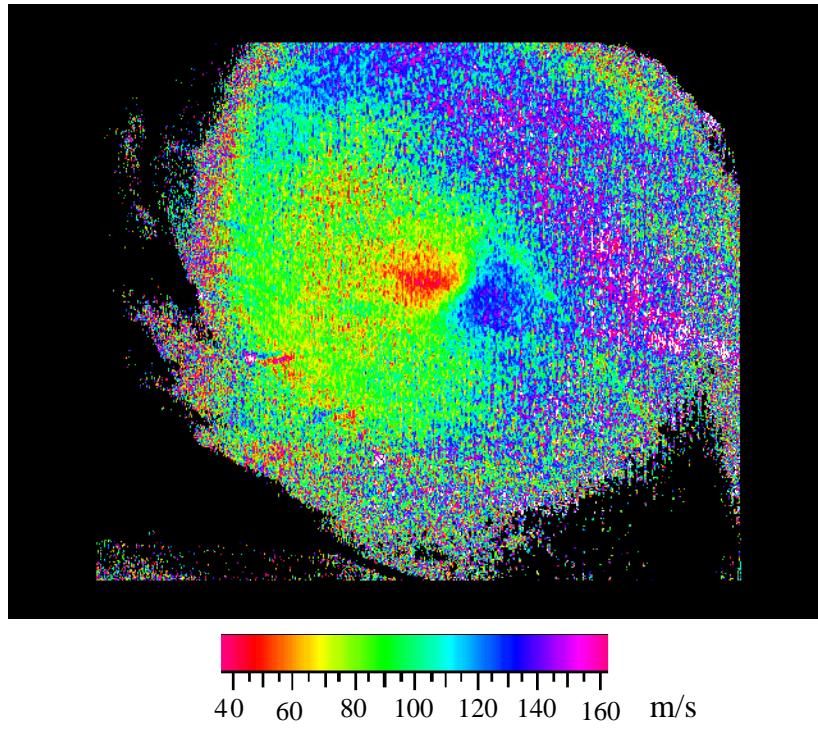
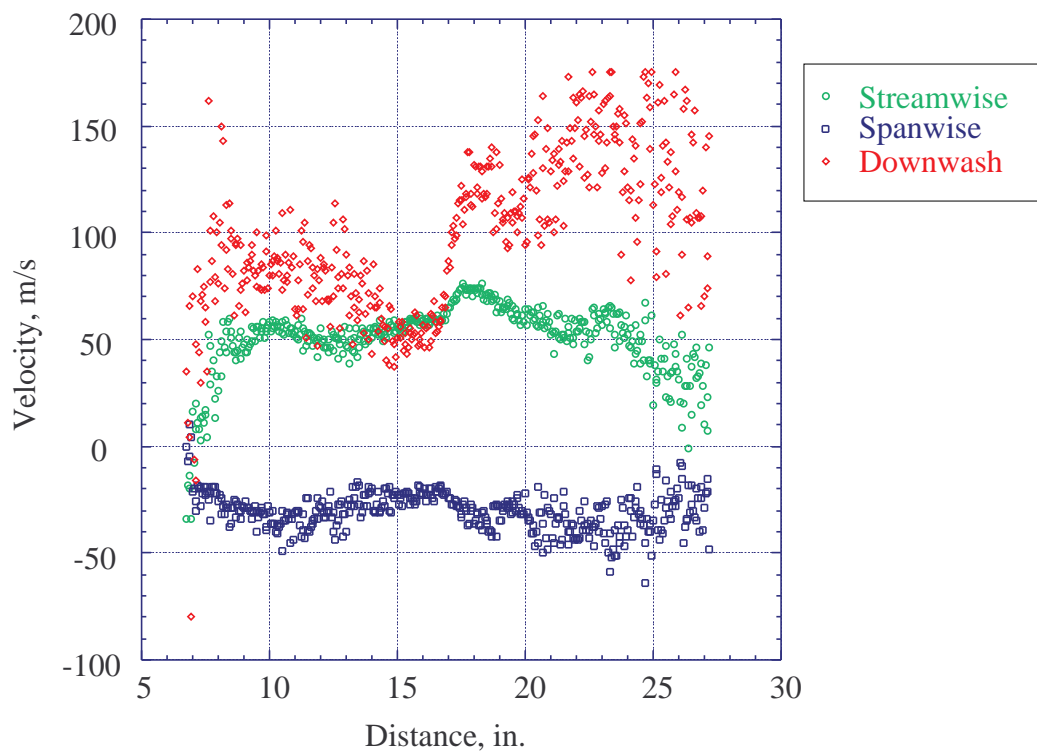


Figure 19. Measured mean orthogonal components of LEX flow field (looking upstream).



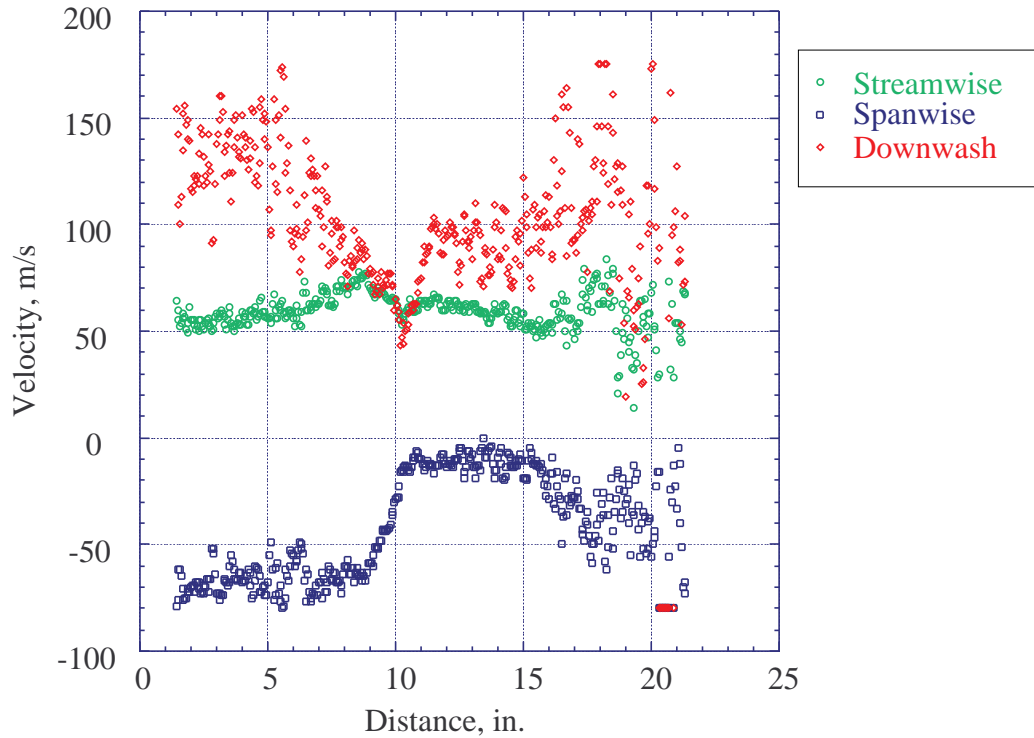


(c) Downwash component (positive up).



(d) Horizontal profile through the center of the vortex.

Figure 19. Continued.



(e) Vertical profile through the center of the vortex.

Figure 19. Concluded.

The velocity bias, observed in the results of the previous test, is also present in these measurements. Although no independent comparison measurements were made to support this assertion, it is clear that the measured streamwise component is too large when compared to the free-stream velocity. Also clearly biased are the crossflow velocities, which should be much closer to zero at the center of the vortex. The bias, due again to response curve drift, reoccurred because its source had not yet been fully identified prior to this test. Because of limited resources, software development and wind tunnel installation preparations were performed in parallel with the effort to resolve bias. The problem was not identified until later, and no significant change in the calibration procedure was made prior to acquiring these data. Nevertheless, three components of velocity were measured and successfully converted to orthogonal components, and the images, although biased in the absolute sense, still provide quantitative information about the relative change of

mean velocity throughout the measurement area. For example, a small region is shown at the center of the vortex where the streamwise component increases by about 20 m/s above the free-stream value. Also shown is a rotational velocity change of about 60 m/s from one side of the vortex to the other.

The relatively large random uncertainty of the downwash component is shown by the speckled appearance of the velocity image and the scatter of the plotted velocities. Equations (16), (17), and (18) are used to compute uncertainty estimates for the measurement geometry. For the 10-image averages, the streamwise, spanwise, and downwash precision uncertainty intervals are estimated to be  $\pm 4$ ,  $\pm 4$ , and  $\pm 10$  m/s, respectively, with 95% confidence. These values correlate well with the scatter of the plotted velocities except at the edges of the images where the decreased seed density results in increased random uncertainty, as described earlier.

### Wing Tip-Vortex Measurements

The DGV system was used a third time, in March 1996, in the Ames 7- by 10-Foot Wind Tunnel. Logistical problems, which were quite significant in the large test section during the previous tests, were manageable in this smaller facility and attention could be focused on solving other problems. The model, a 3%-scale commercial supersonic transport configuration, was tested to evaluate the yaw control effectiveness of a particular pneumatic forebody flow control device at high angles of attack (ref. 23). Figure 20 shows an installation photograph of the model in the test section. The configuration, a cranked delta planform, simulated approach and landing with leading-edge flaps that were drooped to  $30^\circ$  and trailing-edge flaps that were deflected to  $10^\circ$ . DGV measurements were again included to continue development of the technique in the actual wind tunnel environment.

The diagram of figure 21 shows an isometric view of the test section and measurement geometry. Relatively large, high-quality test section windows provided excellent optical access. To improve image intensity and minimize

the random uncertainty of the  $W$  component, forward scatter viewing angles were selected with large camera separation in the vertical direction. The laser sheet was located 50 in. downstream of the main wing trailing edge, and camera angles were adjusted to view the tip vortex and wake of the right wing. DGV measurements were made at a free-stream dynamic pressure of 30 psf over an angle of attack range that varied between  $10^\circ$  and  $20^\circ$ .

The flow was seeded using a vapor condensation smoke generator, which was located upstream of the model in the low-speed flow of the settling chamber. Its position was initially varied, using trial and error, to determine the location that produced the most uniform coverage of the measurement area. Since seed was released from a single source at the generator, uniform coverage was difficult to attain. Most of the seed was pulled into the tip vortex, leaving some of the other areas virtually unseeded. Fortunately, after about 8 to 10 min of running, seed also accumulated in the wind tunnel circuit and the uniformity improved significantly. The fogging fluid, a mixture composed primarily of propylene glycol, was injected at a rate of about 0.5 gph.



Figure 20. High-Speed Civil Transport model shown in the Ames 7- by 10-Foot Wind Tunnel test section.

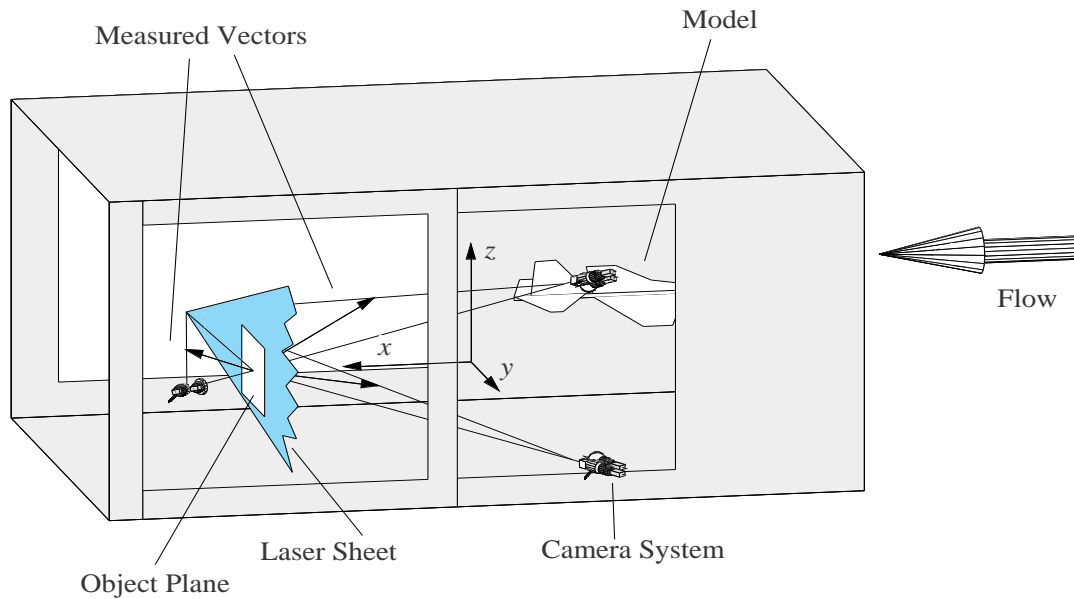


Figure 21. Test section diagram showing the camera locations, laser sheet, and the directions of the measured components.

Sample results are shown in figure 22 for an angle of attack of  $18^\circ$  and a free-stream velocity of 48 m/s. The velocities have been converted to orthogonal components and represent an average of 10 frames. The view is from upstream looking in the direction of the free-stream flow, and the object plane has been rotated to simulate a perpendicular view. The coordinate system origin was located at the horizontal center of the test section where the model was attached to the support strut at the pitch-axis pivot point. Thus, the abscissa of each image measures distance from the center of the tunnel, in a spanwise direction, outboard along the right wing. The spanwise component,  $V$ , is positive to the left, and the downwash component,  $W$ , is positive up. A velocity color map with discrete 5-m/s steps was chosen to better visualize the small changes of the streamwise component. The other images, which contain larger changes in velocity, are colored using a rainbow map.

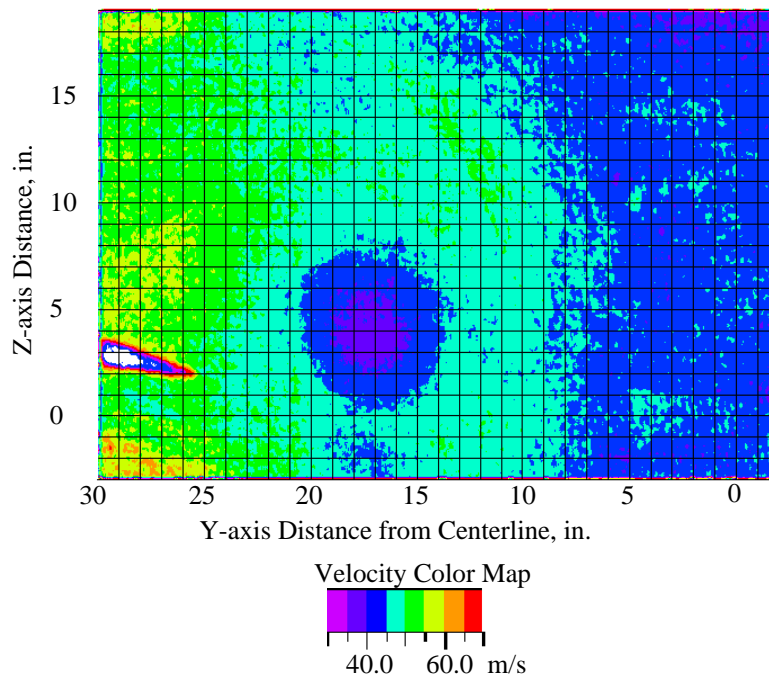
The previous response-curve drift and resulting bias were successfully avoided in this case by measuring the response curves in situ immediately prior to acquiring data. The images show the correct streamwise velocity and near zero crossflow velocity at the center of the vortex. Notice the blue-green contour in the free-stream portion of the streamwise image. This color transition represents a velocity of 50 m/s, essentially the free-stream velocity contour. At the vortex center, the crossflow images are shaded green. This shade corresponds to 0 m/s on the rainbow map. Also clearly visible is slower streamwise flow at the center of the vortex, in

figure 22(a), and the rotational flow, in figures 22(b) and 22(c), shown by the color transition from red through yellow, green, and blue.

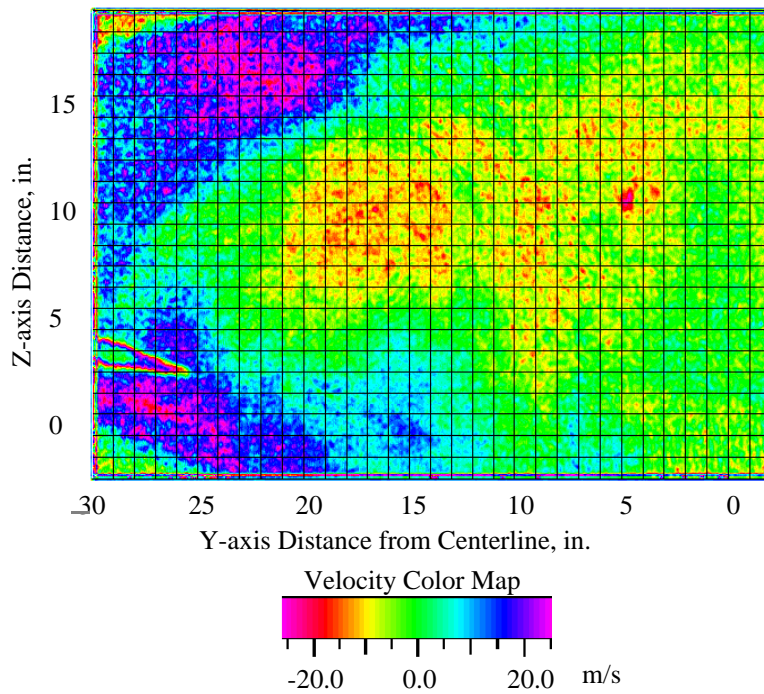
The small projection on the left-hand side of the streamwise- and spanwise-component images is an image of the model tail-cone tip. This part of the model entered the image of the downstream camera system at the higher angles of attack. It remained after subtraction of the background images because these images were acquired only at an angle of  $0^\circ$  and not at the higher angles. It would have been properly subtracted had separate background images been acquired at each angle.

It is interesting to note that the tail cone is not significantly visible in the downwash-component image. For this geometry, the image acquired at downstream camera location does not significantly influence the computation of this component. This image measures a vector that is almost horizontal. Hence, the vector is orthogonal to the downwash component, and its contribution in the transformation is negligible. The tail cone artifact is, therefore, not transferred to the downwash image.

The upper and lower left-hand corners of the images show areas of the flow where the free-stream seed accumulation did not produce sufficient droplet number density. These areas are most obvious in the spanwise-component image, which is computed primarily from the downstream camera-system measurement. Apparently, this location may have been at an angle for which Mie scattering intensity was less than the other two.



(a) Streamwise component.



(b) Spanwise component (positive to the left).

Figure 22. Measured mean orthogonal components of the High-Speed Civil Transport wake flow field (looking downstream).



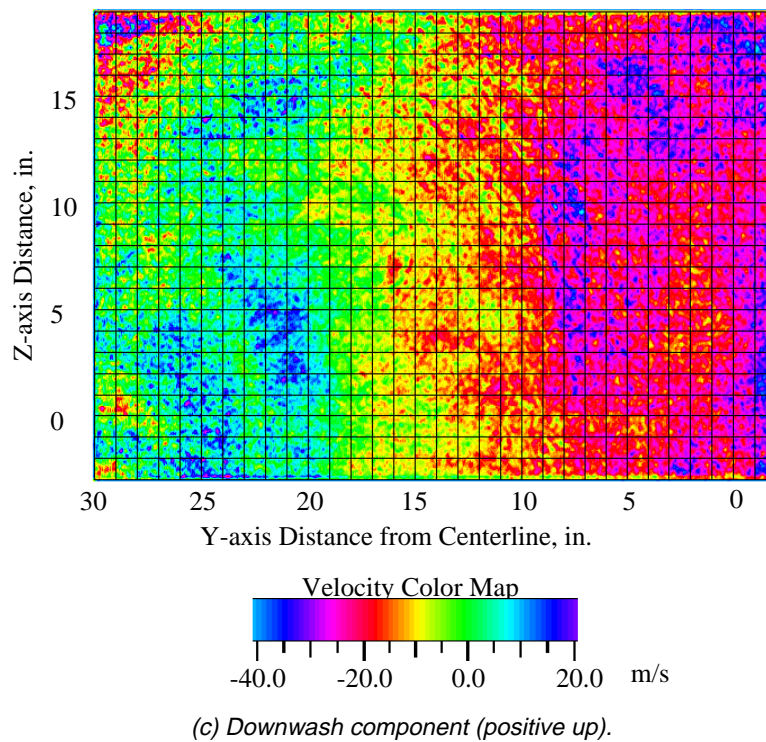


Figure 22. Concluded.

The speckled appearance of these images provides a qualitative indication of the random uncertainty. Equations (16), (17) and (18) are again used to compute quantitative estimates for this measurement geometry. The streamwise, spanwise, and downwash precision uncertainty intervals are estimated to be  $\pm 2$ ,  $\pm 5$ , and  $\pm 7$  m/s, respectively, for the 10-image averages with 95% confidence. These values correlate well with the scatter of the plotted velocities except where the seed density is low for the reasons discussed earlier.

### Flap-Edge Vortex Measurements

The DGV system was used again, in July 1996, in the Ames 7- by 10-Foot Wind Tunnel to measure the mean velocity distribution in the wake region downstream of an unswept wing equipped with a half-span Fowler flap. The test was undertaken to study the three-dimensional flow field of the midspan discontinuity (ref. 24). Tip effects were removed from the flow field by mounting the wing vertically in the test section between two false walls. Figure 23 shows an installation photograph of the wing, a NACA 63<sub>2</sub>-215 Mod B airfoil and 0.3 chord, half-span flap.



Figure 23. NACA 63<sub>2</sub>-215 Mod B airfoil and 0.3 chord, half-span flap shown in the Ames 7- by 10-Foot Wind Tunnel test section.

The diagram of figure 24 shows an isometric view of the test section and measurement geometry. This geometry is essentially the same as the geometry of the March test, except that the upstream and downstream camera system locations have been interchanged. By making this change, a small increase in the angle between two of the measured vectors could be made—the vectors inclined above and below the horizontal—because of slightly better optical access at the window. The laser sheet was located normal to the test section axis 30 in. downstream of the flap tip, and the object plane was nominally centered at the location of the flap-edge vortex. DGV measurements were made at an angle of attack of  $10^\circ$  and a flap deflection of  $39^\circ$  for two free-stream dynamic pressures, 40 and 52 psf.

The flow was seeded as in the previous test using a vapor condensation smoke generator located upstream of the model in the wind tunnel settling chamber. Its position was also optimized to produce the most uniform coverage of the measurement area, but the seed was again pulled into the vortex flow. Accumulation of the smoke in the circuit helped to seed the free-stream areas. However, a somewhat higher ambient temperature than in March caused a noticeable decrease in the overall seed accumulation. Runs were conducted in the cooler temperatures of

the early morning to improve accumulation, and a second smoke generator, placed on the floor of the settling chamber, was used to supplement the primary unit. The fogging fluid was injected at a combined average rate of about 0.5 gph, and a total of 5 gal of the fluid was used during the cumulative run time of about 10 hr.

Sample mean orthogonal-velocity results are shown in figure 25. The figure is an average of 100 frames taken at a free-stream velocity of 74 m/s, after correction for the blockage of the wing and false walls. The object plane has been rotated to simulate a perpendicular view from a location downstream of the wing, and the origin of the figure is at the tip of the flap edge. In this case, the spanwise component is positive up, and the downwash component is positive to the right.

The system response curves were again acquired in situ immediately prior to acquiring images, and no evidence of significant bias due to drift of the curves is apparent. The correct streamwise velocity is shown in the images along with a crossflow velocity at the center of the vortex that is essentially zero. Notice also that the images have smoother, less speckled appearance than the previous results because of the larger 100-image sample and the resulting decrease in random uncertainty.

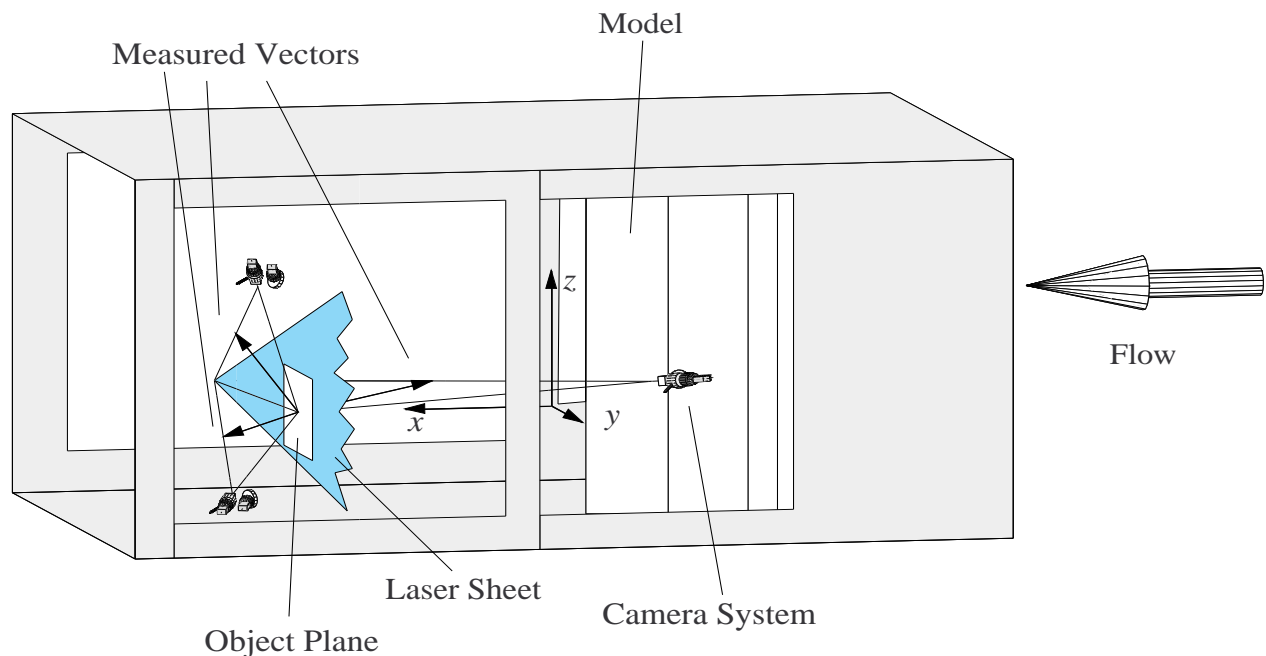


Figure 24. Test section diagram showing the camera locations, laser sheet, and the directions of the measured components.

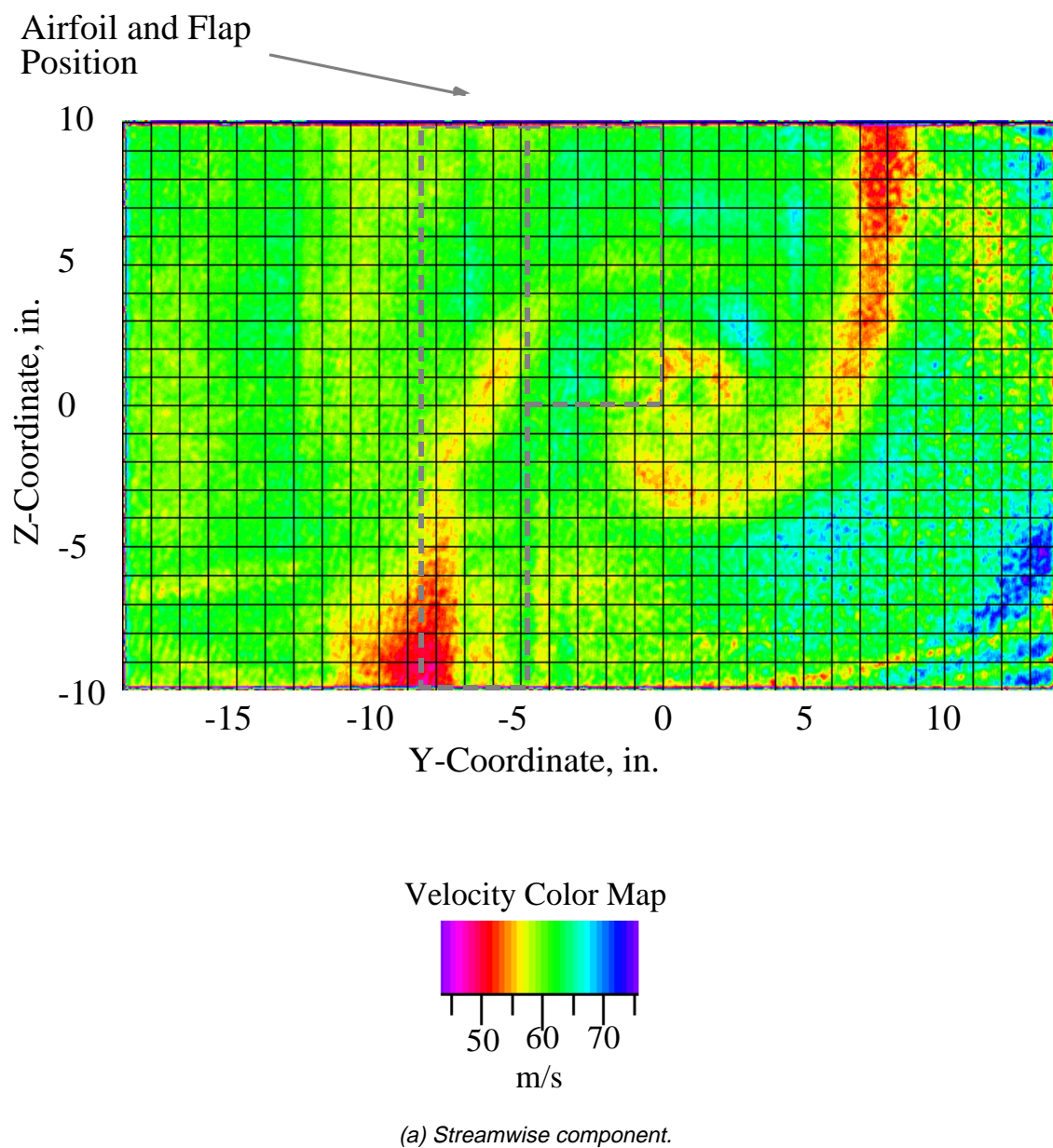
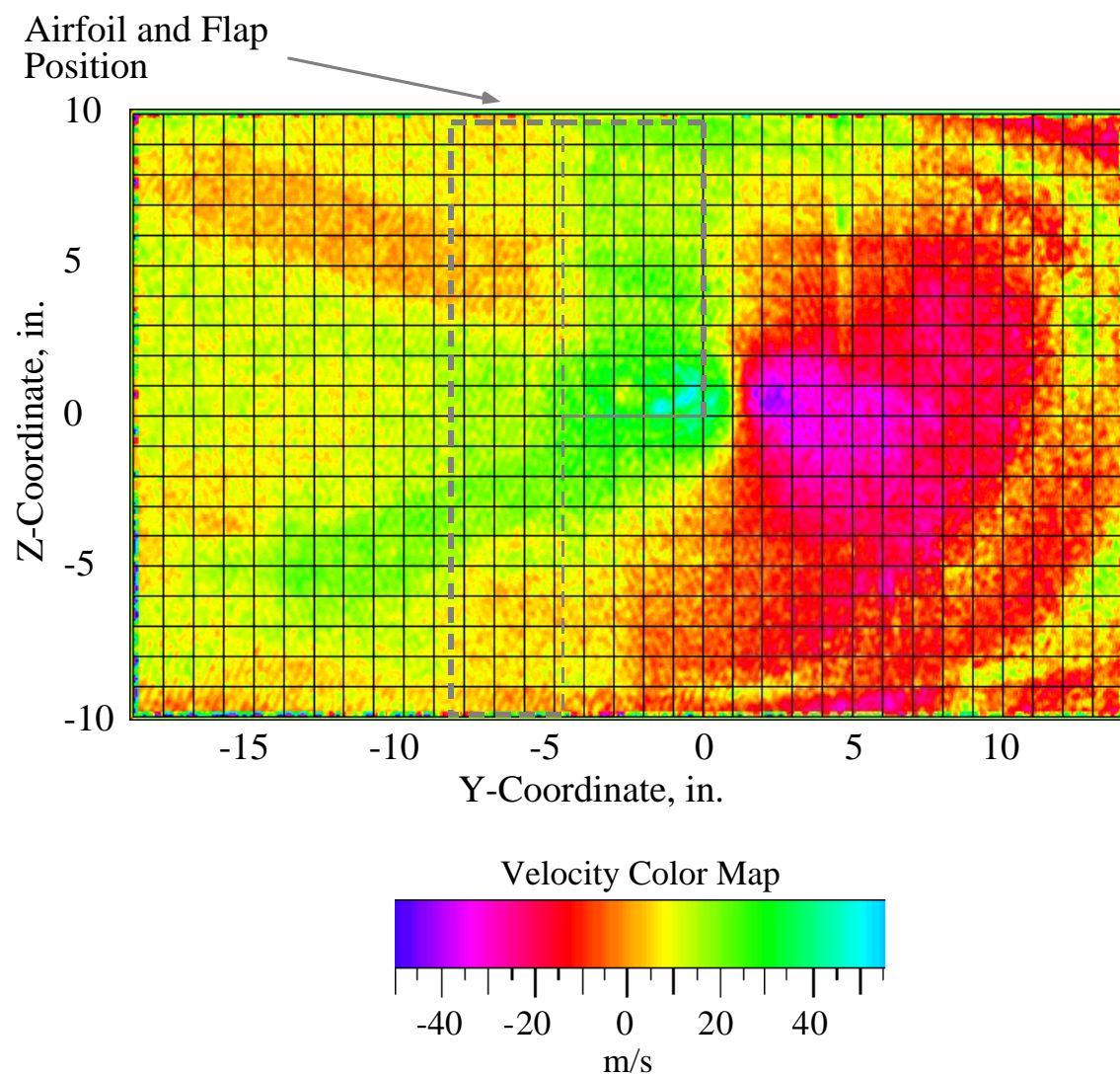


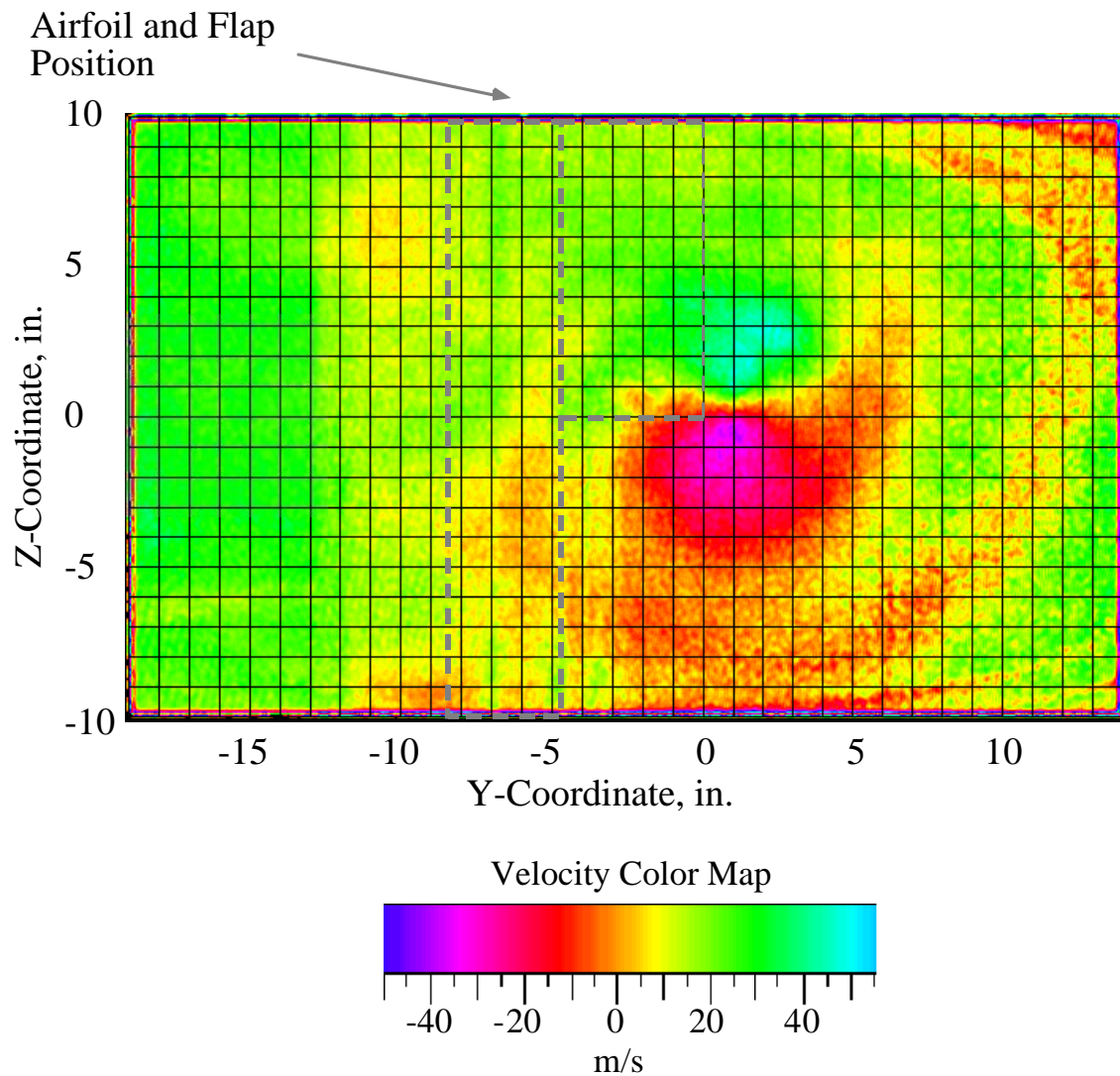
Figure 25. Measured mean orthogonal components of the flap-edge vortical flow field (looking upstream).





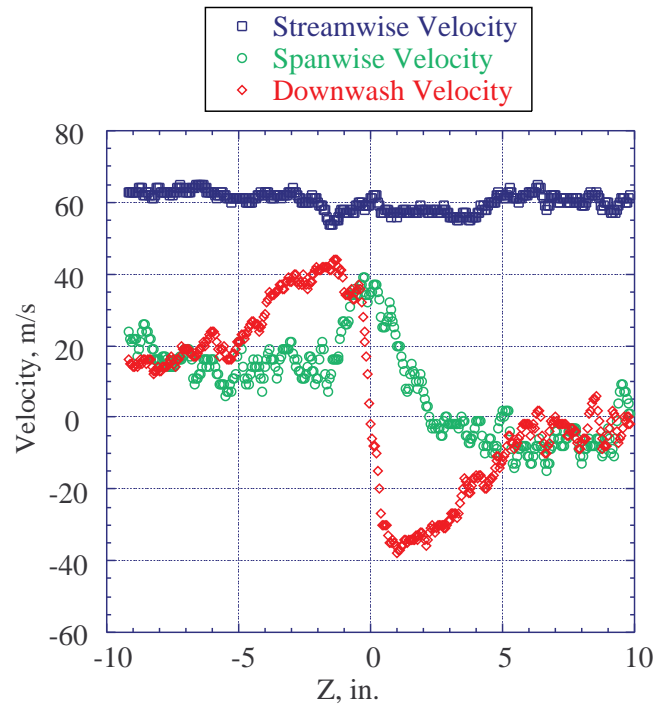
(b) Spanwise component (positive up).

Figure 25. Continued.

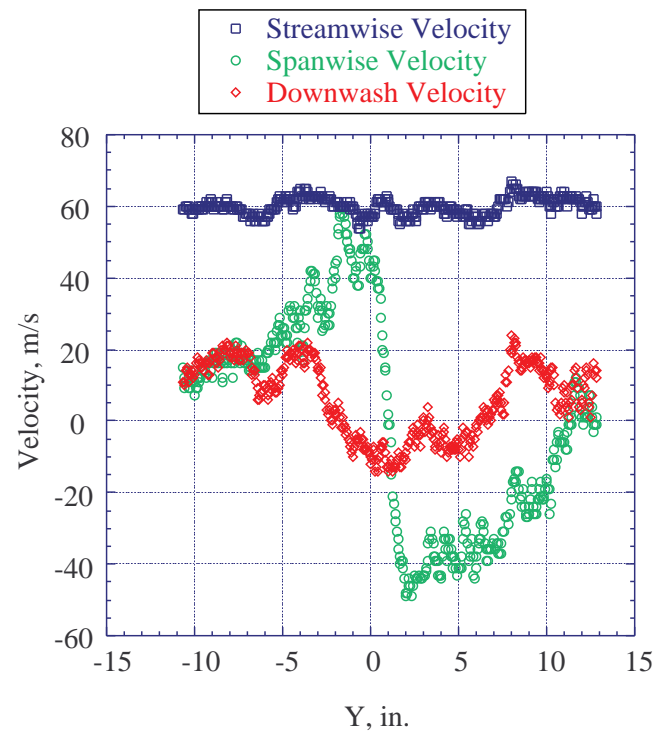


(c) Downwash component (positive to the right).

Figure 25. Continued.



(d) Vertical profile through center of vortex.



(e) Horizontal profile through center of vortex.

Figure 25. Concluded.

The vortex position is clearly shown in the streamwise-component image. At this measuring location, the region of velocity deficiency in the viscous wake of the wing is displaced by the rotational flow, forming the double spiral pattern. The crossflow images also clearly show the vortex position, which is centered about 1 in. below the flap tip at this station, and a peak rotational velocity of about 60 m/s.

Equations (16), (17) and (18) are again used to compute uncertainty estimates for this measurement geometry. The streamwise, spanwise, and downwash precision uncertainty intervals are estimated to be  $\pm 0.8$ ,  $\pm 3$ , and  $\pm 2$  m/s, respectively, for the 100-image averages with 95% confidence. Although the images are significantly smoother because of this lower uncertainty, some background and flatfield artifacts remain in the images. Future work will focus on developing improved techniques to better remove these artifacts.

## Conclusions

This work demonstrates the successful application of the DGV measurement technique in the Ames 40- by 80-Foot and 7- by 10-Foot Wind Tunnels using low-cost cameras and computer equipment. Wind tunnel measurements are presented that show a progression of success as installation problems were solved and calibration procedures were improved.

An analysis of measurement uncertainty shows that uncertainty due to random effects is caused primarily by

the radiometric noise sources of the camera. Precision uncertainty is expressed as an absolute uncertainty interval, which is predicted to be  $\pm 5$  m/s for a single image or  $\pm 0.5$  m/s for a 100-image average, both at 68% confidence. This uncertainty is shown to propagate from direct velocity measurements when they are converted to orthogonal vector components. The conversion is made using an algebraic transformation that is developed for a general measurement geometry, and a method is presented for propagating the uncertainty. For a typical forward-scatter viewing geometry, the method predicts single-image precision uncertainties of  $\pm 4$ ,  $\pm 7$ , and  $\pm 6$  m/s, respectively, for the  $U$ ,  $V$ , and  $W$  components at 68% confidence. Wind tunnel measurements are presented that show other configurations and the associated uncertainties.

The results demonstrate the feasibility of using the DGV technique in the research environment of large wind tunnels. For production testing, however, a number of improvements are planned to increase efficiency. Data processing could be further automated, and calibration techniques could be further refined. A pulsed, frequency-doubled Nd:YAG laser could be used in place of the argon laser. This new laser would provide more laser power with a substantial increase in the intensity of the light scattered by the seed particles. This increase would result in a reduction in the quantity of seed that must be injected into the flow for a particular test. It would also permit shuttering of the cameras and eliminate the requirement to acquire images under darkened conditions.

## Appendix A

### Unit Vectors for General-Case Viewing Geometry

The unit vectors for each of the three camera locations are given by the expressions

$$\begin{aligned}
 (\hat{k}_1 - \hat{l}) &= \frac{1}{A_1} \left[ \left\{ \frac{x_1 - x_i}{\sqrt{(x_1 - x_i)^2 + (y_1 - y_i)^2 + (z_1 - z_i)^2}} - \frac{x_i - x_s}{\sqrt{(x_i - x_s)^2 + (y_i - y_s)^2 + (z_i - z_s)^2}} \right\} \hat{i} \right. \\
 &\quad + \left\{ \frac{y_1 - y_i}{\sqrt{(x_1 - x_i)^2 + (y_1 - y_i)^2 + (z_1 - z_i)^2}} - \frac{y_i - y_s}{\sqrt{(x_i - x_s)^2 + (y_i - y_s)^2 + (z_i - z_s)^2}} \right\} \hat{j} \\
 &\quad \left. + \left\{ \frac{z_1 - z_i}{\sqrt{(x_1 - x_i)^2 + (y_1 - y_i)^2 + (z_1 - z_i)^2}} - \frac{z_i - z_s}{\sqrt{(x_i - x_s)^2 + (y_i - y_s)^2 + (z_i - z_s)^2}} \right\} \hat{k} \right] \\
 (\hat{k}_2 - \hat{l}) &= \frac{1}{A_2} \left[ \left\{ \frac{x_2 - x_i}{\sqrt{(x_2 - x_i)^2 + (y_2 - y_i)^2 + (z_2 - z_i)^2}} - \frac{x_i - x_s}{\sqrt{(x_i - x_s)^2 + (y_i - y_s)^2 + (z_i - z_s)^2}} \right\} \hat{i} \right. \\
 &\quad + \left\{ \frac{y_2 - y_i}{\sqrt{(x_2 - x_i)^2 + (y_2 - y_i)^2 + (z_2 - z_i)^2}} - \frac{y_i - y_s}{\sqrt{(x_i - x_s)^2 + (y_i - y_s)^2 + (z_i - z_s)^2}} \right\} \hat{j} \\
 &\quad \left. + \left\{ \frac{z_2 - z_i}{\sqrt{(x_2 - x_i)^2 + (y_2 - y_i)^2 + (z_2 - z_i)^2}} - \frac{z_i - z_s}{\sqrt{(x_i - x_s)^2 + (y_i - y_s)^2 + (z_i - z_s)^2}} \right\} \hat{k} \right] \\
 (\hat{k}_3 - \hat{l}) &= \frac{1}{A_3} \left[ \left\{ \frac{x_3 - x_i}{\sqrt{(x_3 - x_i)^2 + (y_3 - y_i)^2 + (z_3 - z_i)^2}} - \frac{x_i - x_s}{\sqrt{(x_i - x_s)^2 + (y_i - y_s)^2 + (z_i - z_s)^2}} \right\} \hat{i} \right. \\
 &\quad + \left\{ \frac{y_3 - y_i}{\sqrt{(x_3 - x_i)^2 + (y_3 - y_i)^2 + (z_3 - z_i)^2}} - \frac{y_i - y_s}{\sqrt{(x_i - x_s)^2 + (y_i - y_s)^2 + (z_i - z_s)^2}} \right\} \hat{j} \\
 &\quad \left. + \left\{ \frac{z_3 - z_i}{\sqrt{(x_3 - x_i)^2 + (y_3 - y_i)^2 + (z_3 - z_i)^2}} - \frac{z_i - z_s}{\sqrt{(x_i - x_s)^2 + (y_i - y_s)^2 + (z_i - z_s)^2}} \right\} \hat{k} \right]
 \end{aligned}$$

where

$$\begin{aligned}
A_1 &= \left[ \left\{ \frac{x_1 - x_i}{\sqrt{(x_1 - x_i)^2 + (y_1 - y_i)^2 + (z_1 - z_i)^2}} - \frac{x_i - x_s}{\sqrt{(x_i - x_s)^2 + (y_i - y_s)^2 + (z_i - z_s)^2}} \right\}^2 \right. \\
&\quad + \left\{ \frac{y_1 - y_i}{\sqrt{(x_1 - x_i)^2 + (y_1 - y_i)^2 + (z_1 - z_i)^2}} - \frac{y_i - y_s}{\sqrt{(x_i - x_s)^2 + (y_i - y_s)^2 + (z_i - z_s)^2}} \right\}^2 \\
&\quad \left. + \left\{ \frac{z_1 - z_i}{\sqrt{(x_1 - x_i)^2 + (y_1 - y_i)^2 + (z_1 - z_i)^2}} - \frac{z_i - z_s}{\sqrt{(x_i - x_s)^2 + (y_i - y_s)^2 + (z_i - z_s)^2}} \right\}^2 \right]^{1/2} \\
A_2 &= \left[ \left\{ \frac{x_2 - x_i}{\sqrt{(x_2 - x_i)^2 + (y_2 - y_i)^2 + (z_2 - z_i)^2}} - \frac{x_i - x_s}{\sqrt{(x_i - x_s)^2 + (y_i - y_s)^2 + (z_i - z_s)^2}} \right\}^2 \right. \\
&\quad + \left\{ \frac{y_2 - y_i}{\sqrt{(x_2 - x_i)^2 + (y_2 - y_i)^2 + (z_2 - z_i)^2}} - \frac{y_i - y_s}{\sqrt{(x_i - x_s)^2 + (y_i - y_s)^2 + (z_i - z_s)^2}} \right\}^2 \\
&\quad \left. + \left\{ \frac{z_2 - z_i}{\sqrt{(x_2 - x_i)^2 + (y_2 - y_i)^2 + (z_2 - z_i)^2}} - \frac{z_i - z_s}{\sqrt{(x_i - x_s)^2 + (y_i - y_s)^2 + (z_i - z_s)^2}} \right\}^2 \right]^{1/2} \\
A_3 &= \left[ \left\{ \frac{x_3 - x_i}{\sqrt{(x_3 - x_i)^2 + (y_3 - y_i)^2 + (z_3 - z_i)^2}} - \frac{x_i - x_s}{\sqrt{(x_i - x_s)^2 + (y_i - y_s)^2 + (z_i - z_s)^2}} \right\}^2 \right. \\
&\quad + \left\{ \frac{y_3 - y_i}{\sqrt{(x_3 - x_i)^2 + (y_3 - y_i)^2 + (z_3 - z_i)^2}} - \frac{y_i - y_s}{\sqrt{(x_i - x_s)^2 + (y_i - y_s)^2 + (z_i - z_s)^2}} \right\}^2 \\
&\quad \left. + \left\{ \frac{z_3 - z_i}{\sqrt{(x_3 - x_i)^2 + (y_3 - y_i)^2 + (z_3 - z_i)^2}} - \frac{z_i - z_s}{\sqrt{(x_i - x_s)^2 + (y_i - y_s)^2 + (z_i - z_s)^2}} \right\}^2 \right]^{1/2}
\end{aligned}$$

and

- $x_1, y_1, z_1$  = coordinates of camera a
- $x_2, y_2, z_2$  = coordinates of camera b
- $x_3, y_3, z_3$  = coordinates of camera c
- $x_i, y_i, z_i$  = coordinates of the  $i$ th pixel, projected onto the object plane
- $x_i, y_i, z_i$  = coordinates of the laser sheet origin

## Appendix B

### U-, V-, and W-Component Precision Uncertainty

The  $U$ -component precision uncertainty is given by the expression

$$\begin{aligned}
 \sigma_U = \sqrt{ & \left\{ \frac{(-Y_3 Z_2 + Y_2 Z_3)^2 \text{Prec}[U_{ma}]^2}{(-X_3 Y_2 Z_1 + X_2 Y_3 Z_1 + X_3 Y_1 Z_2 - X_1 Y_3 Z_2 - X_2 Y_1 Z_3 + X_1 Y_2 Z_3)^2} \right. \\
 & + \frac{(Y_3 Z_1 - Y_1 Z_3)^2 \text{Prec}[U_{mb}]^2}{(-X_3 Y_2 Z_1 + X_2 Y_3 Z_1 + X_3 Y_1 Z_2 - X_1 Y_3 Z_2 - X_2 Y_1 Z_3 + X_1 Y_2 Z_3)^2} \\
 & + \frac{(-Y_2 Z_1 + Y_1 Z_2)^2 \text{Prec}[U_{mc}]^2}{(-X_3 Y_2 Z_1 + X_2 Y_3 Z_1 + X_3 Y_1 Z_2 - X_1 Y_3 Z_2 - X_2 Y_1 Z_3 + X_1 Y_2 Z_3)^2} \\
 & + \frac{(-Y_3 Z_2 + Y_2 Z_3)^2 (U_{mc}(-Y_2 Z_1 + Y_1 Z_2) - U_{mb}(-Y_3 Z_1 + Y_1 Z_3) + U_{ma}(-Y_3 Z_2 + Y_2 Z_3))^2 \text{Prec}[X_1]^2}{(-X_3 Y_2 Z_1 + X_2 Y_3 Z_1 + X_3 Y_1 Z_2 - X_1 Y_3 Z_2 - X_2 Y_1 Z_3 + X_1 Y_2 Z_3)^4} \\
 & + \frac{(Y_3 Z_1 - Y_1 Z_3)^2 (U_{mc}(-Y_2 Z_1 + Y_1 Z_2) - U_{mb}(-Y_3 Z_1 + Y_1 Z_3) + U_{ma}(-Y_3 Z_2 + Y_2 Z_3))^2 \text{Prec}[X_2]^2}{(-X_3 Y_2 Z_1 + X_2 Y_3 Z_1 + X_3 Y_1 Z_2 - X_1 Y_3 Z_2 - X_2 Y_1 Z_3 + X_1 Y_2 Z_3)^4} \\
 & + \frac{(-Y_2 Z_1 + Y_1 Z_2)^2 (U_{mc}(-Y_2 Z_1 + Y_1 Z_2) - U_{mb}(-Y_3 Z_1 + Y_1 Z_3) + U_{ma}(-Y_3 Z_2 + Y_2 Z_3))^2 \text{Prec}[X_3]^2}{(-X_3 Y_2 Z_1 + X_2 Y_3 Z_1 + X_3 Y_1 Z_2 - X_1 Y_3 Z_2 - X_2 Y_1 Z_3 + X_1 Y_2 Z_3)^4} \\
 & + \left( \frac{U_{mc} Z_2 - U_{mb} Z_3}{-X_3 Y_2 Z_1 + X_2 Y_3 Z_1 + X_3 Y_1 Z_2 - X_1 Y_3 Z_2 - X_2 Y_1 Z_3 + X_1 Y_2 Z_3} - \frac{(X_3 Z_2 - X_2 Z_3)(U_{mc}(-Y_2 Z_1 + Y_1 Z_2) - U_{mb}(-Y_3 Z_1 + Y_1 Z_3) + U_{ma}(-Y_3 Z_2 + Y_2 Z_3))}{(-X_3 Y_2 Z_1 + X_2 Y_3 Z_1 + X_3 Y_1 Z_2 - X_1 Y_3 Z_2 - X_2 Y_1 Z_3 + X_1 Y_2 Z_3)^2} \right)^2 \text{Prec}[Y_1]^2 \\
 & + \left( \frac{-U_{mc} Z_1 + U_{ma} Z_3}{-X_3 Y_2 Z_1 + X_2 Y_3 Z_1 + X_3 Y_1 Z_2 - X_1 Y_3 Z_2 - X_2 Y_1 Z_3 + X_1 Y_2 Z_3} - \frac{(-X_3 Z_1 + X_1 Z_3)(U_{mc}(-Y_2 Z_1 + Y_1 Z_2) - U_{mb}(-Y_3 Z_1 + Y_1 Z_3) + U_{ma}(-Y_3 Z_2 + Y_2 Z_3))}{(-X_3 Y_2 Z_1 + X_2 Y_3 Z_1 + X_3 Y_1 Z_2 - X_1 Y_3 Z_2 - X_2 Y_1 Z_3 + X_1 Y_2 Z_3)^2} \right)^2 \text{Prec}[Y_2]^2 \\
 & + \left( \frac{-U_{mb} Z_1 + U_{ma} Z_2}{-X_3 Y_2 Z_1 + X_2 Y_3 Z_1 + X_3 Y_1 Z_2 - X_1 Y_3 Z_2 - X_2 Y_1 Z_3 + X_1 Y_2 Z_3} - \frac{(X_2 Z_1 - X_1 Z_2)(U_{mc}(-Y_2 Z_1 + Y_1 Z_2) - U_{mb}(-Y_3 Z_1 + Y_1 Z_3) + U_{ma}(-Y_3 Z_2 + Y_2 Z_3))}{(-X_3 Y_2 Z_1 + X_2 Y_3 Z_1 + X_3 Y_1 Z_2 - X_1 Y_3 Z_2 - X_2 Y_1 Z_3 + X_1 Y_2 Z_3)^2} \right)^2 \text{Prec}[Y_3]^2 \\
 & + \left( \frac{-U_{mc} Y_2 + U_{mb} Y_3}{-X_3 Y_2 Z_1 + X_2 Y_3 Z_1 + X_3 Y_1 Z_2 - X_1 Y_3 Z_2 - X_2 Y_1 Z_3 + X_1 Y_2 Z_3} - \frac{(-X_3 Y_2 + X_2 Y_3)(U_{mc}(-Y_2 Z_1 + Y_1 Z_2) - U_{mb}(-Y_3 Z_1 + Y_1 Z_3) + U_{ma}(-Y_3 Z_2 + Y_2 Z_3))}{(-X_3 Y_2 Z_1 + X_2 Y_3 Z_1 + X_3 Y_1 Z_2 - X_1 Y_3 Z_2 - X_2 Y_1 Z_3 + X_1 Y_2 Z_3)^2} \right)^2 \text{Prec}[Z_1]^2 \\
 & + \left( \frac{U_{mc} Y_1 - U_{ma} Y_3}{-X_3 Y_2 Z_1 + X_2 Y_3 Z_1 + X_3 Y_1 Z_2 - X_1 Y_3 Z_2 - X_2 Y_1 Z_3 + X_1 Y_2 Z_3} - \frac{(X_3 Y_1 - X_1 Y_3)(U_{mc}(-Y_2 Z_1 + Y_1 Z_2) - U_{mb}(-Y_3 Z_1 + Y_1 Z_3) + U_{ma}(-Y_3 Z_2 + Y_2 Z_3))}{(-X_3 Y_2 Z_1 + X_2 Y_3 Z_1 + X_3 Y_1 Z_2 - X_1 Y_3 Z_2 - X_2 Y_1 Z_3 + X_1 Y_2 Z_3)^2} \right)^2 \text{Prec}[Z_2]^2 \\
 & + \left( \frac{-U_{mb} Y_1 + U_{ma} Y_2}{-X_3 Y_2 Z_1 + X_2 Y_3 Z_1 + X_3 Y_1 Z_2 - X_1 Y_3 Z_2 - X_2 Y_1 Z_3 + X_1 Y_2 Z_3} - \frac{(-X_2 Y_1 + X_1 Y_2)(U_{mc}(-Y_2 Z_1 + Y_1 Z_2) - U_{mb}(-Y_3 Z_1 + Y_1 Z_3) + U_{ma}(-Y_3 Z_2 + Y_2 Z_3))}{(-X_3 Y_2 Z_1 + X_2 Y_3 Z_1 + X_3 Y_1 Z_2 - X_1 Y_3 Z_2 - X_2 Y_1 Z_3 + X_1 Y_2 Z_3)^2} \right)^2 \text{Prec}[Z_3]^2 \Big\}
 \end{aligned}$$

where

- $U_{ma}$  = magnitude of the measured component from camera view a
- $U_{mb}$  = magnitude of the measured component from camera view b
- $U_{mc}$  = magnitude of the measured component from camera view c
- $X_1, Y_1, Z_1$  = unit vector components defining the direction of  $\vec{U}_{ma}$

$X_2, Y_2, Z_2$  = unit vector components defining the direction of  $\vec{U}_{mb}$

$X_3, Y_3, Z_3$  = unit vector components defining the direction of  $\vec{U}_{mc}$

$\text{Prec}[U_{ma}] = \sigma_a$

$\text{Prec}[U_{mb}] = \sigma_b$

$\text{Prec}[U_{mc}] = \sigma_c$

$\text{Prec}[X_1] = \sigma_{X_1}$

$\text{Prec}[X_2] = \sigma_{X_2}$

$\text{Prec}[X_3] = \sigma_{X_3}$

$\text{Prec}[Y_1] = \sigma_{Y_1}$

$\text{Prec}[Y_2] = \sigma_{Y_2}$

$\text{Prec}[Y_3] = \sigma_{Y_3}$

$\text{Prec}[Z_1] = \sigma_{Z_1}$

$\text{Prec}[Z_2] = \sigma_{Z_2}$

$\text{Prec}[Z_3] = \sigma_{Z_3}$



The V-component precision uncertainty is given by the expression

$$\begin{aligned}
\sigma_V = & \sqrt{\left\{ \frac{(X_3 Z_2 - X_2 Z_3)^2 \text{Prec}[U_{ma}]^2}{(-X_3 Y_2 Z_1 + X_2 Y_3 Z_1 + X_3 Y_1 Z_2 - X_1 Y_3 Z_2 - X_2 Y_1 Z_3 + X_1 Y_2 Z_3)^2} \right.} \\
& + \frac{(-X_3 Z_1 + X_1 Z_3)^2 \text{Prec}[U_{mb}]^2}{(-X_3 Y_2 Z_1 + X_2 Y_3 Z_1 + X_3 Y_1 Z_2 - X_1 Y_3 Z_2 - X_2 Y_1 Z_3 + X_1 Y_2 Z_3)^2} \\
& + \frac{(X_2 Z_1 - X_1 Z_2)^2 \text{Prec}[U_{mc}]^2}{(-X_3 Y_2 Z_1 + X_2 Y_3 Z_1 + X_3 Y_1 Z_2 - X_1 Y_3 Z_2 - X_2 Y_1 Z_3 + X_1 Y_2 Z_3)^2} \\
& + \left( \frac{-U_{mc} Z_2 + U_{mb} Z_3}{(-X_3 Y_2 Z_1 + X_2 Y_3 Z_1 + X_3 Y_1 Z_2 - X_1 Y_3 Z_2 - X_2 Y_1 Z_3 + X_1 Y_2 Z_3)} - \frac{(-Y_3 Z_2 + Y_2 Z_3)(X_3(-U_{mb} Z_1 + U_{ma} Z_2) - X_2(-U_{mc} Z_1 + U_{ma} Z_3) + X_1(-U_{mc} Z_2 + U_{mb} Z_3))}{(-X_3 Y_2 Z_1 + X_2 Y_3 Z_1 + X_3 Y_1 Z_2 - X_1 Y_3 Z_2 - X_2 Y_1 Z_3 + X_1 Y_2 Z_3)^2} \right)^2 \text{Prec}[X_1]^2 \\
& + \left( \frac{U_{mc} Z_1 + U_{ma} Z_3}{(-X_3 Y_2 Z_1 + X_2 Y_3 Z_1 + X_3 Y_1 Z_2 - X_1 Y_3 Z_2 - X_2 Y_1 Z_3 + X_1 Y_2 Z_3)} - \frac{(Y_3 Z_1 - Y_1 Z_3)(X_3(-U_{mb} Z_1 + U_{ma} Z_2) - X_2(-U_{mc} Z_1 + U_{ma} Z_3) + X_1(-U_{mc} Z_2 + U_{mb} Z_3))}{(-X_3 Y_2 Z_1 + X_2 Y_3 Z_1 + X_3 Y_1 Z_2 - X_1 Y_3 Z_2 - X_2 Y_1 Z_3 + X_1 Y_2 Z_3)^2} \right)^2 \text{Prec}[X_2]^2 \\
& + \left( \frac{-U_{mb} Z_1 + U_{ma} Z_2}{(-X_3 Y_2 Z_1 + X_2 Y_3 Z_1 + X_3 Y_1 Z_2 - X_1 Y_3 Z_2 - X_2 Y_1 Z_3 + X_1 Y_2 Z_3)} - \frac{(-Y_2 Z_1 + Y_1 Z_2)(X_3(-U_{mb} Z_1 + U_{ma} Z_2) - X_2(-U_{mc} Z_1 + U_{ma} Z_3) + X_1(-U_{mc} Z_2 + U_{mb} Z_3))}{(-X_3 Y_2 Z_1 + X_2 Y_3 Z_1 + X_3 Y_1 Z_2 - X_1 Y_3 Z_2 - X_2 Y_1 Z_3 + X_1 Y_2 Z_3)^2} \right)^2 \text{Prec}[X_3]^2 \\
& + \frac{(X_3 Z_2 - X_2 Z_3)^2 (X_3(-U_{mb} Z_1 + U_{ma} Z_2) - X_2(-U_{mc} Z_1 + U_{ma} Z_3) + X_1(-U_{mc} Z_2 + U_{mb} Z_3))^2 \text{Prec}[Y_1]^2}{(-X_3 Y_2 Z_1 + X_2 Y_3 Z_1 + X_3 Y_1 Z_2 - X_1 Y_3 Z_2 - X_2 Y_1 Z_3 + X_1 Y_2 Z_3)^4} \\
& + \frac{(-X_3 Z_1 + X_1 Z_3)^2 (X_3(-U_{mb} Z_1 + U_{ma} Z_2) - X_2(-U_{mc} Z_1 + U_{ma} Z_3) + X_1(-U_{mc} Z_2 + U_{mb} Z_3))^2 \text{Prec}[Y_2]^2}{(-X_3 Y_2 Z_1 + X_2 Y_3 Z_1 + X_3 Y_1 Z_2 - X_1 Y_3 Z_2 - X_2 Y_1 Z_3 + X_1 Y_2 Z_3)^4} \\
& + \frac{(X_2 Z_1 - X_1 Z_2)^2 (X_3(-U_{mb} Z_1 + U_{ma} Z_2) - X_2(-U_{mc} Z_1 + U_{ma} Z_3) + X_1(-U_{mc} Z_2 + U_{mb} Z_3))^2 \text{Prec}[Y_3]^2}{(-X_3 Y_2 Z_1 + X_2 Y_3 Z_1 + X_3 Y_1 Z_2 - X_1 Y_3 Z_2 - X_2 Y_1 Z_3 + X_1 Y_2 Z_3)^4} \\
& + \left( \frac{U_{mc} X_2 - U_{mb} X_3}{(-X_3 Y_2 Z_1 + X_2 Y_3 Z_1 + X_3 Y_1 Z_2 - X_1 Y_3 Z_2 - X_2 Y_1 Z_3 + X_1 Y_2 Z_3)} - \frac{(-X_3 Y_2 + X_2 Y_3)(X_3(-U_{mb} Z_1 + U_{ma} Z_2) - X_2(-U_{mc} Z_1 + U_{ma} Z_3) + X_1(-U_{mc} Z_2 + U_{mb} Z_3))}{(-X_3 Y_2 Z_1 + X_2 Y_3 Z_1 + X_3 Y_1 Z_2 - X_1 Y_3 Z_2 - X_2 Y_1 Z_3 + X_1 Y_2 Z_3)^2} \right)^2 \text{Prec}[Z_1]^2 \\
& + \left( \frac{-U_{mc} X_1 + U_{ma} X_3}{(-X_3 Y_2 Z_1 + X_2 Y_3 Z_1 + X_3 Y_1 Z_2 - X_1 Y_3 Z_2 - X_2 Y_1 Z_3 + X_1 Y_2 Z_3)} - \frac{(X_3 Y_1 - X_1 Y_3)(X_3(-U_{mb} Z_1 + U_{ma} Z_2) - X_2(-U_{mc} Z_1 + U_{ma} Z_3) + X_1(-U_{mc} Z_2 + U_{mb} Z_3))}{(-X_3 Y_2 Z_1 + X_2 Y_3 Z_1 + X_3 Y_1 Z_2 - X_1 Y_3 Z_2 - X_2 Y_1 Z_3 + X_1 Y_2 Z_3)^2} \right)^2 \text{Prec}[Z_2]^2 \\
& + \left( \frac{U_{mb} X_1 - U_{ma} X_2}{(-X_3 Y_2 Z_1 + X_2 Y_3 Z_1 + X_3 Y_1 Z_2 - X_1 Y_3 Z_2 - X_2 Y_1 Z_3 + X_1 Y_2 Z_3)} - \frac{(-X_2 Y_1 + X_1 Y_2)(X_3(-U_{mb} Z_1 + U_{ma} Z_2) - X_2(-U_{mc} Z_1 + U_{ma} Z_3) + X_1(-U_{mc} Z_2 + U_{mb} Z_3))}{(-X_3 Y_2 Z_1 + X_2 Y_3 Z_1 + X_3 Y_1 Z_2 - X_1 Y_3 Z_2 - X_2 Y_1 Z_3 + X_1 Y_2 Z_3)^2} \right)^2 \text{Prec}[Z_3]^2 \Big\}
\end{aligned}$$

The  $W$ -component precision uncertainty is given by the expression

$$\begin{aligned}
\sigma_W = & \sqrt{\left\{ \frac{(-X_3 Y_2 + X_2 Y_3)^2 \text{Prec}[U_{ma}]^2}{(-X_3 Y_2 Z_1 + X_2 Y_3 Z_1 + X_3 Y_1 Z_2 - X_1 Y_3 Z_2 - X_2 Y_1 Z_3 + X_1 Y_2 Z_3)^2} \right. \\
& + \frac{(X_3 Y_1 - X_1 Y_3)^2 \text{Prec}[U_{mb}]^2}{(-X_3 Y_2 Z_1 + X_2 Y_3 Z_1 + X_3 Y_1 Z_2 - X_1 Y_3 Z_2 - X_2 Y_1 Z_3 + X_1 Y_2 Z_3)^2} \\
& + \frac{(-X_2 Y_1 + X_1 Y_2)^2 \text{Prec}[U_{mc}]^2}{(-X_3 Y_2 Z_1 + X_2 Y_3 Z_1 + X_3 Y_1 Z_2 - X_1 Y_3 Z_2 - X_2 Y_1 Z_3 + X_1 Y_2 Z_3)^2} \\
& + \left( -\frac{(X_3(U_{mb} Y_1 - U_{ma} Y_2) - X_2(U_{mc} Y_1 - U_{ma} Y_3) + X_1(U_{mc} Y_2 - U_{mb} Y_3))(-Y_3 Z_2 + Y_2 Z_3)}{(-X_3 Y_2 Z_1 + X_2 Y_3 Z_1 + X_3 Y_1 Z_2 - X_1 Y_3 Z_2 - X_2 Y_1 Z_3 + X_1 Y_2 Z_3)^2} + \frac{U_{mc} Y_2 + U_{mb} Y_3}{-X_3 Y_2 Z_1 + X_2 Y_3 Z_1 + X_3 Y_1 Z_2 - X_1 Y_3 Z_2 - X_2 Y_1 Z_3 + X_1 Y_2 Z_3} \right)^2 \text{Prec}[X_1]^2 \\
& + \left( -\frac{(X_3(U_{mb} Y_1 - U_{ma} Y_2) - X_2(U_{mc} Y_1 - U_{ma} Y_3) + X_1(U_{mc} Y_2 - U_{mb} Y_3))(-Y_3 Z_1 - Y_1 Z_3)}{(-X_3 Y_2 Z_1 + X_2 Y_3 Z_1 + X_3 Y_1 Z_2 - X_1 Y_3 Z_2 - X_2 Y_1 Z_3 + X_1 Y_2 Z_3)^2} + \frac{-U_{mc} Y_1 + U_{ma} Y_3}{-X_3 Y_2 Z_1 + X_2 Y_3 Z_1 + X_3 Y_1 Z_2 - X_1 Y_3 Z_2 - X_2 Y_1 Z_3 + X_1 Y_2 Z_3} \right)^2 \text{Prec}[X_2]^2 \\
& + \left( -\frac{(X_3(U_{mb} Y_1 - U_{ma} Y_2) - X_2(U_{mc} Y_1 - U_{ma} Y_3) + X_1(U_{mc} Y_2 - U_{mb} Y_3))(-Y_2 Z_1 + Y_1 Z_2)}{(-X_3 Y_2 Z_1 + X_2 Y_3 Z_1 + X_3 Y_1 Z_2 - X_1 Y_3 Z_2 - X_2 Y_1 Z_3 + X_1 Y_2 Z_3)^2} + \frac{U_{mb} Y_1 - U_{ma} Y_2}{-X_3 Y_2 Z_1 + X_2 Y_3 Z_1 + X_3 Y_1 Z_2 - X_1 Y_3 Z_2 - X_2 Y_1 Z_3 + X_1 Y_2 Z_3} \right)^2 \text{Prec}[X_3]^2 \\
& + \left( -\frac{(X_3(U_{mb} Y_1 - U_{ma} Y_2) - X_2(U_{mc} Y_1 - U_{ma} Y_3) + X_1(U_{mc} Y_2 - U_{mb} Y_3))(X_3 Z_2 - X_2 Z_3)}{(-X_3 Y_2 Z_1 + X_2 Y_3 Z_1 + X_3 Y_1 Z_2 - X_1 Y_3 Z_2 - X_2 Y_1 Z_3 + X_1 Y_2 Z_3)^2} + \frac{-U_{mc} X_2 + U_{mb} X_3}{-X_3 Y_2 Z_1 + X_2 Y_3 Z_1 + X_3 Y_1 Z_2 - X_1 Y_3 Z_2 - X_2 Y_1 Z_3 + X_1 Y_2 Z_3} \right)^2 \text{Prec}[Y_1]^2 \\
& + \left( -\frac{(X_3(U_{mb} Y_1 - U_{ma} Y_2) - X_2(U_{mc} Y_1 - U_{ma} Y_3) + X_1(U_{mc} Y_2 - U_{mb} Y_3))(-X_3 Z_1 + X_1 Z_3)}{(-X_3 Y_2 Z_1 + X_2 Y_3 Z_1 + X_3 Y_1 Z_2 - X_1 Y_3 Z_2 - X_2 Y_1 Z_3 + X_1 Y_2 Z_3)^2} + \frac{U_{mc} X_1 - U_{ma} X_3}{-X_3 Y_2 Z_1 + X_2 Y_3 Z_1 + X_3 Y_1 Z_2 - X_1 Y_3 Z_2 - X_2 Y_1 Z_3 + X_1 Y_2 Z_3} \right)^2 \text{Prec}[Y_2]^2 \\
& + \left( -\frac{(X_3(U_{mb} Y_1 - U_{ma} Y_2) - X_2(U_{mc} Y_1 - U_{ma} Y_3) + X_1(U_{mc} Y_2 - U_{mb} Y_3))(X_2 Z_1 - X_1 Z_2)}{(-X_3 Y_2 Z_1 + X_2 Y_3 Z_1 + X_3 Y_1 Z_2 - X_1 Y_3 Z_2 - X_2 Y_1 Z_3 + X_1 Y_2 Z_3)^2} + \frac{-U_{mb} X_1 + U_{ma} X_2}{-X_3 Y_2 Z_1 + X_2 Y_3 Z_1 + X_3 Y_1 Z_2 - X_1 Y_3 Z_2 - X_2 Y_1 Z_3 + X_1 Y_2 Z_3} \right)^2 \text{Prec}[Y_3]^2 \\
& + \frac{(-X_3 Y_2 + X_2 Y_3)^2 (X_3(U_{mb} Y_1 - U_{ma} Y_2) - X_2(U_{mc} Y_1 - U_{ma} Y_3) + X_1(U_{mc} Y_2 - U_{mb} Y_3))^2 \text{Prec}[Z_1]^2}{(-X_3 Y_2 Z_1 + X_2 Y_3 Z_1 + X_3 Y_1 Z_2 - X_1 Y_3 Z_2 - X_2 Y_1 Z_3 + X_1 Y_2 Z_3)^4} \\
& + \frac{(X_3 Y_1 - X_1 Y_3)^2 (X_3(U_{mb} Y_1 - U_{ma} Y_2) - X_2(U_{mc} Y_1 - U_{ma} Y_3) + X_1(U_{mc} Y_2 - U_{mb} Y_3))^2 \text{Prec}[Z_2]^2}{(-X_3 Y_2 Z_1 + X_2 Y_3 Z_1 + X_3 Y_1 Z_2 - X_1 Y_3 Z_2 - X_2 Y_1 Z_3 + X_1 Y_2 Z_3)^4} \\
& + \left. \frac{(-X_2 Y_1 + X_1 Y_2)^2 (X_3(U_{mb} Y_1 - U_{ma} Y_2) - X_2(U_{mc} Y_1 - U_{ma} Y_3) + X_1(U_{mc} Y_2 - U_{mb} Y_3))^2 \text{Prec}[Z_3]^2}{(-X_3 Y_2 Z_1 + X_2 Y_3 Z_1 + X_3 Y_1 Z_2 - X_1 Y_3 Z_2 - X_2 Y_1 Z_3 + X_1 Y_2 Z_3)^4} \right\}
\end{aligned}$$

## References

1. Reinath, M. S.: A Long-Range Laser Velocimeter. IEEE Transactions on Aerospace and Electronic Systems, vol. 27, no. 1, Jan. 1991, pp. 125–138. (Also NASA TM-101081, June 1989.)
2. Lourenco, L. M.: Particle Image Velocimetry. von Karman Institute for Fluid Dynamics Lecture Series 1996-03, June 3–7, 1996.
3. Komine, H.; Brosnan, S. J.; Litton, A. B.; and Stappaerts, E. A.: Real-Time, Doppler Global Velocimetry. AIAA Paper 91-0337, 29th Aerospace Sciences Meeting, Jan. 7–10, 1991, Reno, Nev.
4. Meyers, J. F.; and Komine, H.: Doppler Global Velocimetry—A New Way to Look at Velocity. ASME Fourth International Conference on Laser Anemometry, Aug. 23–27, 1991, Cleveland, Ohio.
5. Lee, J. W.; Meyers, J. F.; Cavone, A. A.; and Suzuki, K. E.: Doppler Global Velocimetry Measurements of the Vortical Flow Above an F/A-18. AIAA Paper 93-0414, 31st Aerospace Sciences Meeting, Jan. 11–14, 1993, Reno, Nev.
6. Castleman, K. R.: Digital Image Processing. Prentice-Hall, Inc., Englewood Cliffs, N.J., 1979.
7. Green, W. B.; Jepsen, P. L.; Kreznar, J. E.; Ruiz, R. M.; Schwartz, A. A.; and Seidman, J. B.: Removal of Instrument Signature from Mariner 9 Television Images of Mars. Applied Optics, vol. 14, no. 1, Jan. 1975.
8. Rindfleisch, T. C.: Digital Image Processing for the Rectification of Television Camera Distortions. Proceedings of the Space Applications of Camera Tubes International Colloquium, Paris, France, Nov. 23–25, 1971, pp. 331–350.
9. Soha, J. M.; Lynn, D. J.; Lorre, J. J.; Mosher, J. A.; Thayer, N. N.; Elliott, D. A.; Benton, W. D.; and Dewar, R. E.: IPL Processing of the Mariner 10 Images of Mercury. J. Geophys. Res., vol. 80, no. 17, June 1975, pp. 2394–2414.
10. McKenzie, R. L.: Measurement Capabilities of Planar Doppler Velocimetry Using Pulsed Lasers. Applied Optics, vol. 35, no. 6, Feb. 20, 1996, pp. 948–964. (Also AIAA Paper 95-0297, 1995.)
11. Meyers, J. F.: Doppler Global Velocimetry. The Next Generation? AIAA Paper 92-3897, 17th Aerospace Ground Testing Conference, July 6–8, 1992, Nashville, Tenn.
12. Assessment of Wind Tunnel Data Uncertainty. AIAA Standard S-071-1995, American Institute of Aeronautics and Astronautics, Washington, D.C., 1995.
13. McKenzie, R. L.: Planar Doppler Velocimetry Performance in Low-Speed Flows. AIAA Paper 97-0498, 35th Aerospace Sciences Meeting, Jan. 6–10, 1997, Reno, Nev.
14. Measurement Uncertainty. ANSI/ASME PTC 19.1-1985, Part 1, 1986. (Available from ASME Order Dept., 22 Law Drive, Box 2300, Fairfield, NJ 07007-2300.)
15. Buil, C.: CCD Astronomy: Construction and Use of an Astronomical CCD Camera. Willmann-Bell, Inc., Richmond, Va., 1991.
16. Princeton Instruments Catalog of High Performance Cameras. Princeton Instruments, Inc., Jan. 1994.
17. Taylor, B. N.; and Kuyatt, C. E.: Guidelines for Evaluating and Expressing the Uncertainty of NIST Measurement Results. NIST Technical Note 1297, 1994 Edition, National Institute of Standards and Technology, Sept. 1994.
18. Orloff, K. L.; and Snyder, P. K.: Laser Doppler Anemometer Measurements Using Nonorthogonal Velocity Components: Error Estimates. Applied Optics, vol. 21, no. 2, Jan. 15, 1982, pp. 339–344.
19. Coleman, H. W.; and Steele, W. G., Jr.: Experimental and Uncertainty Analysis for Engineers. John Wiley and Sons, New York, 1989.
20. Widnall, S. E.; and Sullivan, J. P.: On the Stability of Vortex Rings. Proceedings of the Royal Society of London, Series A, vol. 332, 1973, p. 335.
21. Alexander, M. G., Captain: Pneumatic Forebody Vortex Control and Leading Edge Flap Hingeline Blowing Using the 55% SHARC Model. WL-TR-96-3002, 1996.
22. Meyers, J. F.: Generation of Particles and Seeding. von Karman Institute for Fluid Dynamics Lecture Series 1991-08, June 10–14, 1991.

23. Takahashi, T. T.; Eidson, R. C.; and Heineck, J. T.: Aerodynamic Characteristics of a Supersonic Transport with Pneumatic Forebody Flow Control. AIAA Paper 97-0043, 35th Aerospace Sciences Meeting, Jan.6–10, 1997, Reno, Nev.
24. Storms, B. L.; Takahashi, T. T.; and Ross, J. C.: Aerodynamic Influence of a Finite-Span Flap on a Simple Wing. SAE Technical Paper 951977, Aerotech '95, Sept. 18–21, 1995, Los Angeles, Calif.

<b>REPORT DOCUMENTATION PAGE</b>			Form Approved OMB No. 0704-0188	
Public reporting burden for this collection of information is estimated to average 1 hour per response, including the time for reviewing instructions, searching existing data sources, gathering and maintaining the data needed, and completing and reviewing the collection of information. Send comments regarding this burden estimate or any other aspect of this collection of information, including suggestions for reducing this burden, to Washington Headquarters Services, Directorate for Information Operations and Reports, 1215 Jefferson Davis Highway, Suite 1204, Arlington, VA 22202-4302, and to the Office of Management and Budget, Paperwork Reduction Project (0704-0188), Washington, DC 20503.				
<b>1. AGENCY USE ONLY (Leave blank)</b>		<b>2. REPORT DATE</b> September 1997	<b>3. REPORT TYPE AND DATES COVERED</b> Technical Memorandum	
<b>4. TITLE AND SUBTITLE</b>  Doppler Global Velocimeter Development for the Large Wind Tunnels at Ames Research Center			<b>5. FUNDING NUMBERS</b>  519-20-22	
<b>6. AUTHOR(S)</b>  Michael S. Reinath				
<b>7. PERFORMING ORGANIZATION NAME(S) AND ADDRESS(ES)</b>  Ames Research Center Moffett Field, CA 94035-1000			<b>8. PERFORMING ORGANIZATION REPORT NUMBER</b>  A-977253	
<b>9. SPONSORING/MONITORING AGENCY NAME(S) AND ADDRESS(ES)</b>  National Aeronautics and Space Administration Washington, DC 20546-0001			<b>10. SPONSORING/MONITORING AGENCY REPORT NUMBER</b>  NASA TM-112210	
<b>11. SUPPLEMENTARY NOTES</b> Point of Contact: Michael S. Reinath, Ames Research Center, MS 247-2, Moffett Field, CA 94035-1000 (650) 604-6680				
<b>12a. DISTRIBUTION/AVAILABILITY STATEMENT</b>  Unclassified — Unlimited Subject Category 35			<b>12b. DISTRIBUTION CODE</b>	
<b>13. ABSTRACT (Maximum 200 words)</b>  Development of an optical, laser-based flow-field measurement technique for large wind tunnels is described. The technique uses laser sheet illumination and charged coupled device detectors to rapidly measure flow-field velocity distributions over large planar regions of the flow. Sample measurements are presented that illustrate the capability of the technique.  An analysis of measurement uncertainty, which focuses on the random component of uncertainty, shows that precision uncertainty is not dependent on the measured velocity magnitude. For a single-image measurement, the analysis predicts a precision uncertainty of $\pm 5$ m/s. When multiple images are averaged, this uncertainty is shown to decrease. For an average of 100 images, for example, the analysis shows that a precision uncertainty of $\pm 0.5$ m/s can be expected.  Sample applications show that vectors aligned with an orthogonal coordinate system are difficult to measure directly. An algebraic transformation is presented which converts measured vectors to the desired orthogonal components. Uncertainty propagation is then used to show how the uncertainty propagates from the direct measurements to the orthogonal components. For a typical forward-scatter viewing geometry, the propagation analysis predicts precision uncertainties of $\pm 4$ , $\pm 7$ , and $\pm 6$ m/s, respectively, for the $U$ , $V$ , and $W$ components at 68% confidence.				
<b>14. SUBJECT TERMS</b>  Aerodynamic measurements, Wind tunnel instrumentation, Laser velocimetry			<b>15. NUMBER OF PAGES</b> 57	
			<b>16. PRICE CODE</b> A04	
<b>17. SECURITY CLASSIFICATION OF REPORT</b> Unclassified	<b>18. SECURITY CLASSIFICATION OF THIS PAGE</b> Unclassified	<b>19. SECURITY CLASSIFICATION OF ABSTRACT</b>	<b>20. LIMITATION OF ABSTRACT</b>	